

A Fermi-degenerate three-dimensional optical lattice clock

by

Sara L. Campbell

B.S., Massachusetts Institute of Technology, 2010

A thesis submitted to the
Faculty of the Graduate School of the
University of Colorado in partial fulfillment
of the requirements for the degree of
Doctor of Philosophy
Department of Physics

2017

This thesis entitled:
A Fermi-degenerate three-dimensional optical lattice clock
written by Sara L. Campbell
has been approved for the Department of Physics

Prof. Jun Ye

Prof. James Thompson

Date _____

The final copy of this thesis has been examined by the signatories, and we find that both the content and the form meet acceptable presentation standards of scholarly work in the above mentioned discipline.

Campbell, Sara L. (Ph.D., Physics)

A Fermi-degenerate three-dimensional optical lattice clock

Thesis directed by Prof. Jun Ye

Strontium optical lattice clocks have the potential to simultaneously interrogate millions of atoms with a spectroscopic quality factor $\mathbf{Q} \approx 4 \times 10^{17}$. Previously, atomic interactions have forced a compromise between clock stability, which benefits from a large atom number, and accuracy, which suffers from density-dependent frequency shifts. Here, we demonstrate a scalable solution which takes advantage of the high, correlated density of a degenerate Fermi gas in a three-dimensional optical lattice to guard against on-site interaction shifts. Using a state-of-the-art ultra-stable laser, we achieve an unprecedented level of atom-light coherence, reaching $\mathbf{Q} = 5.2 \times 10^{15}$ with 1×10^4 atoms. We investigate clock systematics unique to this design; in particular, we show that contact interactions are resolved so that their contribution to clock shifts is orders of magnitude lower than in previous experiments, and we measure the combined scalar and tensor magic wavelengths for state-independent trapping along all three lattice axes.

Dedication

To Brad

Acknowledgements

First of all, I thank Jun for being the best advisor I can possibly imagine. Once I stopped being so intimidated by him, Jun became a great friend who I could rely on for advice about everything from the noise properties of mundane circuit components to life's biggest questions. What I most admire about Jun is his fearlessness. From years of working with him, I have come to believe that there is nothing we cannot gradually tackle via persistence and improved measurement capabilities. Jan Hall surely played a key role in fostering Jun's playful enthusiasm in the lab. I thank Jan for his warm company in the electronics shop, and for setting an example to appreciate every little bit involved in getting an experiment working. Indeed, even the smallest electronic challenges can be "great fun!"

When I first arrived at JILA, I felt a bit like a deer in the headlights. I am incredibly indebted to Ben Bloom for taking me under his wing, teaching me how to debug and how to manage a project. Travis Nicholson's passion for our experiment convinced me to join. Jason Williams' quiet wisdom always came just when we needed it. Other strontium alumni I enjoyed working with include Mike Martin, Mike Bishof, Xibo Zhang, and Matt Swallows.

I feel especially lucky to have had a great few years building the new system with the SrQ Dream Team. Everyone's unique strengths were essential to getting our new experiment working. While technically we were supposed to be supervising our undergraduate student Rees McNally, it was not long before he was the one teaching us! Among many other important projects, Rees designed, built, and tested the high-current magnetic coil control electronics. Masters student Nelson Darkwah Oppong built the 1064 laser system, figured out how to use the high-power fibers,

and made us some beautiful German-engineered low-noise photodiodes, complete with instructions from Easy-E on how to set the gain. We still miss his laugh and exclamations of "niiiiice!!" along with all of his insight and technical tips. We also enjoyed the company and curiosity of visiting student Dan Reed who always made us laugh.

Ross Hutson is insanely good at everything from FPGA programming to theoretical three-body calculations, and he manages to do it all with quiet goofiness, modesty and thoughtfulness towards others. Lab is rad, LabRad is rad, and Ross is the raddest. Ed Marti (my human Mendeley library) is an AMO renaissance man, whose broad knowledge and insights both led us to new ideas and prevented several disasters. During his time in the Ye group, Ed has also assumed the role of "Team Mom," taking special care of all us little strontium ducklings, and being our go-to person for life and physics advice. Aki Goban is a conscientious experimentalist and a deep thinker who is always willing to jump in and get things done, as well as one of the kindest people I know. I like it when Aki breaks character and gets sassy, because it means you deserved it. I feel privileged to have been a part of this amazing team, and I can't wait to see what they do next.

Thank you to all of our collaborators. The Rey group regularly attended group meetings, adding insights and excitement. Tom Loftus was meticulous, honest, and available to help – just the person you need when having strange problems with a new prototype. Dylan Cotta from Stephan Kuhr's group graciously shared all of their knowledge on using photonic crystal fibers for high power and was patient with my incessant emails. David Tracy of TraTech Fiberoptics did a beautiful custom job connectorizing these fibers for us and was similarly patient with my incessant emails. Tim Darby of the UK Atomic Energy Authority helped with the design and construction of our recessed viewports, was accommodating when we had some unusual problems, and was also patient with my incessant emails. Our team really enjoyed visits from both Darrick Chang and Helmut Ritsch which helped us get a handle on the magnitude and mechanisms of dipolar interactions in our present system, as well as gave us inspiration to work towards future possibilities. While we play with new ideas for clocks, Judah Levine carries the responsibility of actually telling the time, and kindly maintains a Cs-referenced 10 MHz signal so that all of Jun

and Jan's experiments - from clocks to combs to molecules - have a reliable RF reference. Every few years, when we need to actually measure a number, it has been a real treat to take field trips to his Time Lord fortress to hear about "fiberology," "jiggly-wiggles" and how one *actually* measures time. In earlier accuracy studies, we worked with Marianna Safronova, Wes Tew, and Gregoroy Strouse to further nail down the BBR shift. Insights on the state of our field from Murray Holland and Misha Lukin were greatly appreciated when I emerged from the basement to ponder such things.

We shared much of the strontium experience with the Sr1 gang. I admire Sarah Bromley's determination and level of focus in the lab. We have enjoyed the ideas and thoughtful company of Shimon Kolkowitz (not to mention the donuts and breakfast burritos). Toby Bothwell seems to get more excited about strontium every day. With a curiosity for the truth and an eye towards the big picture, he will do a great job at steering Sr1's future experimental direction. Dhruv Kedar recently joined the team as well, adding his talent and positive attitude.

Finally, thank you to the stable laser crew, who provide the heartbeat and the gears of the optical lattice clock. In the lab, I "grew up" taking Mike Martin's 40 cm ULE cavity for granted. The first demonstration of the better stability of a many-particle frequency reference would not have been possible without it. Wei Zhang has the superhuman capability of working two postdocs at once and selflessly does whatever needs to get done. Lindsay Sonderhouse persevered in getting the comb working again, and maintains a thoughtfulness towards the broader context of science in society. John Robinson was the next to join the team; I have never met a young student more excited about Allan deviations. Yo dawg, I heard you are fond of the meta, so I put infinities inside your infinities so you can self-similarity forever. The most recent addition was postdoc Erik Oelker, who is applying LIGO-style transfer-function-ology to elucidate some of the ultrastable laser voodoo.

A huge thanks to the JILA electronics and machine shops. Not only do they do beautiful, highly specialized work, they also teach us students to do these things ourselves. Terry Brown always has time for impromptu lectures on feedback. Carl Sauer taught me some of his debugging

and surface mount soldering skills. James Fung-a-fat and Chris Ho's good-humored presence and technical tips were always appreciated.

Pushing the limits of metrology often requires pushing the limits of machinists' patience, and so I am infinitely grateful to everyone in the JILA machine shop. Kim Hagen had to put up with the majority of the magnetic coil winding. Hans Green made our temperature sensors for both accuracy evaluations and somehow managed to keep a positive attitude. Blaine Horner's wisdom was crucial throughout the design process. Tracy Keep helped us design the water cooling manifold and was the general magnetic field guru. Todd Asnicar coordinated all of these jobs beautifully.

There are too many other JILA folks to really do justice to in these acknowledgements. Thank you to the rest of the Ye group for their company and expertise, and also to the Thompson group who graciously shared their knowledge and their lab space. Thank you to Brian Lynch, Dan Lewis, and Jennifer Erickson in the supply office; Xu the custodian for her friendly hellos; Amy Allison for her help with everything; Dave Alchenberger for all things tiny and/or coated; JR, Cory, and others in computing for their help and company; Chris Purtell and Dave Errickson for assistance with our FACMAN questions and problems; Beth Kroger for being there when things really needed to get done. Finally, none of the work presented in this thesis would have been possible without Debbie Jin, who laid the experimental groundwork for degenerate Fermi gases and continues to be an inspiration.

I first discovered how much fun AMO can be in Martin Zwierlein's group at MIT ("djyeeah-hhhhhh!"). Thanks to Martin for all of the excitement, Peyman Ahmadi for his kind leadership and team spirit, Cheng-Hsun Wu for the laughter, and Ibon Santiago for the camaraderie. From countless optics from BECII (aka "Wal-Mart") to his Solidworks files, Aviv Keshet has been graciously letting me steal his things for my entire AMO career. Outside of lab, Nergis Mavalvala was the best junior lab instructor, Javier Duarte was the best junior lab partner, and my academic advisor Gabriella Sciolla always fought for my best interest.

Outside of lab, my roommates (aka the men and women of Beefcake Manor) were my second family. Thank you to Bob Peterson, Ben Pollard, AJ Johnson, Scott Johnson, Liz Shanblatt,

and Andy Missert. My friends and climbing partners including Brian O'Callahan, Kuyler and Madrone Coopwood, and Cathy Klauss kept me sane. Thank you to my parents for encouraging and supporting my interests and my brother Jonathan for always being on my team. Thank you as well to the Callahans, Auntie Jen and Uncle Mo, Julie Grandma, and Fred Grandma for all of their help along the way.

Lastly I thank my husband Brad Johnson, the smartest person I know, for his love, patience, and advice.

Contents

| Chapter | |
|----------------|--|
| 1 | Introduction 2 |
| 1.1 | Historical perspective 2 |
| 1.2 | The current frontier 9 |
| 1.3 | Coupled bands 11 |
| 1.4 | 3D Lattice Design 18 |
| | |
| 2 | New Apparatus 21 |
| 2.1 | UHV System 21 |
| 2.1.1 | Design 21 |
| 2.1.2 | Viewports 22 |
| 2.1.3 | Bake-out procedure 24 |
| 2.2 | Chamber mounts, custom breadboards, and other mechanical structures 31 |
| 2.3 | Magnetic fields 35 |
| 2.3.1 | Compensation/bias coils 35 |
| 2.3.2 | Anti-Helmholtz coils 37 |
| 2.3.3 | Quadrant coils 40 |
| 2.3.4 | Single layer selection 45 |
| 2.3.5 | Control electronics 45 |
| 2.3.6 | Mounting and water cooling 52 |

| | | |
|----------|---|------------|
| 2.4 | Laser systems | 63 |
| 2.4.1 | Optics layout around the main experiment | 63 |
| 2.4.2 | Blue system upgrades | 66 |
| 2.5 | Imaging system | 68 |
| 2.5.1 | Design | 70 |
| 2.5.2 | Measuring and testing resolution | 77 |
| 3 | Preparation | 80 |
| 3.1 | Initial laser cooling stages | 80 |
| 3.2 | Crossed optical dipole trap | 85 |
| 3.2.1 | Initial loading | 85 |
| 3.2.2 | Theory | 85 |
| 3.2.3 | Measuring trap frequencies | 87 |
| 3.3 | Red absorption imaging | 88 |
| 3.3.1 | Magnetic field cancellation and calibration | 88 |
| 3.3.2 | Optical pumping and spin state detection | 94 |
| 3.4 | Evaporation | 94 |
| 3.5 | Kapitza-Dirac scattering | 97 |
| 3.6 | Lattice loading and characterization | 99 |
| 4 | Experiments | 108 |
| 4.1 | Lattice AC Stark Shifts | 108 |
| 4.1.1 | Experimental configuration and measurement | 109 |
| 4.1.2 | Data analysis and statistical methods | 112 |
| 4.2 | Interactions | 117 |
| 4.2.1 | On-site contact interactions | 117 |
| 4.2.2 | Dipolar interactions | 122 |
| 4.3 | Narrow line spectroscopy | 126 |

| | | |
|----------|--|------------|
| 4.4 | Stability | 126 |
| 5 | Future prospects and conclusion | 131 |
| 5.0.1 | Accuracy | 131 |
| 5.1 | Dark matter searches | 134 |
| 5.2 | The future of quantum metrology | 137 |
| | Bibliography | 140 |
| | Appendix | |
| A | Anti-reflection coating fused silica viewports: A cautionary tale | 152 |

Tables

Table

| | | |
|-----|---|----|
| 1.1 | Typical operating parameters. | 19 |
| 1.2 | Requirements for clock operation in a Mott-insulating regime with one atom per site. | 20 |
| 2.1 | Specifications for important lasers used in the experiment. | 62 |
| 2.2 | AOSense requirements | 68 |

Figures

Figure

| | | |
|------|---|----|
| 1.1 | | 4 |
| 1.2 | | 4 |
| 1.3 | Coupled bands for different dressing laser Rabi frequencies | 13 |
| 1.4 | Coupled bands for different clock laser detunings | 14 |
| 1.5 | Coupled band lineshapes for different tunneling rates | 16 |
| 1.6 | Coupled band lineshapes for different phase shifts | 17 |
| 2.1 | CAD drawings of the UHV chamber | 23 |
| 2.2 | TAKOS AR coatings spectrophotometer measurements | 25 |
| 2.3 | REO AR coating spectrophotometer measurement | 29 |
| 2.4 | Which viewports have what AR coatings | 30 |
| 2.5 | Chamber mounts | 32 |
| 2.6 | CAD drawings of the full system | 33 |
| 2.7 | Mezzanine posts | 34 |
| 2.8 | Optical table enclosure | 36 |
| 2.9 | Compensation coils CAD model | 38 |
| 2.10 | Teflon spacers in the compensation coil mounts | 38 |
| 2.11 | Compensation coil design fields | 39 |
| 2.12 | Anti-Helmholtz coil design | 40 |

| | | |
|------|---|----|
| 2.13 | Anti-Helmholtz coil fields | 41 |
| 2.14 | CAD model of quadrant coils | 43 |
| 2.15 | Quadrant coil schematic | 43 |
| 2.16 | Constructing the quadrant coils | 44 |
| 2.17 | 3D plots of fields generated by actual quadrant coils | 46 |
| 2.18 | Magnetic fields of actual quadrant coils | 47 |
| 2.19 | x lattice layer selection schematic | 48 |
| 2.20 | Applying a magnetic field to select a layer along x | 49 |
| 2.21 | Range of transition frequencies due to magnetic field curvature | 50 |
| 2.22 | Coil control electronics | 53 |
| 2.23 | Coil switching logic logic | 54 |
| 2.24 | Coil switching explanation | 55 |
| 2.25 | Anti-Helmholtz and quadrant coil current servo | 56 |
| 2.26 | Anti-Helmholtz coil design | 57 |
| 2.27 | Photo of all bucket coils | 57 |
| 2.28 | Bottom coil water and electrical hookups | 58 |
| 2.29 | Top coil water and electrical hookups | 59 |
| 2.30 | Interlock schemaite | 61 |
| 2.31 | Interlock photo | 61 |
| 2.32 | Mezzanine optics layout | 64 |
| 2.33 | Bottom optics layout | 65 |
| 2.34 | Top mezzanine layout | 67 |
| 2.35 | Artist's depiction of the optics layout process. | 67 |
| 2.36 | Blue system schematic | 69 |
| 2.37 | Imaging system section view | 71 |
| 2.38 | Illustration of aberrations | 73 |
| 2.39 | Meniscus coating curve | 75 |

| | | |
|------|---|-----|
| 2.40 | Imaging system design | 76 |
| 2.41 | Image of a two-pinhole test pattern | 78 |
| 2.42 | Measuring resolution via the Rayleigh criterion | 78 |
| 3.1 | Sr-87 level diagram | 81 |
| 3.2 | 3P_2 trap lifetime | 83 |
| 3.3 | Timing diagram for the red MOT and ODT loading | 86 |
| 3.4 | Attempt to measure XODT frequencies via parametric heating | 89 |
| 3.5 | Measuring ODT trap frequencies via dipole oscillations | 90 |
| 3.6 | HODT vertical calibration | 91 |
| 3.7 | 3P_1 scans for compensation coil calibration | 92 |
| 3.8 | Compensation coil field calibration | 93 |
| 3.9 | Polarization configuration for measuring spin populations with 3P_1 absorption imaging | 95 |
| 3.10 | 3P_1 scans of nuclear spin states | 95 |
| 3.11 | Time-of-flight data of a degenerate gas in the optical dipole trap | 96 |
| 3.12 | Dipole dipole trap lifetime | 98 |
| 3.13 | Kapitza-Dirac scattering | 100 |
| 3.14 | Lattice loading timing diagram | 101 |
| 3.15 | Experiment schematic | 103 |
| 3.16 | Motional sidebands | 104 |
| 3.17 | Doublet suppression for $T = 50$ nK. | 107 |
| 3.18 | Doublet suppression for $T = 15$ nK | 107 |
| 4.1 | AC Stark cartoon | 110 |
| 4.2 | AC Stark data | 111 |
| 4.3 | AC Stark data autocorrelation function | 115 |
| 4.4 | Vector Stark shifts | 116 |
| 4.5 | Level diagram for two-atom interactions | 118 |

| | | |
|------|--|-----|
| 4.6 | Interaction spectroscopy data | 123 |
| 4.7 | Spectrum of all transitions on doubly-occupied sites | 124 |
| 4.8 | Line pulling calculation | 125 |
| 4.9 | Narrow-line Ramsey spectroscopy | 127 |
| 4.10 | Narrow-line Rabi spectroscopy | 128 |
| 4.11 | Measured and calculated stability for different clock configurations. | 130 |
| A.1 | APC Quadband coating spectrophotometer measurement | 154 |
| A.2 | Never have your coatings done by American Photonics or Blue Ridge Optics | 155 |
| A.3 | TAKOS coating delamination | 156 |



Chapter 1

Introduction

Of the four fundamental forces, the electromagnetic force is the one most intricately tied to how we perceive and manipulate matter. Atoms, the building blocks of matter, are comprised of mostly empty space. Our eyes cannot resolve the electron clouds around atoms, tiny particles flying around in a huge void. We see the world through photons, the gauge bosons that mediate electromagnetic interactions, scattered into the eye where they are focused on the retina and converted to electric impulses that travel to the brain. The reason why we can touch and pick up a cup of coffee is because of the force of a billion virtual photons a second being exchanged between the atoms of our fingertips and the atoms of the cup, enforcing the Pauli exclusion principle that identical electrons cannot spatially overlap, a consequence of the unintuitive statistics of their minuscule realm. It is only natural then that spectroscopy, the study of the interaction between matter and electromagnetic radiation, was historically central to understanding the fundamentals of nature, and presently gives the physical quantities that can be the most accurately measured. SI base units such as the second and the meter, the labels we assign to the magnitudes of human experience, are all derived from spectroscopic measurements.

1.1 Historical perspective

Spectroscopy was our first window into the quantum world. When Isaac Newton used a prism to refract white light into its constituent colors in the mid-1600s, it appeared as a continuous rainbow (see Fig. 1.1) [146]. Joseph von Fraunhofer's inventions of the spectrometer and the

wire diffraction grating in the early 1800s both increased resolution, revealing discrete dark lines within the rainbow, and enabled absolute frequency measurements [27]. Scientists in the mid-1800s discovered that each element has its own unique spectrum [88]. The dark lines in the solar spectrum were the shadows cast by absorption at discrete energy levels of atmospheric atoms. Atoms were shown to emit at these discrete wavelengths, producing a negative of their absorption spectrum. In 1885, Johann Balmer found a simple formula that could predict the hydrogen spectrum in terms of integers [79]. Meanwhile, other experimental harbingers of quantum mechanics cropped up, including the photoelectric effect, the discovery of the electron, and the discovery of the discretized nature of electric charge [69, 78, 116]. To resolve the ultraviolet catastrophe, models by Planck and his contemporaries began to quantize the energy emitted and absorbed by matter. Then, in 1905, Einstein proposed a model where light came in discrete quanta of energy, in order to explain the photoelectric effect [54].

In 1917, Einstein laid the foundation for the modern laser when he described the three types of light-matter interactions [55]. Absorption and spontaneous emission were evident in the spectral lines first observed a century ago. Additionally, to satisfy Planck's law for the distribution of radiation at thermal equilibrium, Einstein introduced a third process: stimulated emission, whereby a photon causes an atom to transition from the excited state to the ground state, emitting a second photon identical to the first. The fact that nature already held the key to making perfect copies of quantized electromagnetic radiation was an early hint at the utility of this newly-discovered non-classical world. In 1953, Charles Townes demonstrated the first maser, a microwave amplifier based on stimulated emission on a 24 GHz transition in ammonia molecules [60]. Nikolay Basov and Aleksandr Prokhorov realized that these amplifiers could achieve continuous output by using two transitions: one for incoherent pumping to maintain a population inversion, and another for stimulated emission for coherent amplification [120]. Thus began an evolution towards quantum engineering, where the newly-discovered underpinnings of light and matter began to be exploited in clever ways.

Another breakthrough in spectroscopy came in 1938 when, with the matrix and wave me-

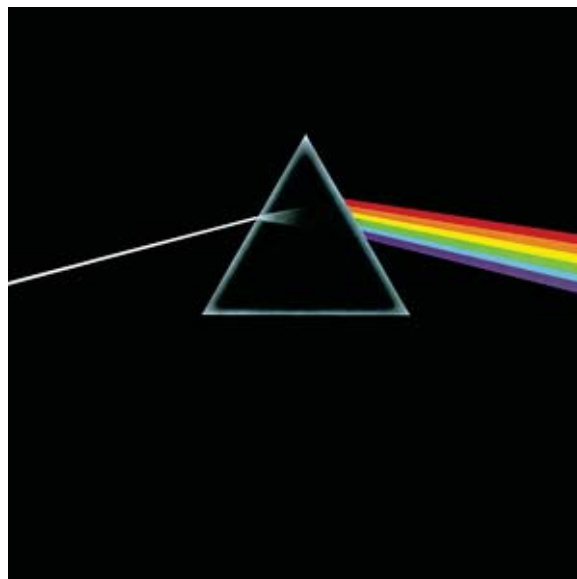


Figure 1.1: Album art from Pink Floyd's Dark Side of the Moon [155].

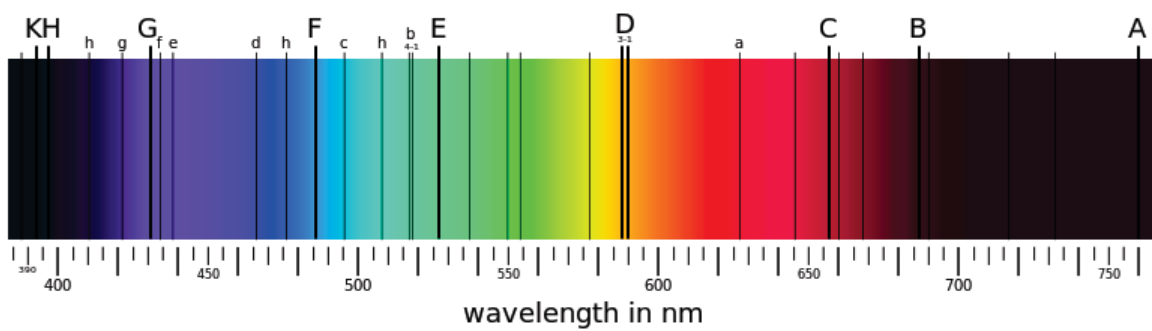


Figure 1.2: Fraunhofer lines in the spectrum of the sun [2].

chanics formulations of quantum mechanics recently established, I.I. Rabi demonstrated the first coherent manipulation of internal states of atoms in his seminal work on nuclear magnetic resonance [130]. His student Norman Ramsey improved on this protocol, introducing the method of “separated oscillatory fields” in 1949 [131]. Armed with the technology to coherently control both light and matter, we could finally begin working towards the vision first laid out in the Magna Carta in 1215, that, “There is to be a single measure ... throughout our realm.” [159] Agreements in the Magna Carta were not upheld, resulting in war within a year of the signing of the document, and as recently as 1795, abuse of units of measures was one of the motives of the French Revolution [113], thus highlighting the fallibility of man, and the superiority of the immutable laws of nature to enforce the equality of metrology standards. One of the new doctrines resulting from quantum theory was that, if two people each had a Cs atom that they were each using as a frequency reference, and they put their two atoms close enough together and in the same quantum state, the two quantum particles would be fundamentally indistinguishable. This then led to the cesium beam clock where the periodic “ticking” is provided by radio-frequency (RF) electromagnetic radiation and the absolute frequency reference is the ground hyperfine transition of the Cs-133 atoms, a constant of nature that is identical everywhere [3].

Spectroscopists continued to devise new methods to improve energy resolution, putting Newtons rainbow under an ever-finer microscope, looking for any anomalies that could force us to overhaul our foundational understanding of the natural world. One of the main hindrances to atomic spectroscopy was Doppler-broadening due to atomic motion; control of external degrees of freedom in precision measurement experiments remains important today. In 1947, Willis Lamb and Robert Retherford employed a clever use of microwave transitions to reduce Doppler effects and observe an unpredicted splitting between the $^2S_{1/2}$ and $^2P_{1/2}$ levels of the hydrogen atom, due to a one-loop correction to account for the zero-point energy of the vacuum causing absorption and emission of virtual photons [96]. This is another example where new measurement techniques mandated new understanding, and it spurred the development of modern quantum electrodynamics, introducing the general concept of renormalization in quantum field theory. Theoretical devel-

opments in quantum field theory, along with new particles discovered by generations of particle accelerators with ever-increasing collision energies, led to the formulation of the Standard Model of particle physics [129].

Meanwhile, with the foundations of quantum mechanics well established, atomic, molecular, and optical (AMO) physicists spent the latter half of the 20th century developing new techniques to control both light and matter. Beginning with the first continuous-wave helium-neon (HeNe) gas laser, the 1960s and 1970s saw the invention of several new kinds of lasers, frequency control, and finally frequency stabilization techniques[65]. Laser technology enabled the meter to be the next SI base unit to be fully defined in terms of fundamental constants: first in 1960 in terms of a number of wavelengths of an atomic transition, and then again in 1983 in terms of the length of the path traveled by light in $1/299792458$ of a second [1]. Frequency-stabilized lasers were a necessary tool in laser cooling and trapping of neutral atoms [150, 161, 36], which could then be loaded into a magnetic trap for evaporative cooling, culminating in 1995 with the synthesization of a new state of matter, the Bose-Einstein condensate (BEC), in which the majority of a gas of identical bosons occupies the lowest motional state of the trap [40, 87]. Finally, all degrees of freedom of individual quantum particles could be controlled. Just as the discovery of quantum mechanics led to the cesium beam clock, developments in laser cooling and trapping led to the cesium fountain clock, where the use of cold atoms allowed for longer interrogation times, improved stability, and a tenfold improvement in accuracy [77].

While the reductionist approach that dominated 20th century physics was widely successful in predicting a wide range of phenomena in terms of mean-field theory and perturbative expansions, it left a broad swath of physical phenomena unexplained, namely strongly-interacting many-body systems. Some outstanding problems falling in this category include the fractional quantum Hall effect, high-Tc superconductivity, and the quantum chromodynamics governing the physics of atomic nuclei, neutron stars, and quark matter. These phenomena are all physical manifestations of the more general numerical sign problem, in which the antisymmetrization required by Fermi statistics

requires summing over a large number of wavefunctions with opposite sign, resulting in convergence issues which become prohibitive in the thermodynamic limit [103]. While quantum entanglement was proposed in 1935 and demonstrated in the 1980s, Hilbert space grows exponentially with the number of particles, and so our understanding was limited to systems which either only have a few particles, or have an underlying symmetry.

“...it does seem to be true that all the various field theories have the same kind of behavior, and can be simulated in every way, apparently with little latticeworks of spins and other things.”

- R. Feynman [57]

In 1982, Richard Feynman considered that, while the complexity of quantum many-body systems quickly overwhelms classical computers, one can build a universal quantum simulator to predict their behavior [57]. At the turn of the millennium, some key tools and ideas were unearthed that enabled the realization of Feynmans vision.

As many of the outstanding problems in condensed matter and particle physics follow Fermi statistics, one challenge was to realize a controllable quantum gas of fermions, which are more difficult to evaporatively cool than their bosonic counterparts. A second challenge was in relating these highly-controllable synthetic ultracold atom systems to unexplained physical phenomena that are orders of magnitude away in temperature and density.

In 1999, Debbie Jin and student Brian deMarco produced the first degenerate Fermi gas of ultracold atoms [46]. Then, not long after, along came the idea of operating these quantum simulators in regimes giving access to so-called universal thermodynamics. At a Feshbach resonance [74], when the energy of two atoms in the open scattering channel is brought into resonance with the energy of a bound state in the closed channel, the scattering length a diverges. In the unitarity limit of $r \ll n^{-1/3} \ll a$, thermodynamic quantities depend only on the Fermi energy E_F (with corresponding Fermi temperature $k_B T_F = E_F$) and the temperature $k_B T$. The internal energy E can then be described in terms of a universal function f of a dimensionless parameter: $E = N E_F f(T/T_F)$ [132, 10]. All unitary Fermi gases, from ultracold quantum gases at a Feshbach

resonance (≈ 10 nK), to hot dense objects such as neutron stars ($\approx 10^6$ K) and quark-gluon plasmas ($\approx 10^{12}$ K), can be described via a single equation of state spanning over 20 orders of magnitude. An early triumph in the quantum simulation of natural phenomena was the measurement of the equation of state for the unitary Fermi gas in 2012 [94].

Additionally, quantum phase transitions, which occur at zero temperature by tuning the relative strengths of competing terms in the Hamiltonian, offer another link to the universal physics of quantum many-body systems. Just as in classical thermodynamics, the behavior of a system near a phase transition is governed by universal critical exponents which only depend on dimensionality and the power law of interactions. Inspired by crystal lattices governing the behavior of electrons in solid state materials, optical lattices made from standing waves of laser light were used to realize Hubbard models for an atomic gas. This led to the observation of the superfluid to Mott-insulator phase transition in a BEC [63]. Ultracold atomic systems operating at quantum criticality since have measured universal thermodynamic behavior.

While Debbie Jin was upstairs at JILA cooling potassium atoms, down in the basement, amid towering piles of papers, precariously air-wired circuits, and tangled webs of RF, Jan Hall and his team demonstrated the first octave-spanning frequency comb in 1999 [51].¹ This provided the missing step in converting between optical and microwave frequencies, as it allowed for measurement and stabilization of the carrier offset frequency f_0 , and thus opened the possibility of using optical frequency standards. The two fundamental limitations to clock stability are local oscillator noise which is aliased by running with a finite duty cycle via the Dick effect [76] and quantum projection noise (QPN), which depends on both the spectroscopic quality factor and the number of atoms being interrogated. Optical frequency standards achieve a much higher spectroscopic quality factor $Q = \nu/\Delta\nu$ than their RF counterparts by operating at a frequency ν that is over 4 orders of magnitude higher. The NIST mercury-ion and aluminum-ion clocks went on to break records in clock stability and accuracy [164, 66, 73].

¹ Little did Debbie and Jun know, they would soon combine these powers to cool potassium-rubidium molecules to their rovibrational ground state!

Also in 1999, work done at JILA, Caltech and in Japan [64, 83, 168] developing state-independent trapping potentials planted the seeds for optical lattice clocks, based on thousands of neutral atoms trapped in a one-dimensional (1D) optical lattice. These optical lattice clocks went on to gain another order order of magnitude in stability due to the lower quantum projection noise (QPN) limit [122, 70] and demonstrate record-breaking accuracies [121, 23]. With optical frequency transfer technology rapidly approaching the performance of the best ultra-stable lasers [49, 101], we are finally poised to upgrade our international time standard and frequency distribution infrastructure to an optical-frequency clock.

1.2 The current frontier

“The longing for a frontier seems to lie deep in the human soul... While there are clearly many nonscientific sources of adventure left, science is the unique place where genuine wildness may still be found.”

- Robert Laughlin [133]

Try as we might, we have little intuition for worlds we have not yet experienced. Human exploration encompasses both the outer limits of the cosmos and the tiniest energy shifts resolvable. Every time we measure something new, we gain new understanding. This new understanding extends the kinds of things we can make our tools out of and extends the limits of human perception. To quote Jun’s old website, “Every time you peel off another layer of nature and look in a little bit further, it gives you the most fantastic feeling.”²

In metrology, better stability ultimately leads to better accuracy, as systematic shifts can be evaluated to lower uncertainty during the finite number of hours in a day and years in a graduate student’s career [23, 121] . The two fundamental limitations to clock stability are local oscillator noise which is aliased by running with a finite duty cycle via the Dick effect and quantum projection noise (QPN), which depends on both the spectroscopic quality factor and the number of atoms being

² I would like to note that thus far, every time I have looked in a little bit further, all I’ve found is insidious technical noise. But I’m still totally holding out for dark matter.

interrogated. The QPN limit for Ramsey spectroscopy can be given as,

$$\sigma_{\text{QPN}}(\tau) = \frac{1}{2\pi\nu T} \sqrt{\frac{T + T_d}{N\tau}}, \quad (1.1)$$

where ν is the clock frequency, T is the free-evolution time, T_d is the dead time, and τ is the total averaging time. Typically, OLCs operate at a stability above this limit due to the Dick effect [76]; however, operation at or near the QPN limit has been demonstrated in systems through synchronous interrogation of two clocks [122, 154] or interleaved interrogation of two clocks with zero dead time [140]. For the future generation of optical lattice clocks, extended coherence time and more atoms will lead directly to smaller QPN. However, reaching the next goal of $10^{-18}/\sqrt{\tau}$ stability is extremely challenging for 1D OLCs as collisional effects force a compromise between interrogation time and the number of atoms that can be simultaneously interrogated [109, 121].

Throughout history, so-called fundamental limitations have merely been a consequence of the prevailing scientific paradigm. As science begins to tackle emergent behavior, we move beyond quantum phenomena that can be described in terms of its constituent components, to entangled many-body states, which can be engineered to overcome classical noise and be robust against perturbations. Here we take an initial step towards metrologically useful quantum correlated matter, presenting the first scalable solution to the central limitation of collisional effects in optical lattice clocks. We load a two-spin degenerate Fermi gas into the ground band of a 3D optical lattice in the Mott-insulating regime where the number of doubly occupied sites is suppressed [63, 80, 142]. In this configuration, the atom number can be scaled by orders of magnitude, while strong interactions prevent both systematic errors and decoherence associated with high atomic density. This work demonstrates the utility of Mott insulator physics for precision metrology, opening up new possibilities for novel schemes in which quantum gas technology overcomes limits of atom-light coherence.

More is different. - P. W. Anderson

More is a reduction in fundamental noise. - J. Ye³

³ At least half of the quotes in this thesis are fabricated.

1.3 Coupled bands

“Bandz a make her dance.” - Juicy J (the rapper, not Jun Ye)

Now we consider the effect of tunneling on the clock transition lineshape. While historically we have operated clocks deep in the Lamb-Dicke regime where the tunneling rate J is negligible, tunneling opens the door to spin-orbit-coupling studies [91] and other exciting quantum simulation prospects [61]. Furthermore, efforts to increase the atom-light coherence time beyond what has been demonstrated in this thesis may require contending with the upper clock state decay due to Raman scattering from the magic wavelength lattice. Studies of this effect in 1D systems posit that this may limit the excited state lifetime to ≈ 10 s [115]. Efforts to confirm this effect in our 3D system without the complication of lossy collisions between excited state atoms are currently underway.

As is a theme for other systematic effects and broadening mechanisms, there are two complementary facets to spin-orbit-coupling in an optical lattice clock. First, lineshape distortions provide an exciting measurement tool, allowing us to access spin-orbit-coupling physics using precision spectroscopy and uncover exciting many-body physics. Second, once we understand this physics, we can cleverly engineer our lattice geometry to eliminate these effects and enable clock operation at heretofore impossibly low trap depths, thus overcoming an imminent roadblock on the path towards the full potential of the strontium atom’s ≈ 160 s natural lifetime.

The following Hamiltonian describes atoms on 1D lattice sites with index m , spacing a and a tunneling rate J , in two different electronic orbitals e and g , coupled with Rabi frequency Ω with a laser with detuning δ , and a wavenumber k_c that results in a site-to-site phase shift $k_c a$, using the dressed-atom picture and the rotating wave approximation:

$$H = \sum_m J \left(a_g^\dagger a_{g,m+1} + \text{c.c.} + a_e^\dagger a_{e,m+1} + \text{c.c.} \right) \quad (1.2)$$

$$+ \Omega \left(e^{-ik_c a m} a_{g,m}^\dagger a_{e,m} + \text{c.c.} \right) + \frac{\delta}{2} \left(a_{e,m}^\dagger a_{e,m} - a_{g,m}^\dagger a_{g,m} \right) \quad (1.3)$$

To solve for the two coupled bands of this Hamiltonian, we use the following ansatz for the energy

eigenstates ϕ_k which have quasimomentum k :

$$\psi_k = \sum_m \left(c_1 a_{g,m}^\dagger e^{-ikam} + c_2 a_{e,m}^\dagger e^{-i((k-k_c)a)m} \right) |0\rangle \quad (1.4)$$

Plugging the ansatz into the time-independent Schrödinger equation $H\psi_k = E_\pm(k)\psi_k$ gives the following system of equations for the coefficients c_1 and c_2 :

$$\begin{pmatrix} 2J \cos ka - \delta/2 & \Omega \\ \Omega & 2J \cos((k - k_c)a) + \delta/2 \end{pmatrix} \begin{pmatrix} c_1 \\ c_2 \end{pmatrix} = \begin{pmatrix} c_1 \\ c_2 \end{pmatrix} \quad (1.5)$$

We then solve the characteristic equation to determine the energy eigenvalues $E_\pm(k)$,

$$\begin{vmatrix} 2J \cos ka - \delta/2 - E_\pm(k) & \Omega \\ \Omega & 2J \cos((k - k_c)a) + \delta/2 - E_\pm(k) \end{vmatrix} = 0, \quad (1.6)$$

finding that,

$$E_\pm(k) = J(\cos ka + \cos((k - k_c)a)) \quad (1.7)$$

$$\pm \sqrt{(J(\cos ka - \cos((k - k_c)a)))^2 - 2J(\cos ka - \cos((k - k_c)a)) \left(\frac{\delta}{2}\right) + \left(\frac{\delta}{2}\right)^2 + \Omega^2}. \quad (1.8)$$

These two bands are plotted for different Rabi frequencies in Figure 1.3, for the case of strontium in a magic wavelength lattice with spacing $813/2$ nm, and a copropagating 698 nm clock laser, which gives a site-to-site phase shift of $k_c a = 1.16\pi$. Turning on the clock laser with Rabi frequency Ω opens up a gap of $\approx \Omega$ between the two bands.

To calculate the effect of spin-orbit-coupling on the clock transition lineshape, we assume that $\Omega \ll J, \delta$, which simplifies the calculations but preserves the relevant physics. In this limit, the bands become,

$$E_-(k) = 2J \cos ka - \frac{\delta}{2} \quad (1.9)$$

$$E_+(k) = 2J \cos((k - k_c)a) + \frac{\delta}{2} \quad (1.10)$$

Figure 1.4 shows the intersecting bands for different detunings δ . At a given detuning δ , atoms that are initially in the lower band are driven to the excited band at the quasimomenta k

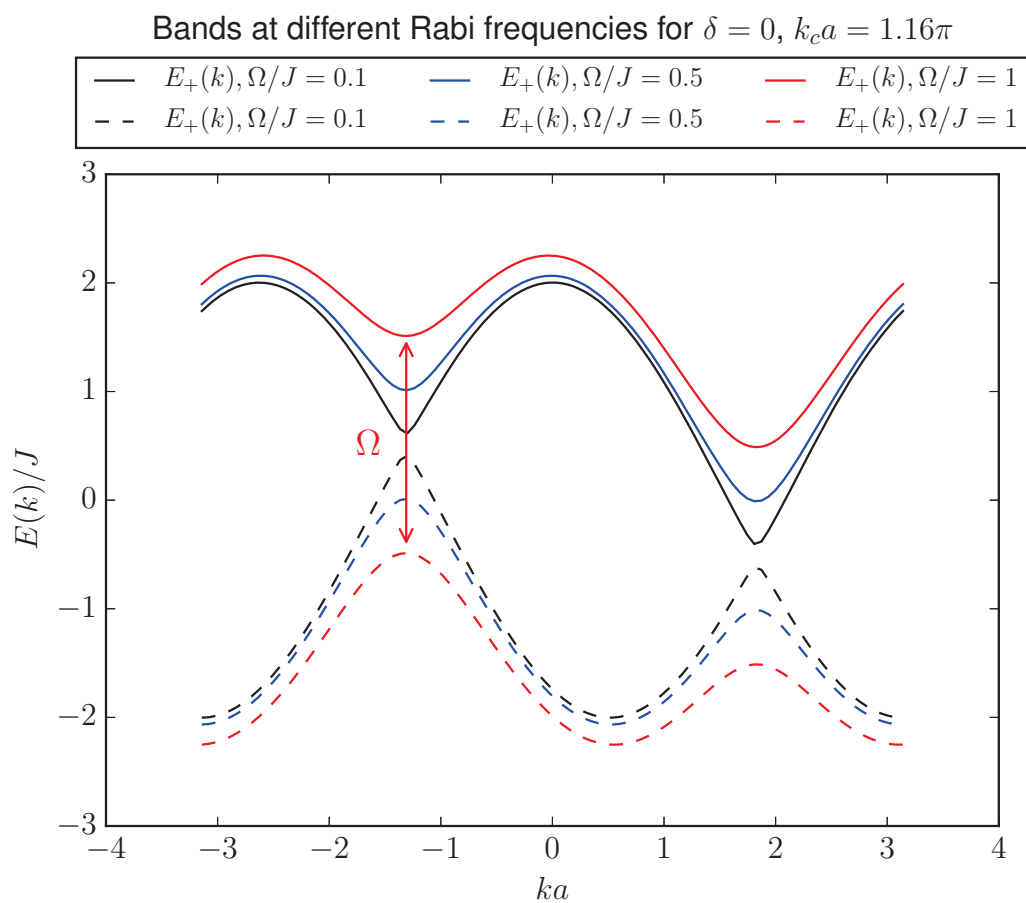


Figure 1.3: Plot showing how turning on the dressing clock laser with Rabi frequency Ω opens up a gap of $\approx \Omega$ between the two bands.

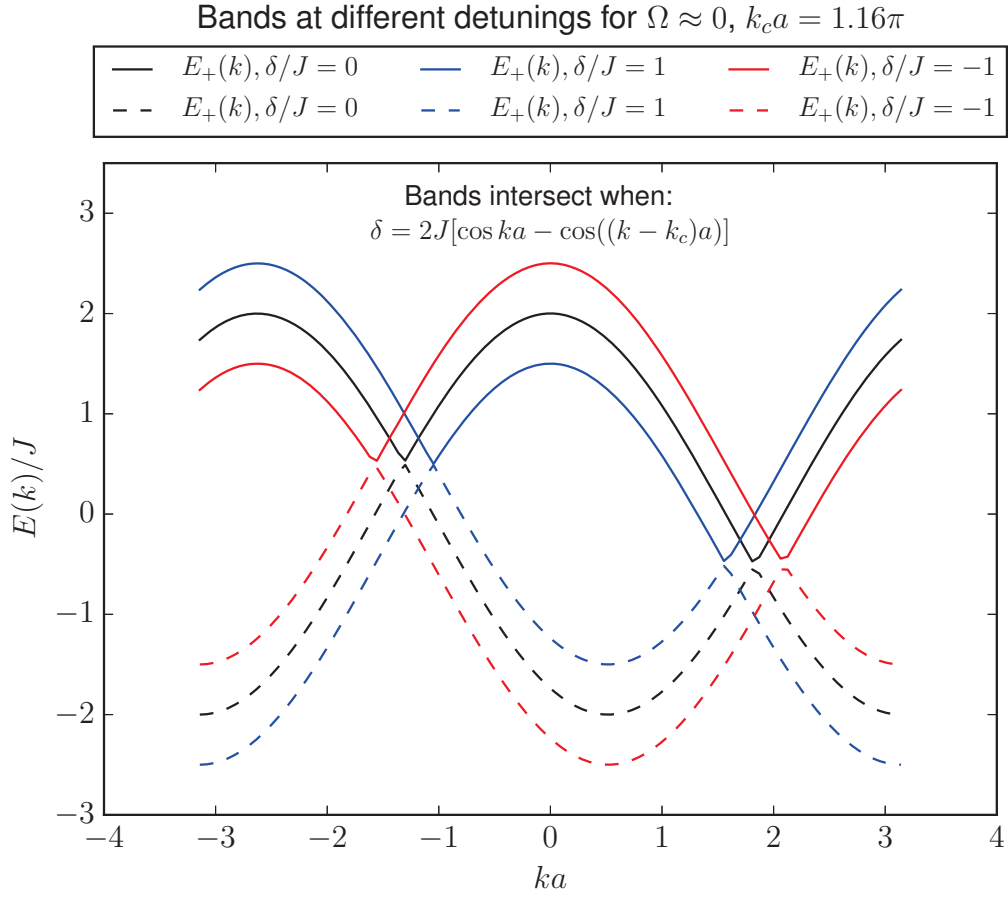


Figure 1.4: Plot showing how the energies of the two coupled bands varies with detuning of the dressing (clock) laser, in the limit of small Rabi frequency Ω compared to the detuning δ and tunneling rate J ($\Omega \ll \delta, J$). Atoms are initially in the bottom band, and at a given detuning, they are driven to the excited band at the quasimomenta where the two bands cross.

where the two bands cross according to,

$$\delta = 2J[\cos ka - \cos((k - k_c)a)] \quad (1.11)$$

$$= -4J \sin\left(\frac{k_c a}{2}\right) \sin\left(k - \frac{k_c a}{2}\right) \quad (1.12)$$

By inverting Equation 1.12, we can solve for the two quasimomenta k_1 and k_2 that are driven to the excited band at a given δ :

$$k_1(\delta) = \frac{1}{a} \sin^{-1}\left(\frac{\delta}{4J \sin(k_c a/2)}\right) + k_c/2 \quad (1.13)$$

$$k_2(\delta) = \pi/a + k_c - k_1 \quad (1.14)$$

To finally calculate the clock transition lineshape, our remaining task is to sum the density of states as a function of energy $D_n(E)$ at these two quasimomenta. We assume an evenly-filled ground band such that $D_n(k)dk$ is a constant.

$$D_n(E)dE \left(\frac{dk}{dE}\right) = D_n(k)dk \quad (1.15)$$

so therefore,

$$D_n(E)dE \propto \frac{dE}{dk}. \quad (1.16)$$

As explained in Equations 1.13 and 1.14 and illustrated in Figure 1.4, for a given δ , there are *two* k -values for which the bands cross. So, to find the total density of states $D(\delta)$ at a particular δ , we add the density of states at k_1 and k_2 to find,

$$D(\delta) = \left.\frac{dE_-(k)}{dk}\right|_{k=k_1(\delta)} + \left.\frac{dE_-(k)}{dk}\right|_{k=k_2(\delta)}, \quad (1.17)$$

where $k_1(\delta)$ and $k_2(\delta)$ are given by Equations 1.13 and 1.14. Approximate clock transition lineshapes for Rabi spectroscopy can then be determined by convolving the Rabi lineshape with $D(\delta)$.

Figure 1.5 plots the lineshapes for the standard 1D strontium configuration with $\phi = 1.16\pi$ as the tunneling rate J is increased, showing a splitting of the line of approximately $8J \sin \phi$. Figure 1.6 plots the lineshapes for $J = 2$ Hz for different ϕ , illustrating that phase matching of the two

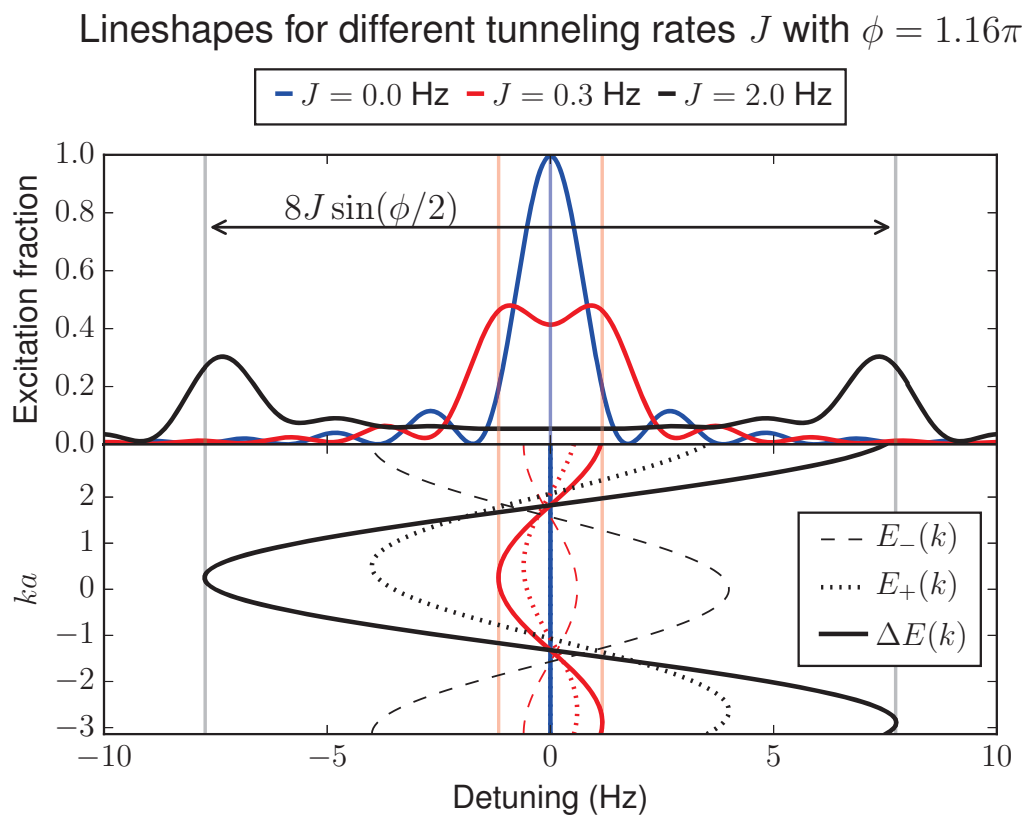


Figure 1.5: Plot showing splitting of the clock transition as the tunneling rate J is increased. This is shown for the standard configuration with co-propagating 698 nm clock laser and 813 nm lattice (with 813/2 nm spacing), giving a site-to-site clock laser phase shift of $\phi = 1.16\pi$.

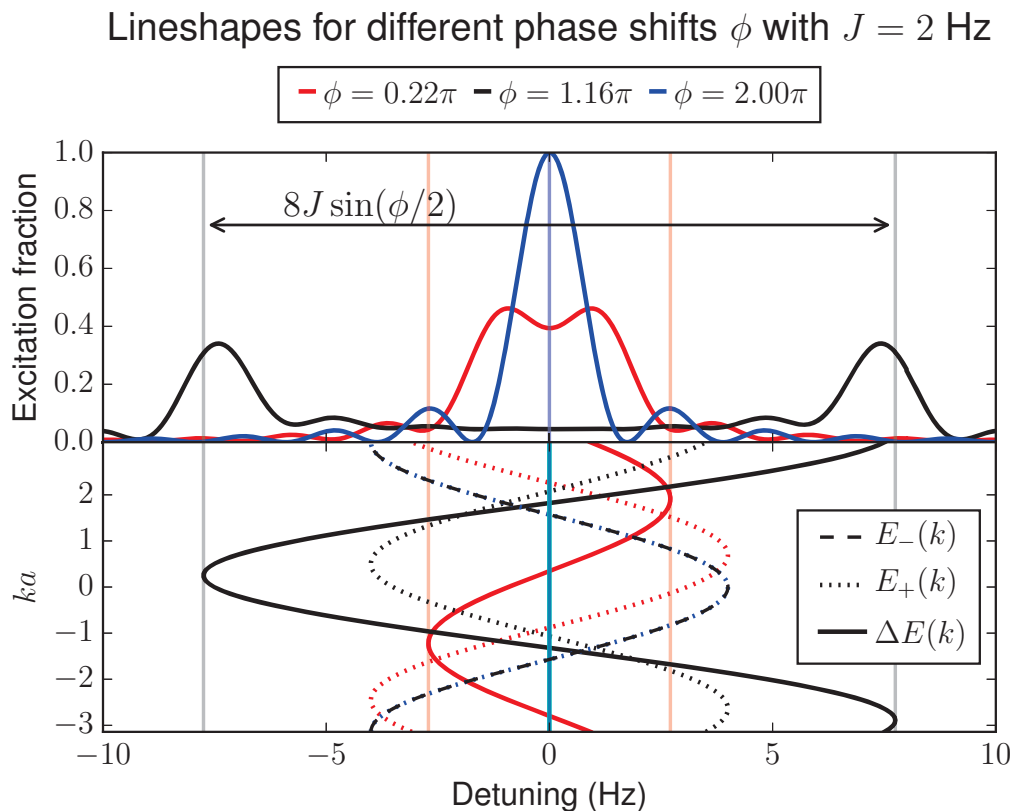


Figure 1.6: Plot showing splitting of the clock transition as a function of the clock laser site-to-site phase shift ϕ at a fixed tunneling rate $J = 2$ Hz. While the line can split by as much as 16 Hz, by carefully phase-matching the ground and excited bands, the momentum kick imparted by the clock laser can be canceled, and we could operate the clock at much lower lattice depths.

bands such that $\phi = 2\pi$ preserves the original lineshape, even at a tunneling rate that would dramatically split line in the standard $\phi = 1.16$ configuration.

However, while phase-matched bands allow for Doppler-free, recoil-free spectroscopy even at shallow lattice depths, this technique does not prevent the atoms from tunneling. In 1D optical lattice clocks, inelastic collisions between excited state atoms have been shown to result in atom loss and excitation fraction suppression [109, 121]. As we will describe in this thesis, we have already shown that we can overcome atomic interactions by trapping one atom per site in a 3D optical lattice. The use of a quantum gas in the Mott-insulating regime, where atomic interactions are responsible for doublon suppression, offers a way to continue to suppress atomic interactions and block tunneling even at relatively low trap depths, thus providing an option to overcome the upcoming limitation of Raman scattering. With each barrier to optical lattice clock performance that we solve, there are always more lurking at the next decimal place. We hope that the use of quantum correlated matter for precision metrology experiments will allow us to continue to engineer many-body states to push against future limitations.

1.4 3D Lattice Design

So, a Fermi-degenerate 3D optical lattice clock seems like a good idea. What kinds of lasers, optics, etc. should we spend all of Jun's money on?⁴ Here we review the basic technical requirements we considered when designing our new experiment.

First, we consider both the requirements for loading into the ground band of the lattice and for reaching the Mott-insulating regime. Loading the ground band requires that $E_{F,\text{ODT}}, k_B T_{\text{lattice}} \ll E_{\text{rec}}$, where $E_{F,\text{ODT}}$ is the Fermi energy in the ODT, k_B is the Boltzmann constant, T_{ODT} is the temperature in the ODT, and E_{rec} is the recoil energy from a lattice photon. Competition between tunneling (J) and repulsive interactions (U) initializes the spatial distribution of the atoms. As the lattice depth increases, multiple occupancies are suppressed when $12J \ll U$ and $k_B T_{\text{lattice}} \ll E_F \ll U$, where T_{lattice} is the temperature in the lattice [80, 142].

⁴ That Jun Ye gravy train. Choo choooo.

| Parameter | Symbol | Typical Value |
|---|---|--|
| Fermi energy in XODT | $E_{F,\text{XODT}}$ | $75 \text{ nK} \cdot k_B$ |
| Temperature in XODT | T_{XODT} | 15 nK |
| Lattice recoil energy | E_{rec} | $167 \text{ nK} \cdot k_B$ |
| Clock laser recoil energy | $E_{\text{rec,clock}}$ | $226 \text{ nK} \cdot k_B$ |
| Contact interaction energy | U | $2 \text{ kHz} \cdot h$ |
| Bloch bandwidth | $4J$ | $6 \times 10^{-7} E_{\text{rec}}$ |
| Tunneling rate along the clock laser axis | J_x/h | 0.5 mHz |
| Spectroscopy time | τ | 6 s |
| Lattice trap depth | $\mathcal{U}_{0,x}, \mathcal{U}_{0,y}, \mathcal{U}_{0,z}$ | $(100, 70, 50) E_{\text{rec,lattice}}$ |
| Lattice trap frequency | ν_x, ν_y, ν_z | $(65, 55, 45) \text{ kHz}$ |

Table 1.1: **Typical operating parameters.**

Next, we consider how finite tunneling rates affect clock spectroscopy. We require $1/J_x \gg \tau$, where J_x is the tunneling rate along the clock laser propagation direction and τ is the spectroscopy time, as the finite Bloch bandwidth of the lattice potential causes a first-order Doppler broadening of $8J_x$. This requirement is satisfied for our longest spectroscopy times $\tau = 6$ s by using lattice depths above $80E_{\text{rec}}$. To achieve a sufficiently deep trap as well as mode-match with the XODT, we use elliptical beams for the \hat{x} and \hat{y} lattice axes with horizontal and vertical waists of $120 \mu\text{m}$ and $35 \mu\text{m}$, respectively. The \hat{z} lattice beam is round with a $90 \mu\text{m}$ waist. Typical operating parameters in our experiment are summarized in Table 1.1, and a list of the requirements on these experimental parameters is summarized in Table 1.2.

OH YEAH! -Kool Aid Man

| Requirement | Inequality |
|-------------------------------|--|
| Ground band loading | $E_{\text{F,XODT}}, k_{\text{B}}T_{\text{lattice}} \ll E_{\text{rec}}$ |
| Double occupancy suppression | $J \ll U, k_{\text{B}}T_{\text{lattice}} \ll E_{\text{F,lattice}} \ll U$ |
| Resolved contact interactions | $\Delta U \gg 1/\tau$ |
| Lamb-Dicke | $h\nu \gg E_{\text{rec,clock}}$ |
| Doppler suppression | $8J_x/h \ll 1/\tau$ |

Table 1.2: **Requirements for clock operation in a Mott-insulating regime with one atom per site.**

Chapter 2

New Apparatus

2.1 UHV System

One of the requirements for both evaporating to Fermi degeneracy and exploring the limits of atom-light coherence is a long vacuum lifetime. This ultrahigh vacuum (UHV) system was designed to reach a pressure $\leq 1 \times 10^{-11}$ Torr for a vacuum lifetime ≥ 60 seconds for optically trapped atoms.

2.1.1 Design

The strontium source is a commercial system from the company AOSense, including an oven, Zeeman slower, and two 2D MOTs which both cool the atoms and direct them into the main chamber, allowing for no line-of-sight between the oven and the main experimental chamber. This design is advantageous, as it prevents blackbody radiation (BBR) photons from the hot oven from reaching the main experimental chamber, which would result in the atoms experiencing an athermal BBR spectrum, and more complicated clock systematics.

The strontium source is connected to the main system via a 4 inch long, 0.24 inch diameter differential pumping tube, corresponding to a sufficiently-low 1 L/s conduction of hydrogen to the main chamber. The main chamber design is based off of similar designs from MIT (cite Aviv thesis, Cheng thesis), and featuring recessed top and bottom viewports (“bucket windows”), which allow for both high-resolution ($\approx 1.2\mu\text{m}$) imaging and the placement of magnetic coils close to the center of the chamber for high magnetic field gradients (> 1 Gauss/(Amp·cm)). The main chamber was custom-made by the company Sharon Vacuum, from 304 stainless steel. They also

offered 316 stainless steel, but the company said that since these parts can get magnetized during the machining process, it is not worth the extra cost. The bucket windows were custom made by the UK Atomic Energy Authority (UKAEA), using 304 stainless steel for the flanges, and 316 stainless steel for the recessed portion, which would sit closer to the magnetic coils.

The science section of the main chamber connects to the pumping section via a wide square tube, so that the pumping on the main chamber is not conduction-limited. For pumps, we use a Varian titanium sublimation pump (TSP), which is contained in a large cylinder for maximal pumping surface area, a NEX Torr 300 L/s (for H₂) Non-evaporable Getter (NEG) and 6 L/2 (for Ar) ion combination pump, and we ultimately had to add a Varian 150 L/s StarCell ion pump because of an unexpectedly-high noble gas load. Additionally, we shipped the entire chamber to Jefferson Laboratories to have them coat the interior with a sputtered Titanium-Zirconium-Vanadium (TiZrVn) NEG coating. This coating reactivates at a temperature of 200°C (actually it can reactivate at lower temperatures, it just takes longer).

2.1.2 Viewports

The closer the laser wavelength is to the UV, the more one must worry about the bubble content of the viewport glass, as the glass can continue to fluoresce long after the laser beams are shut off, resulting in stray photons that can be detrimental to low-entropy Fermi gases and precision clock experiments. Because several steps of our experimental sequence depend on using a 461 nm transition, we took care to use grade A (maximum index variation ≤ 1 ppm) fused silica with an inclusion class of 0 (≤ 0.03 mm² total inclusion cross section per 100 cm³ of glass with a maximum size of 0.10 mm). We custom ordered our viewports from Larson Electronic Glass with the best specifications available for a reasonable price: 20/10 scratch-dig and $\lambda/4$ flatness. (They do not specify better than $\lambda/4$ flatness after warping that results from making the glass-to-metal seal without re-grinding and polishing.) We had some difficulties with our anti-reflection coatings delaminating from the fused silica (see Appendix for the full saga), but we ultimately settled on a combination of viewports with the AR coating curves shown in Figures 2.2 and 2.3,

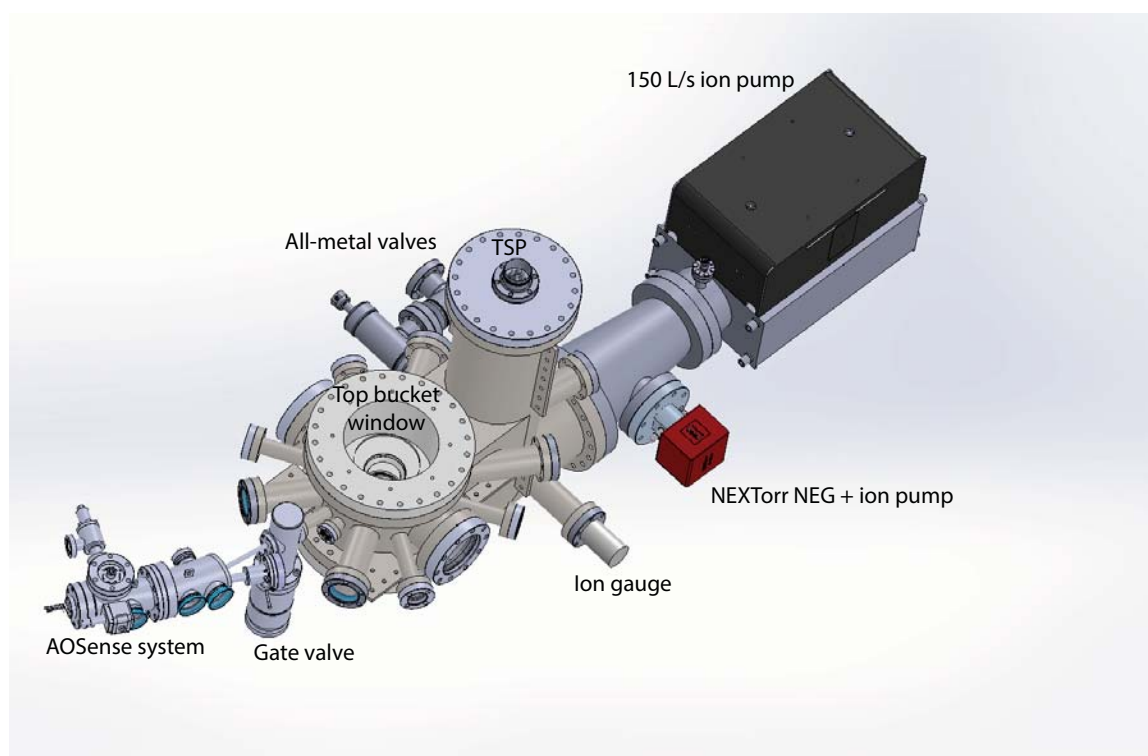
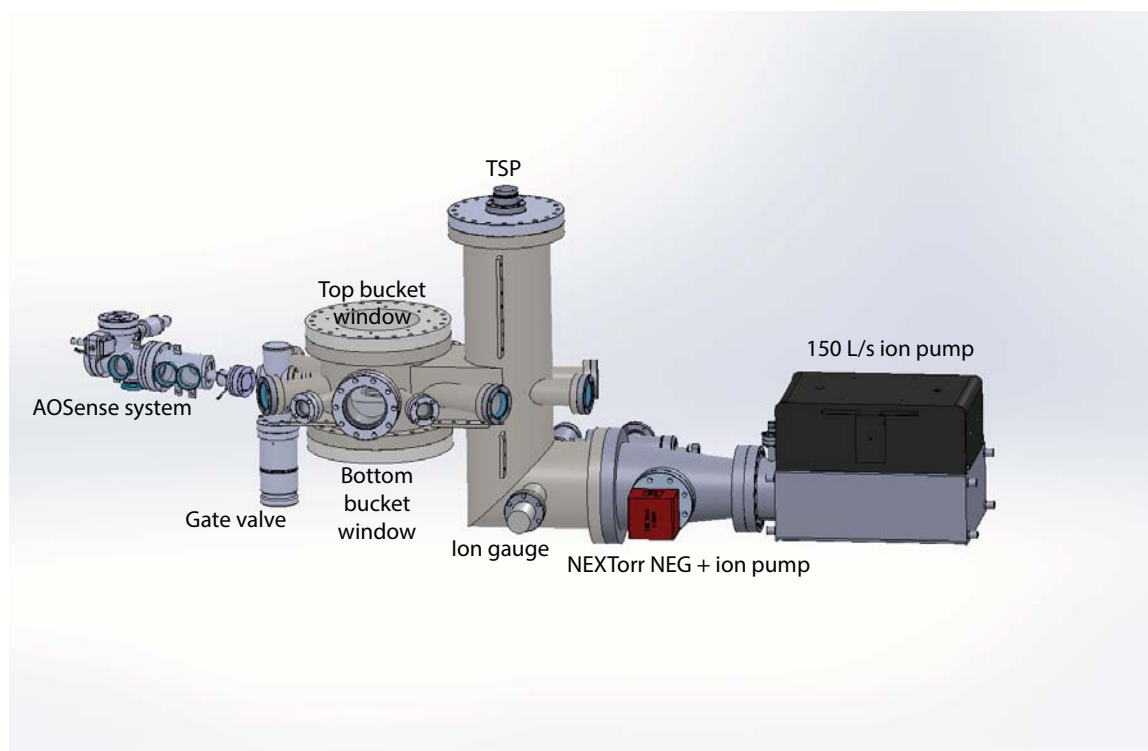


Figure 2.1: CAD drawings of the UHV chamber.

in the locations detailed in Figure 2.4. The coating scheme was determined by some compromise between technical requirements, availability, and time constraints. Apparently ion beam sputtering is better than electron beam sputtering (which both of our companies used). In the future, when asking companies for quotes, I would be more emphatic about the different thermal expansion coefficients of fused silica vs. stainless steel, and have any company assure me that they will do careful temperature control to minimize any mechanical stress.

2.1.3 Bake-out procedure

Due to complications introduced by using several getter pumps in conjunction, we had many steps to our bakeout procedure.

- (1) Remove ion pump magnets, make sure all cables for ion pumps, TSP, NEG pump, ion gauge, and residual gas analyzer (RGA) are plugged in.
- (2) Pump down with roughing pump and turbo pump, leak check using helium gas and the RGA.
- (3) Heat the whole system to 150-160°C, put the NEX Torr NEG into conditioning mode, run 25 A through each TSP filament to heat and clean (but not to deposit any titanium yet). We couldn't find a commercial TSP controller which allowed the current to go that low, so we borrowed a regular power supply from the electronics shop, hacked apart a TSP cable, and put all TSP filaments in parallel because they had similar resistance (to a few percent).
- (4) When the ion gauge reads 2×10^{-8} Torr, clean/degas/flash all components. Ion gauge: degas for the full 15 minutes as the manual suggests. RGA: Degas 3 times via the control software. Ion pump: Flashed twice by turning on the high voltage (saw nothing on the RGA). TSP filaments: Ramp them all at the same time to 37-42 A each and leave for 21 minute before ramping down to 25 A. Do this until the pressure rise from the gases other than hydrogen reads in the low 10^{-9} range on the RGA.

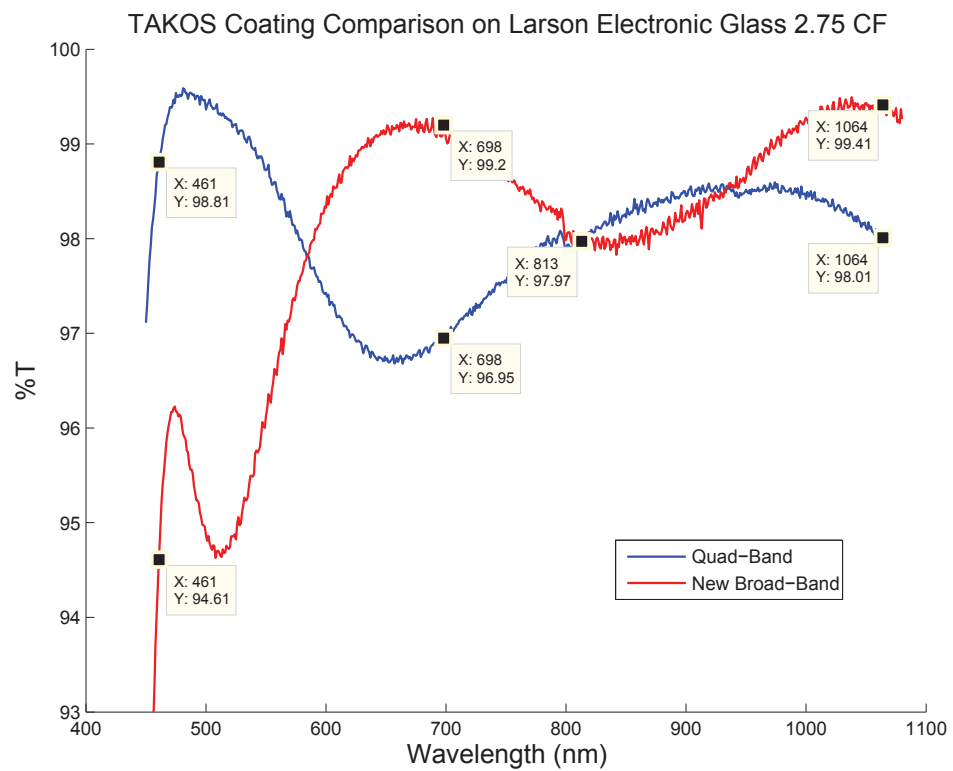


Figure 2.2: Spectrophotometer measurements of both coating runs from TAKOS used on the viewports.

- (5) Heat the whole system to $180 - 190^\circ$ C for several weeks. We realized that with the NEG in conditioning mode at 250° C, the pressure was not going to go below the low 10^{-8} level, so we turned off the conditioning mode to check the base pressure of the system, and found it to be below 10^{-8} Torr.
- (6) Clean the TSP filaments again. On the RGA, we saw mostly hydrogen, a little nitrogen, and a huge argon spike. Throughout most of the vacuum work, we saw odd spurious argon peaks on the RGA. After this, we had to wait overnight for the hydrogen pressure to return to normal. The next morning, we “flashed” (turned on the high voltage to) the ion pump again. We never saw any change to the RGA or ion gauge readings when flashing any ion pump in this manner.
- (7) Activate the NEX Torr NEG. Before activation, the ion gauge read a pressure of 1.2×10^{-8} Torr. First we tried regular activation, but we got scared when the pressure was a few 10^{-7} . Then we repeatedly turned on activation mode and turned it off every time the pressure reached 5×10^{-6} . Finally, we gave up and let the pressure go up as high as it wanted to, to a maximum of 3.5×10^{-5} . We activated the NEX Torr NEG at 550° C for 3 hours, and the pressure dropped to 3.6×10^{-6} Torr, corresponding to a capacity of 1.6 Torr·liter.
- (8) Cool down the system to room temperature.
- (9) Re-attach magnets, turn on ion Andrs D Herrera pumps, then turn them off.
- (10) Subsequently fire all TSP filaments to clean them (while the turbo pump is still pumping) in preparation for re-firing them a year or more later. We rotated firing one filament at the time, stopping when the pressure rose to the low 10^{-6} Torr level. After a few iterations, the pressure only rose to the 1×10^{-7} level and we deemed the filaments sufficiently clean.

After all this was done, we found that the pressure measured by the ion gauge was $2 - 3 \times 10^{-11}$ when the all-metal valve connecting the main chamber to the turbo pump was **open**, which is incredibly good for something connected to a turbo; from looking at the hydrogen partial pressure

on the RGA, we concluded that the main chamber was actually pumping hydrogen away from the front of the turbo pump. However, the pressure curiously **rose** to 5×10^{-11} when we closed the all-metal valve. With the valve closed, we turned the 6 L/s ion pump portion of the NEX Torr off and measured the pressure rise over time to verify that it was indeed pumping as specified. Therefore, we concluded that we had an unexpectedly-high noble gas load in the main chamber, and so we warn that for other groups with similarly large vacuum chambers, the 6 L/s in the NEX Torr pump may not be sufficient, and a regular large ion pump may be required. Additionally, we observed that the pressure rise in the main chamber from opening the gate valve with the oven on was initially much higher than what we would expect from the 300 L/s hydrogen pumping speed from the NEX Torr NEG and the 1 L/s conduction for hydrogen, but after several days of running the oven, the pressure rise was as expected. We concluded that there was likely some residual noble gas load, perhaps due to oven chamber being backfilled with argon for strontium loading, that quickly baked off within several days of operation.

In any case, we ordered a custom tee so that we could add a 150 L/s ion pump to the chamber. (RTFM: The pumping speed decreases with pressure and depends on what is being pumped. The labeled pumping rates correspond to different gases for different companies; the Varian StarCell pump was 150 L/s for hydrogen at higher pressures, but only 30 L/s for argon at 1×10^{-11} Torr. Still, this was 5 times better than the NEX Torr ion pump.) Also, Varian put the ion pump magnet on backwards when they refurbished it. So, if anybody else has trouble getting their refurbished ion pump to start, this may be a useful thing to check, before you follow tech support's advice to aggressively "hit the pump with a rubber mallet to try and shake some electrons loose."

We were also able to do some tests to estimate the pumping speeds of the various pumps. The turbo pumping speed for hydrogen was 45 L/s (and we calculated that it should not be conduction limited). After the next round of firing all TSP filaments to clean them during the bake and before activating any getters, the hydrogen partial pressure on the RGA decreased by a factor of 9, leading us to estimate that the conduction-limited TSP pumping rate *on the RGA* was approximately 360 L/s, and so the TSP pumping rate on the main chamber was at least that high.

As we were cooling down and after activating the NEX Torr NEG pump, we closed the all-metal valve to test our hydrogen pumping speeds (the titanium fired by the TSPs was saturated and not pumping at this point). At our pressure of 6×10^{-11} Torr, the StarCell hydrogen pumping speed was specified to be 40% of its nominal 150 L/s, or 60 L/s. Turning the ion pump off caused the pressure to rise to 8×10^{-11} Torr, which is consistent with the hydrogen being predominantly pumped by those two pumps. Therefore, we concluded that the Ti-Zr-V coating on the chamber was actually not doing any pumping, so perhaps it was not worth all the effort we went through to make sure that it was activated. The folks at Jefferson Labs quoted 0.1 L/ft² for the pumping speed, very low indeed. However, it may be an effective outgassing barrier, but without an identical uncoated chamber to compare it to, it is hard to know. Once we finished cooling down and closed the gate valve, the ion gauge measured a base pressure of approximately 5×10^{-12} Torr. We used the UHV-24P ion gauge (and corresponding controller) from Agilent (formerly Varian), as it seemed to be the only hot ion gauge that could measure pressures that low.

Unfortunately, when we unwrapped the chamber, we discovered to our horror that the bottom bucket window was completely covered with metal dust from the Ti-Zr-V chamber coating. Somehow something has been going wrong lately with Jefferson Laboratory's coating process; we have not heard about this happening to anyone else. The dust is fine (maybe even good) for vacuum, but obviously not ideal for optical lattices or high-resolution imaging. We vented the chamber, blew the dust out, and re-baked at 180°C, after the experts at Jefferson Lab assured us that baking would not produce any more dust. Jun thought (for no good reason) that 150°C would be a better temperature, but he let us go to 180°C. Sure enough, more dust flaked off the walls and fell on the bottom viewport. So, we vented yet again, blew dust off the bottom bucket window, baked at 150°C, and henceforth believe that Jun Ye is a magical wizard who should not be doubted. Since there was a compromise between pressure and metal dust on the viewport, we settled for 1×10^{-11} Torr and a handful of particles on the bottom viewport.

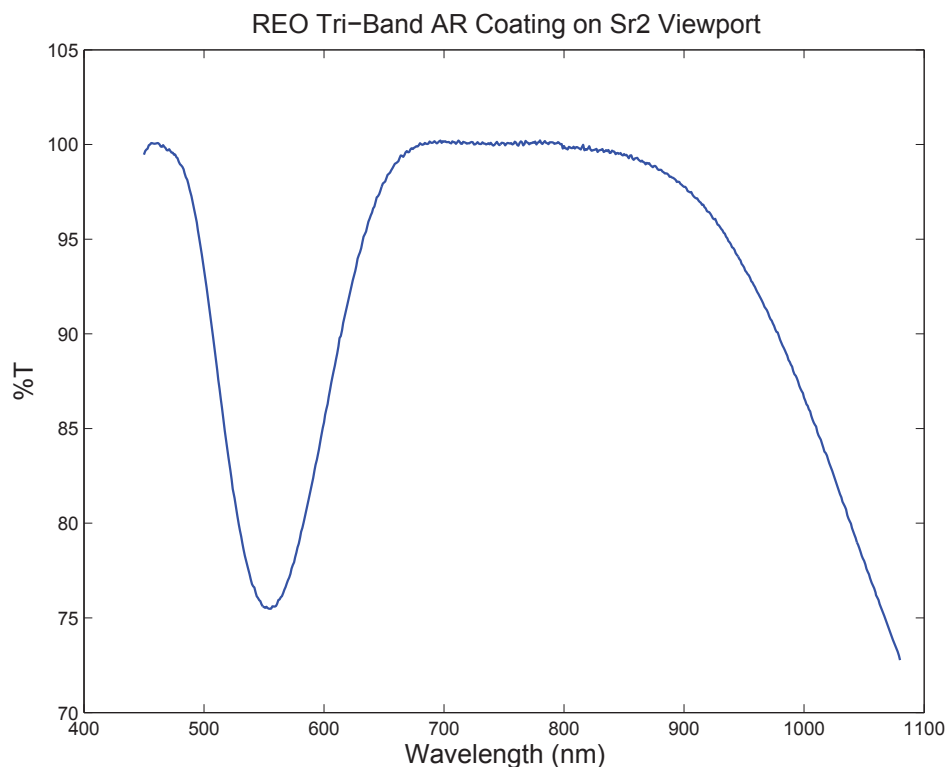


Figure 2.3: Spectrophotometer measurements of the tri-band coating by REO on a viewport from the old Sr2 chamber, which we had to vigorously clean via the Jun Ye method of hanging the viewport above a beaker of boiling solvents (yummmmm). Note the high transmission and how beautifully they achieved the target wavelengths of 461, 698, and 813 nm. Again, they don't make things like they used to. Note: NEVER put fused silica viewports in a sonicator. It might be fine for 7056 glass or other materials which have a different kind of glass-to-metal seal (an anonymous postdoc and senior graduate student on this experiment had sonicated many a viewport on their past experiments), but it is NOT fine for fused silica, where the glass is soldered to the metal. Something about sonicating it eats away the solder. Ask us how we know.

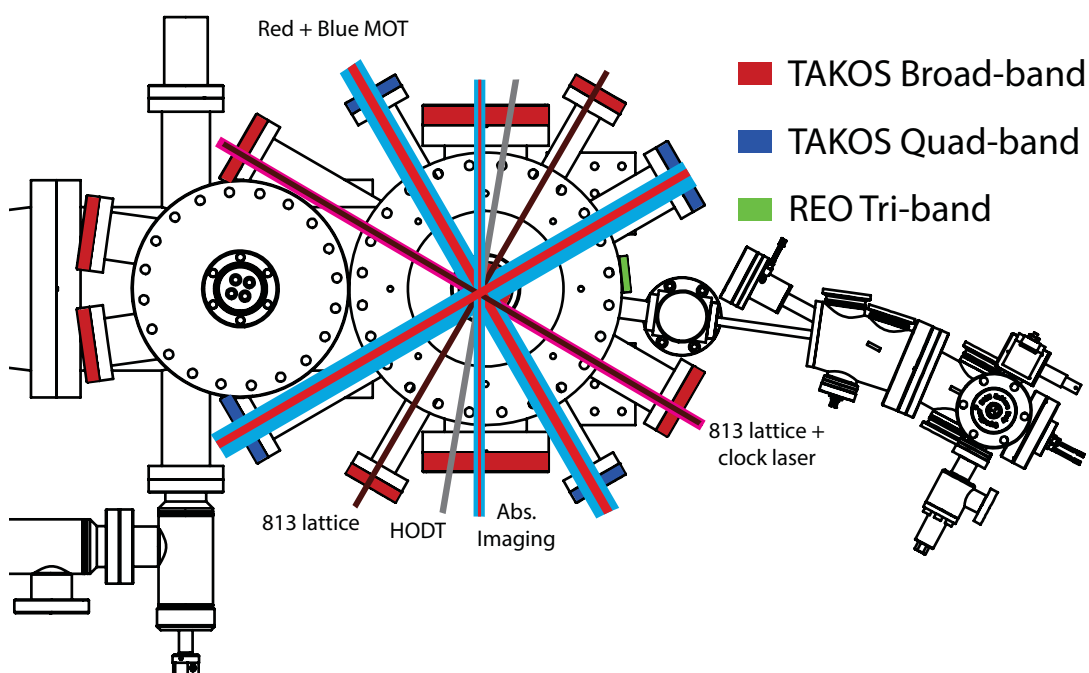


Figure 2.4: Illustration of the different AR coatings on the different viewports

2.2 Chamber mounts, custom breadboards, and other mechanical structures

The chamber was baked on a temporary 80-20 mounting structure. Once the bake was finished, we transported the chamber into the main lab and placed it on permanent mounts made of solid aluminum, shown in figure 2.5. Because the mounting tabs on the chamber were not welded on perfectly, and also following the customary wisdom that any mechanical structure referenced to a plane (i.e. the optical table) by more than three points must be done so with compliant material, we put “blue stuff”¹ between the chamber and the mounts, between the mounts and the optical table, and between the mounts and the clamps to the optical table. Since the magnetic coils would be clamped directly to the bucket windows (and therefore transfer vibrations to the chamber), the “blue stuff” has the added benefit of damping vibrations. The mounts were designed with cross braces and gussets to reduce any potential rocking or swaying vibrational modes. A slot was milled out of the bottom of the mounts to accommodate clamping to the optical table.

Two custom breadboards from the Technical Manufacturing Corporation (TMC) were ordered to fit snugly around the optical table as a “mezzanine” level, as shown in Figure 2.6. We ordered the 77 Series honeycomb core stainless steel breadboard in a 2 inch thickness, with holes on both the top and bottom, to help with future mounting structures and cable management. The breadboards were mounted on 3” diameter aluminum cylinders filled with lead ball bearings for vibration damping and welded shut. As with the chamber mounts, blue stuff was placed above and below the mezzanine mounts both to have a compliant material to minimize mechanical strain and for additional vibration damping. To make sure that both mezzanine breadboards were rigidly referenced to one another in order to minimize drifts in optical alignment, we connected them with two T-beams and one right angle brace. This also served to stiffen the board longitudinally to avoid “flapping” vibrational modes between the two halves of the breadboard.

Additional hardware upgrades included an optical table enclosure, as since we were planning on using a 50 Watt fiber amplifier for evaporation, we decided that it would be a good idea in

¹ ISODAMP C-1002-06 made by EAR, available from Raithbun Associates

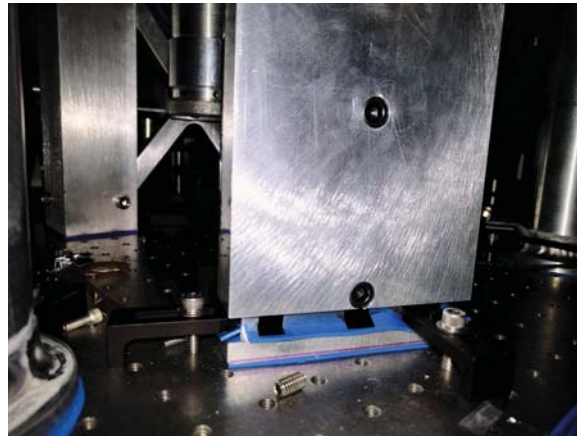
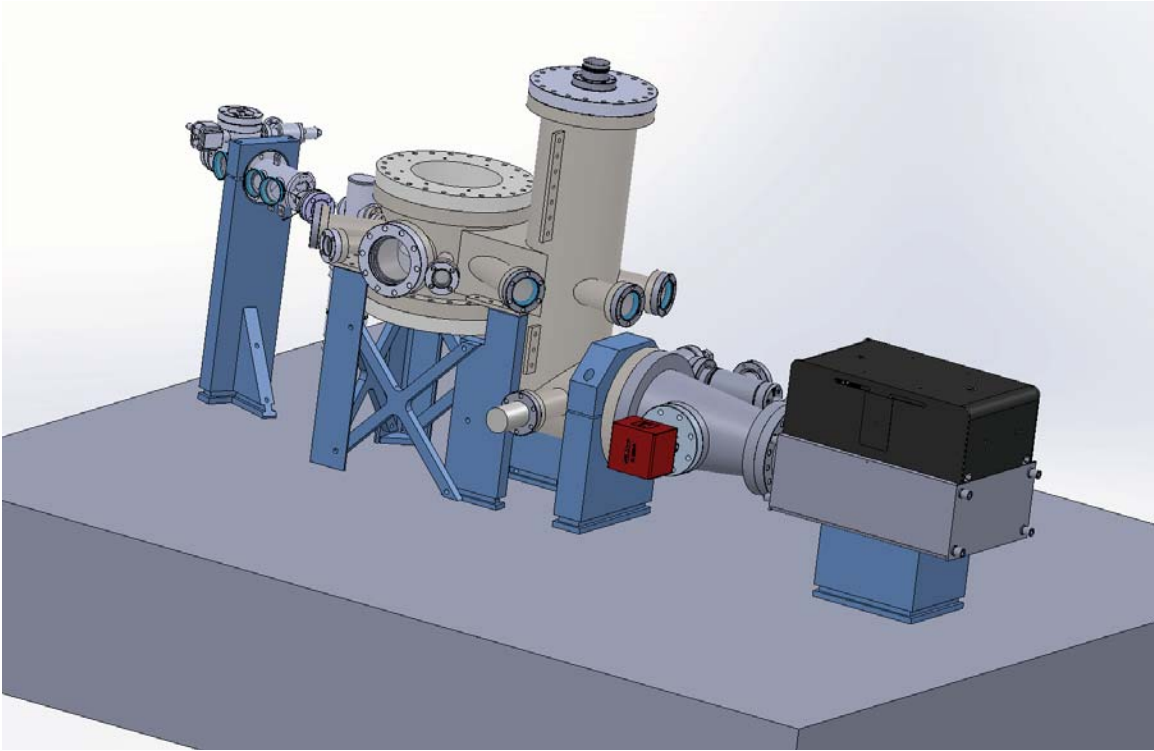


Figure 2.5: Top: CAD drawing showing the chamber mounts in blue. Bottom: Clamping the mounts to the optical table.

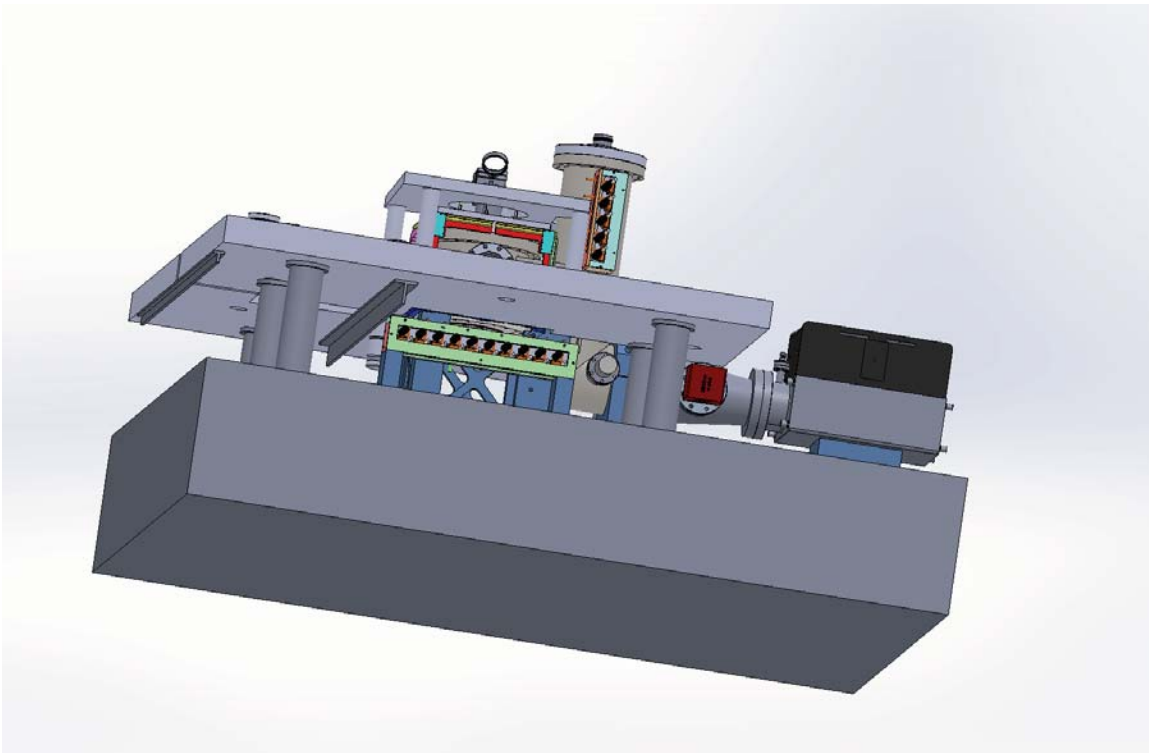
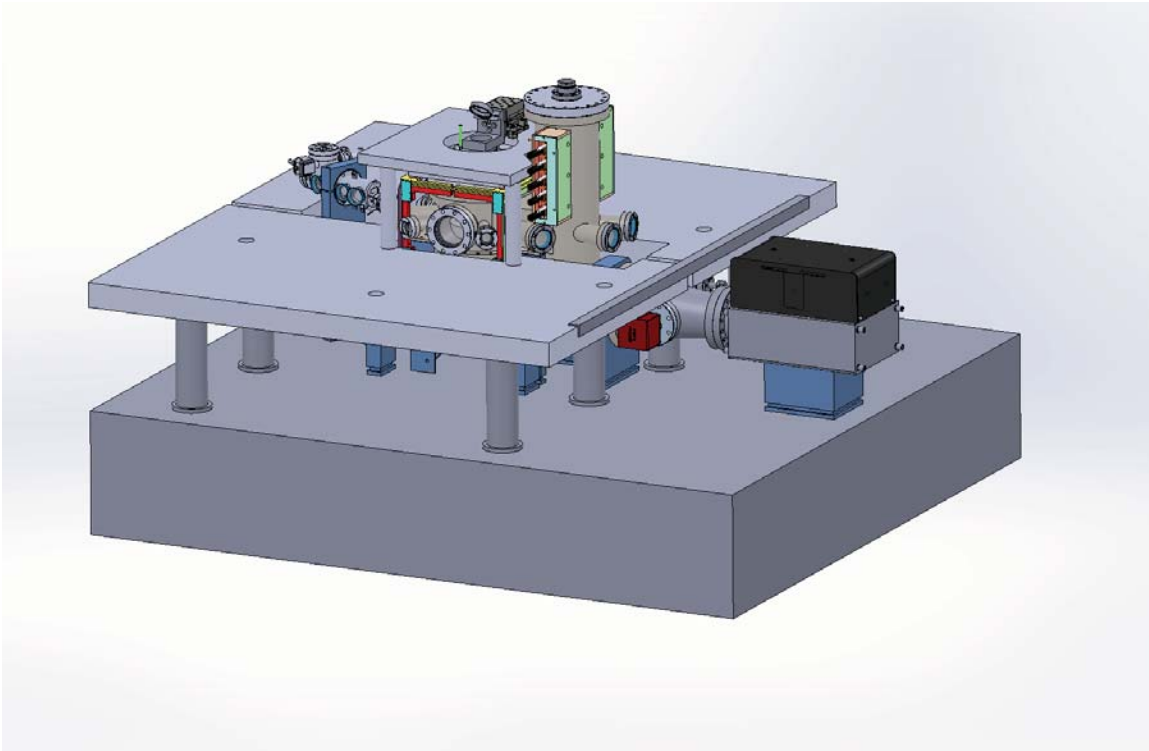


Figure 2.6: CAD drawings showing the full system design, including custom breadboards surrounding the chamber.

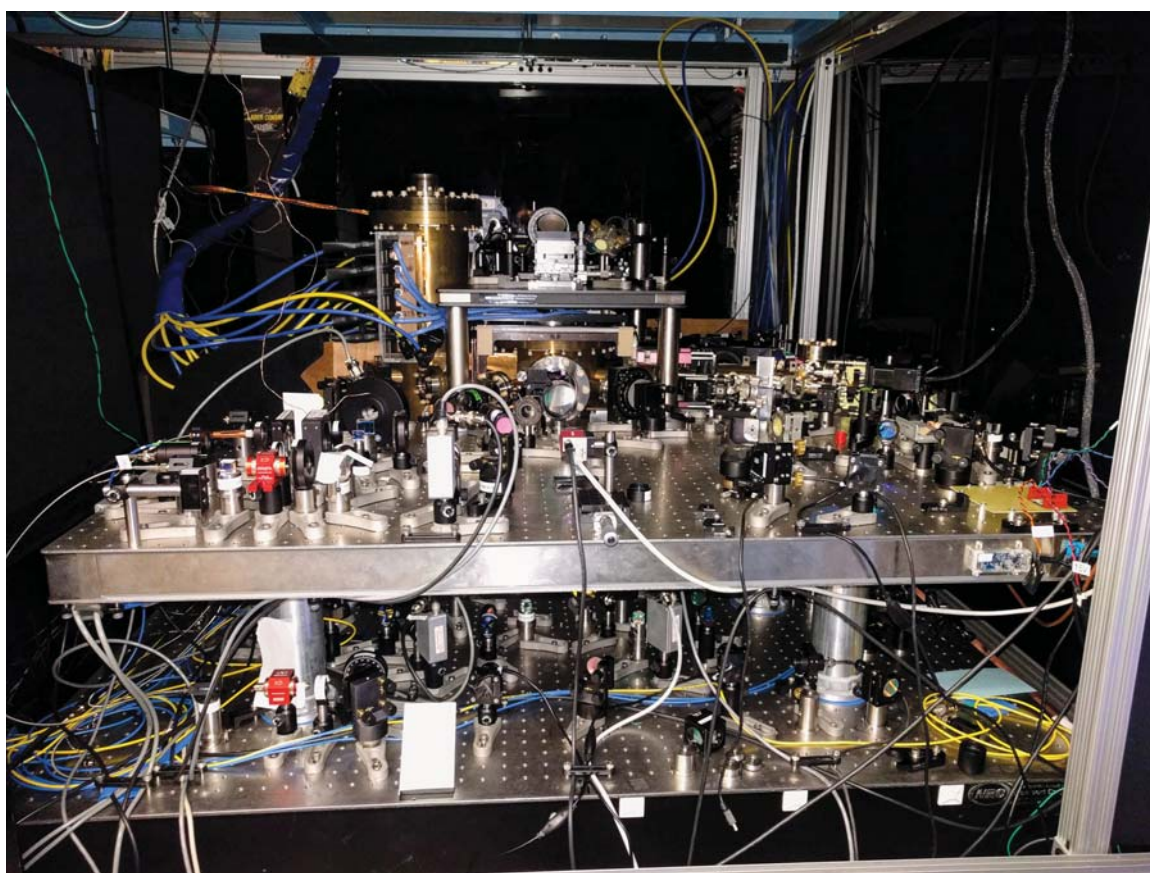


Figure 2.7: Top: Photo of a mezzanine post. Bottom: Photo of the full assembled system.

our dusty lab to run a HEPA filter so that dust wouldn't get burned onto all of the optics. The HEPA filter air intake is connected to a water-cooled heat exchanger to allow for the possibility of temperature stabilizing the optical table (the lab temperature has been stable enough that we have not been motivated to implement this yet).

2.3 Magnetic fields

The magnetic field control requirements for our experiment include bias/compensation coils for both canceling ambient magnetic fields and applying bias fields for atom manipulation; anti-Helmholtz coils for magneto-optical trapping; and new “quadrant coils” capable of applying strong bias fields along any axis, which, when used in conjunction with the gradients from the anti-Helmholtz coils, allow spectroscopic selection via the clock laser of a single lattice layer along any lattice plane.

2.3.1 Compensation/bias coils

The compensation coils were designed to be as compact as possible so as not to impede optical access. It is also desirable to be able to move the narrow-line red MOT, which operates at a magnetic field gradient of ≈ 3 G/cm by at least 2 mm to aid alignment the next stages of laser cooling and trapping, thus requiring a bias field capability of at least 2 G. The compensation coils in our previous generation experiment were very large (a total of ≈ 500 feet of 20 gauge wire) and so became hot to the touch when run at the full current of 3 A. Since the magnetic field scales as I^2N , where I is the current and N is the number of turns, while the power scales as IN , it is generally advantageous to have as many turns of wire as will fit.

A CAD drawing of the compensation coil mounts is shown in Figure 2.9. They were designed to fit snugly together around the vacuum chamber. The mount for one of the x-coils (shown in red) was machined from two separate pieces that fit together around the chamber, and, for mechanical clearance reasons, was wound before the viewports. As in [14], we used Duralco NM25 epoxy (500°F maximum temperature and free of magnetic particles and fillers), along with Kapton-insulated wire

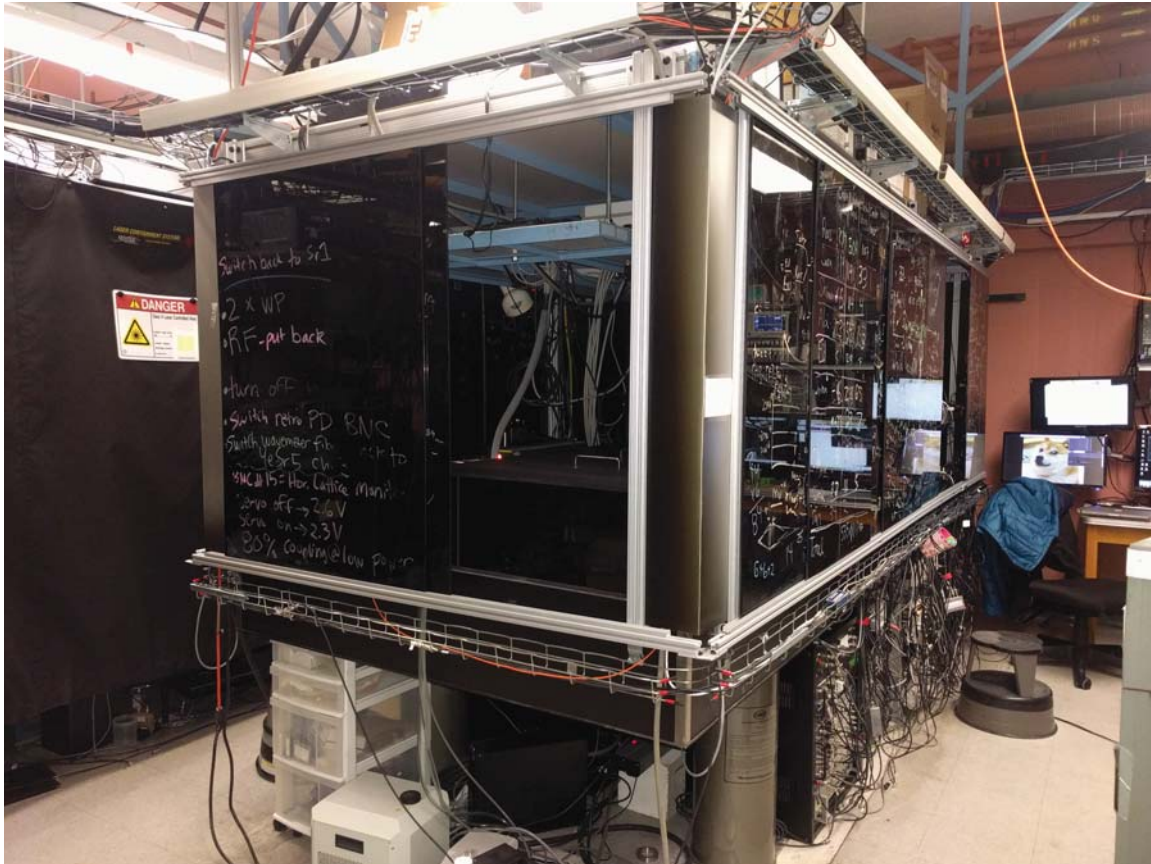


Figure 2.8: Top: Photo of the optical table enclosure, including sliding doors, top and bottom table trays and optical fiber enclosures. The black Plexiglass doors double as a whiteboard!

(400°F maximum temperature), so that the coil could be baked along with the rest of the vacuum chamber. The mounts were machined out of aluminum, so in order to achieve reasonably fast switching times of ≈ 1 ms, we had to add Teflon spacers (shown in Figure 2.10 to break the loop of aluminum and reduce Eddy currents. In retrospect, it might be better to just make the entire mounts out of some kind of high-temperature plastic.

The calculated magnetic fields from these coils are plotted in Figure 2.11, and achieve our design goals, reaching a fields > 4 G in all directions when operated at 3 A, with less than 1/4 of the power consumption of the previous design.

2.3.2 Anti-Helmholtz coils

The anti-Helmholtz coils (Fig. 2.12) serve the dual purpose of providing magnetic field gradients of 50 G/cm and 3 G/cm for the blue and red MOTs, respectively, as well as providing the capability to apply strong gradients of 0.62 G/(A·cm) for maximum gradients of 310 G/cm at 500 A, as shown in Figure 2.13. One can use a combination of magnetic field and high resolution spectroscopy to select a particular lattice layer in the z direction by running the top anti-Helmholtz coil only, which simultaneously provides a bias field and a gradient. Given an 813 nm magic-wavelength optical lattice with 406.5 nm spacing between sites, a 310 G/cm gradient gives a 12.6 mG magnetic field difference between adjacent lattice planes. From the $109 \cdot m_F \mu_B$ Hz/G differential g-factor between the ground 1S_0 and clock 3P_0 states, where μ_B is the Bohr magneton, there would be a 6 Hz clock shift between π -polarized lattice sites on adjacent lattice planes, which is easily resolvable with, for example, 1 Hz Fourier-limited clock spectroscopy.

To provide sufficient water cooling, each set of coils is wound with 3 sets of two layers, with the inner layer wound top to bottom, and the outer layer wound bottom to top. A CAD model showing the layers and dimensions is shown in figure 2.12. This way, the inner and outer layers spiral up and down in opposite directions with respect to the horizontal plane, thus largely canceling stray transverse fields resulting from that tilt. Additionally, each set of 2 layers is designed with decreasing height, so that each set has approximately the same length, and thus heat load. The 3

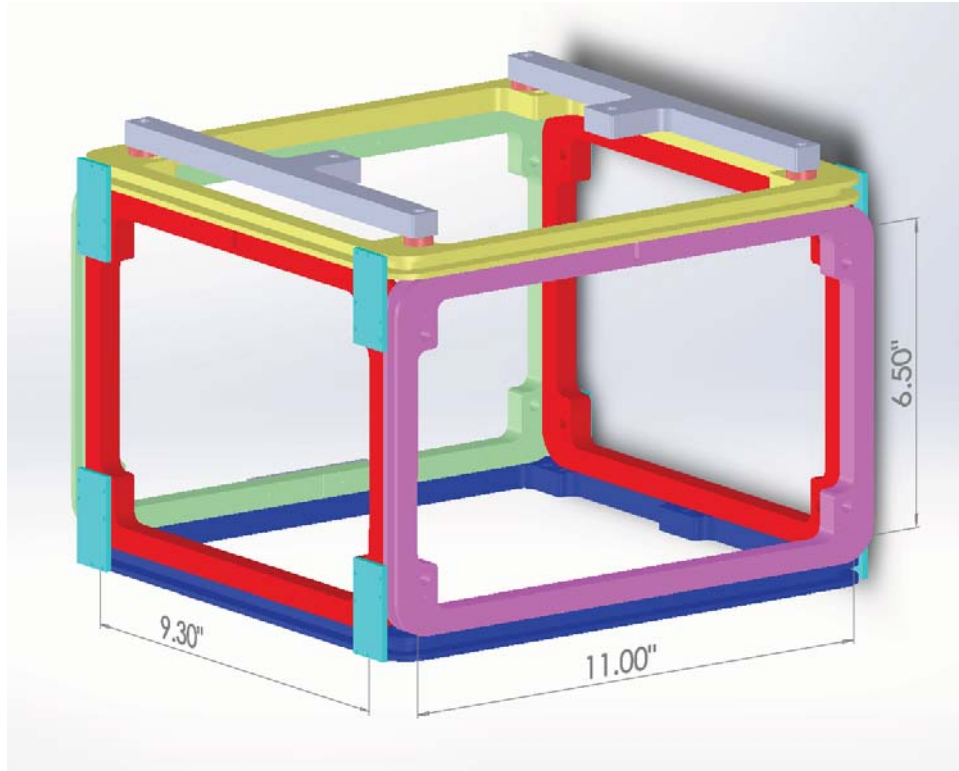


Figure 2.9: CAD model of the compensation coils.

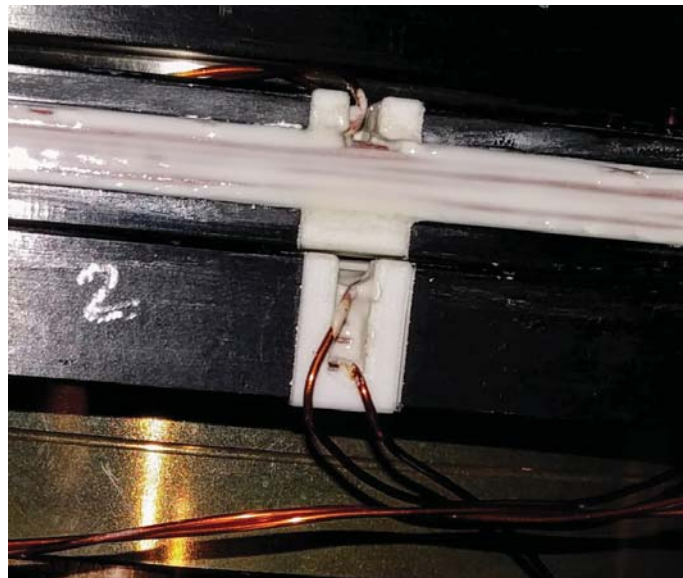


Figure 2.10: Teflon spacers in the aluminum compensation coil mounts, added to reduce eddy currents.

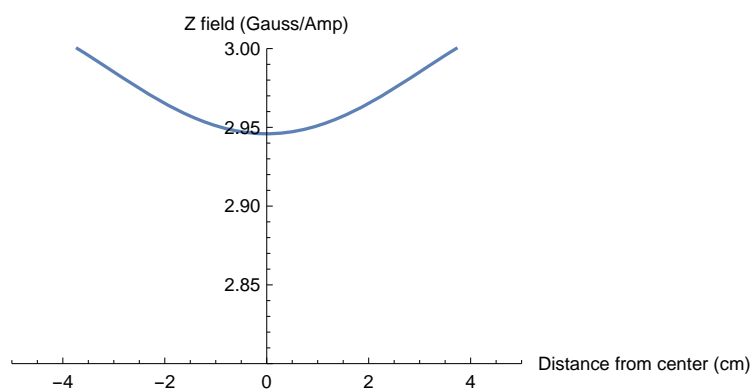
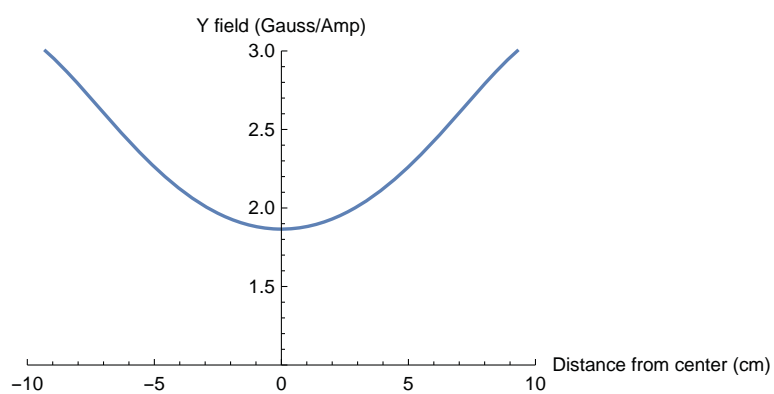
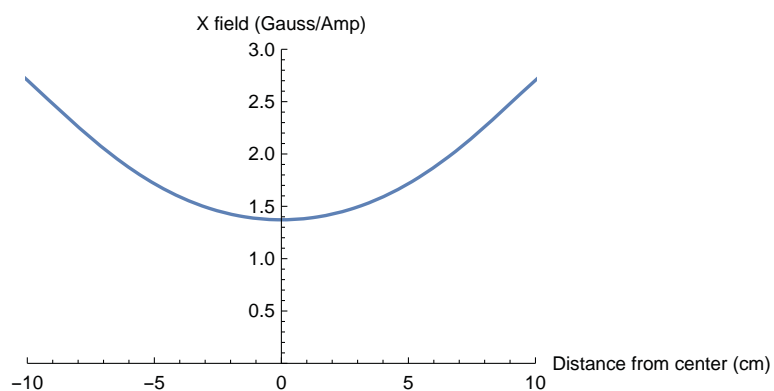


Figure 2.11: Calculated magnetic fields for the compensation coils.

sets of coils are connected electrically in series and connected to the water cooling in parallel.

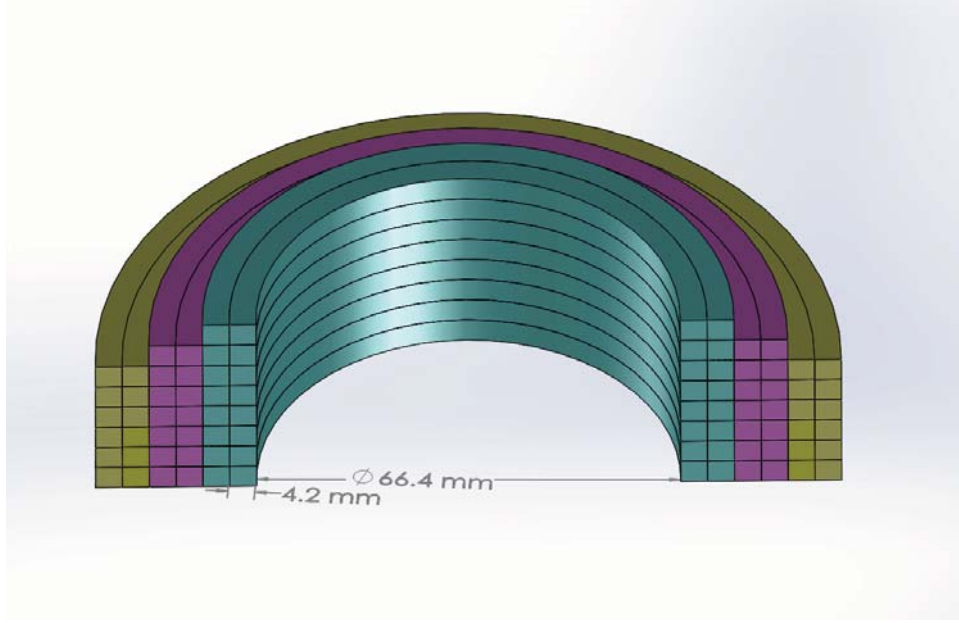


Figure 2.12: Anti-Helmholtz coil design.

2.3.3 Quadrant coils

The anti-Helmholtz coils apply a gradient dB_{AH}/dx in the \hat{x} and \hat{y} directions, and a gradient $2 \cdot dB_{\text{AH}}/dx$ in the \hat{z} direction. In order to effectively select a lattice layer along, for example, the \hat{x} direction, we must ensure that the magnitude of the field $|B|$ varies with \hat{x} more quickly than it varies with \hat{y} or \hat{z} . Then, if the atom cloud size is sufficiently small, all of the atoms along the plane with a certain \hat{x} value will have the same transition frequency, while all subsequent planes along the \hat{x} direction will be spectroscopically resolved. This can be accomplished by applying a large bias field B_{bias} along the \hat{x} direction so that,

$$|B(x, y, z)| = \sqrt{\left(B_{\text{bias}} + \frac{dB_{\text{AH}}}{dx}x\right)^2 + \left(\frac{dB_{\text{AH}}}{dy}y\right)^2 + \left(2\frac{dB_{\text{AH}}}{dx}z\right)^2}. \quad (2.1)$$

For small excursions from the center,

$$B_{\text{bias}}\frac{dB_{\text{AH}}}{dx}x \gg \left(\frac{dB_{\text{AH}}}{dx}y\right)^2, \left(2\frac{dB_{\text{AH}}}{dx}z\right)^2, \quad (2.2)$$

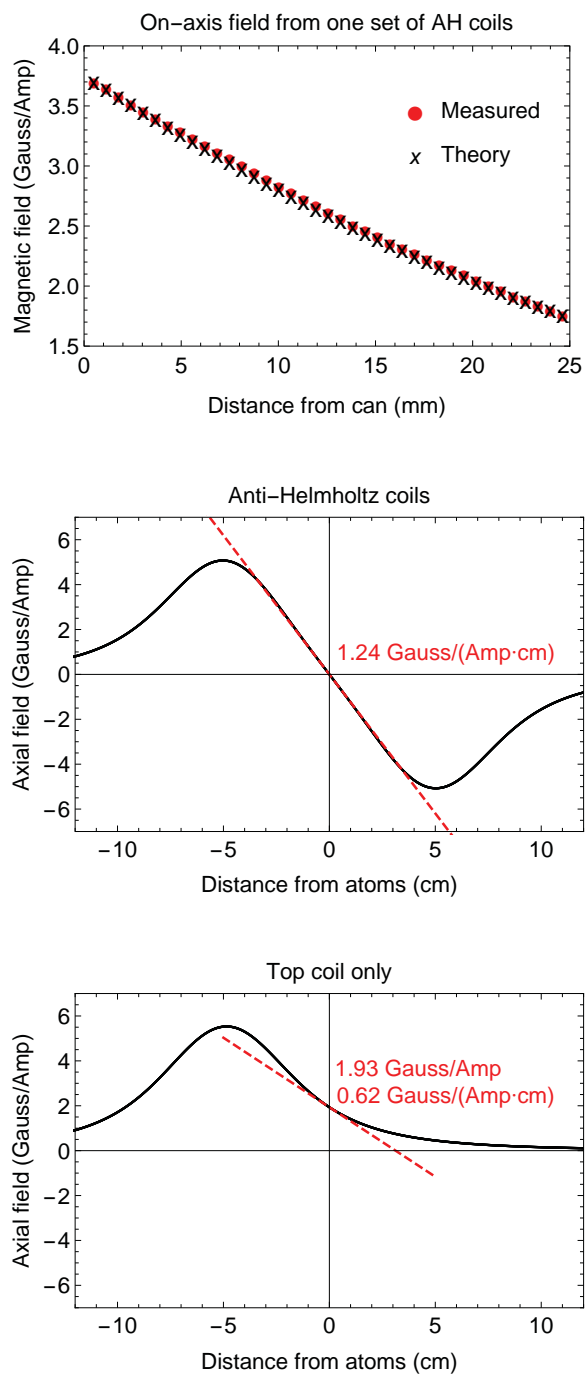


Figure 2.13: Anti-Helmholtz coil comparison of measurement and theory, gradient from both coils, and bias field and gradient from running the top coil only.

and so for sufficiently small y and z , $|B|$ varies linearly with x and does not change with y and z :

$$|B(x, y, z)| \approx B_{\text{bias}} + \frac{dB_{\text{AH}}}{dx}x \quad (2.3)$$

Here, we introduce “quadrant coils”: a scheme for applying large bias fields in any direction, using only coils in the top and bottom bucket windows. A CAD model of the coil shape is shown in Figure 2.14 and a schematic depicting the principle of operation is shown in Figure 2.15. To visualize how these coils work, we assume that the fields produced by wires farther away from the atoms are *much* less significant than the fields produced by wires closer to the atoms (i.e. the wires closest to the bucket window viewports) and can be ignored. Then, we can group these wires into a pair of effective Helmholtz coils, where each effective coil in the Helmholtz pair is shown by the blue and green arrows in Figure 2.15, which also indicate the direction of current flow. Therefore, by changing the direction of current flowing through these 8 quadrant coils, one can apply bias fields in the \hat{x} , \hat{y} and \hat{z} directions. Since a horizontal layer (a plane of constant z) can be selected by running the top anti-Helmholtz coil only, for now, we have only implemented the \hat{x} bias field and \hat{y} bias field configurations. One must simply reverse the direction of current in 4 of the 8 quadrant coils to change between these two orthogonal configurations.

In order to construct the quadrant coils, the wires are wound around square Teflon jigs, then pressed into an arc of the correct radius of curvature to fit inside the bucket window, as shown in Figure 2.16. We tested both the anti-Helmholtz and quadrant coils using flowmeters and found similar flow rates, and so conclude that this method of winding then clamping does not appreciably occlude the hollow core used for water cooling.

The efficacy of this strategy for producing strong bias fields at the atoms depends on the validity of the assumption that the inner wires are much closer to the atoms than the outer wires, so it is desirable to place the quadrant coils as close to the atoms as possible.

In order to simulate the magnetic fields produced by these oddly-shaped coils, a CAD model was imported into the COMSOL simulation software. To simplify the computation, all 5 turns of coils were lumped into one solid object with a constant current flux density of 5 times the current



Figure 2.14: CAD model showing one set of quadrant coils. The two sets of quadrant coils are placed inside the bucket windows, on opposite sides of the atoms.

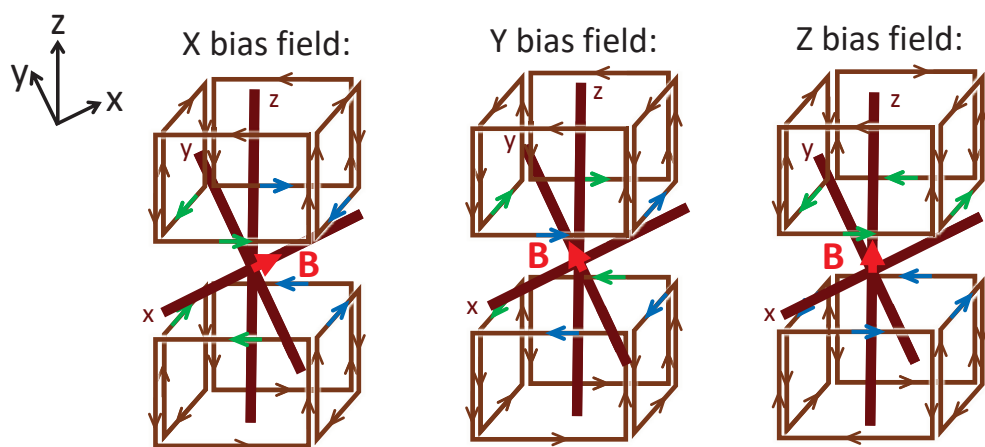


Figure 2.15: Schematic showing how the quadrant coils can be used to generate a bias field in any direction.

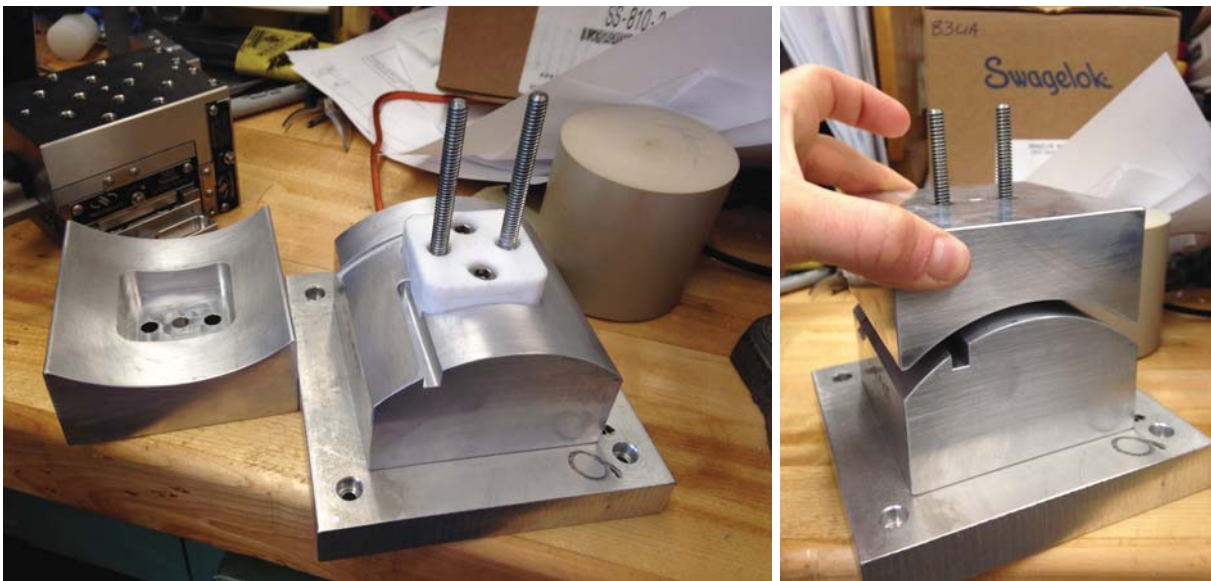


Figure 2.16: Clamps used to bend the quadrant coils into the correct shapes.

in one turn of wire, as shown in Figure 2.17. We had some engineering compromises. Originally, I had assumed an optimistically-small radius of curvature for winding the coils around the square edges, and I assumed that the coils would be touching. However, just some slight adjustments to the CAD model to account for reality had a significant effect on the maximum achievable bias field, reducing it by a factor of 3. Figure 2.18 plots the COMSOL results for the fields as a function of arc length plotted along short lines through the center of the chamber along the x and z lattice axes. The coils still produce a bias field of $0.08 \text{ G}/(\text{A}\cdot\text{cm})$, corresponding to a bias field of 40 G at 500 A, which will be sufficient for our needs.

2.3.4 Single layer selection

Now we consider how the anti-Helmholtz and quadrant coils may be used together to select a single layer of the 3D optical lattice in any direction. Figure 2.19 shows the atom cloud, viewed from the side, where a 310 G/cm (620 G/cm) gradient is applied in the x and y (z) directions, and a 40 G bias field is applied in the x direction to select a single layer along that direction. As one can see, there is still some curvature along the y and z directions of in the surfaces giving a constant $|B|$, but the 40 G bias field largely flattens this out so that the magnetic field value is generally constant over a lattice layer. In Figure 2.20, we plot the magnetic field as well as contour lines along vertical and horizontal slices through the atom cloud. Finally, Figure 2.21 shows that when the lattice layers in the x-direction are resolved by $\approx 6 \text{ Hz}$, the clock frequency varies by ≈ 2 over a lattice layer for a cloud size of ± 50 lattice sites ($40 \mu\text{m}$) in the x and y directions, and ± 25 lattice sites) ($20 \mu\text{m}$) in the z direction.

2.3.5 Control electronics

The coil switching and current servo electronics for both the quadrant and the anti-Helmholtz coils are shown in Figures 2.22 and 2.25. First we explain how the switching circuit works. Figure 2.23 shows truth tables for both the quadrant coils and anti-Helmholtz coils explaining how the two logic signals L1 and L2 determine the behavior of each switching circuit, as well as the logic

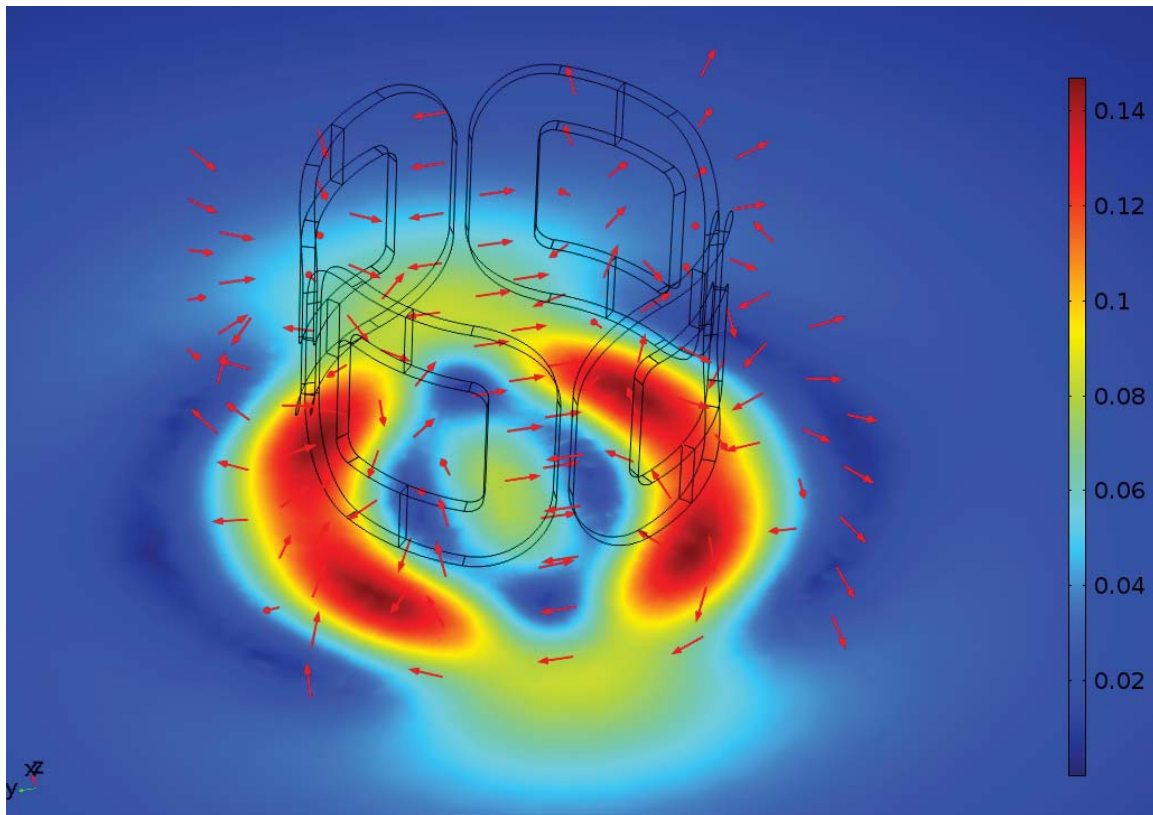


Figure 2.17: 3D plot of the field produced by the actual quadrant coils.

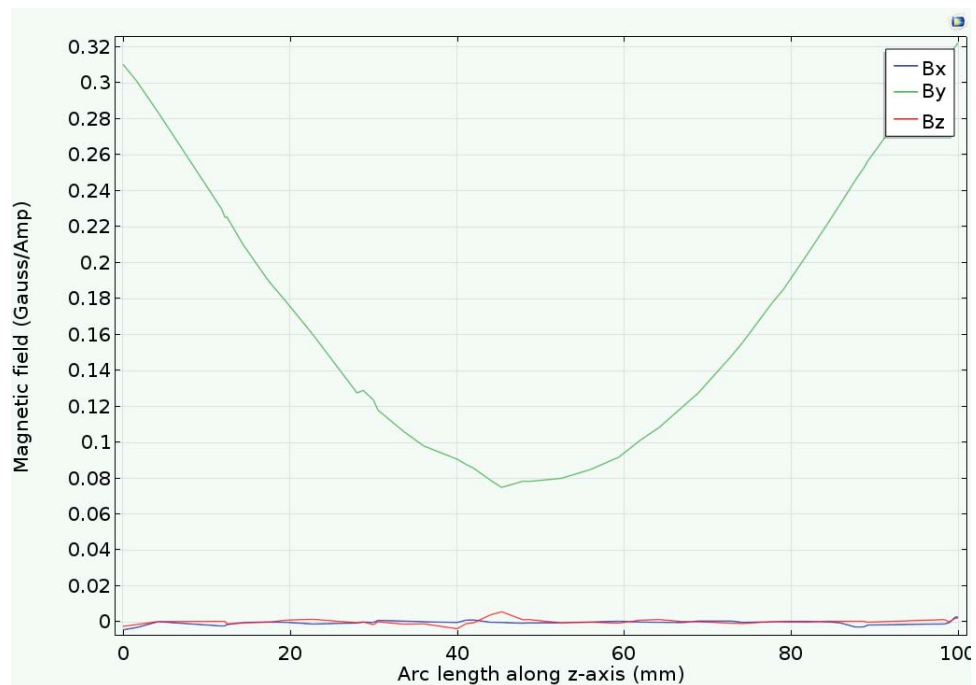
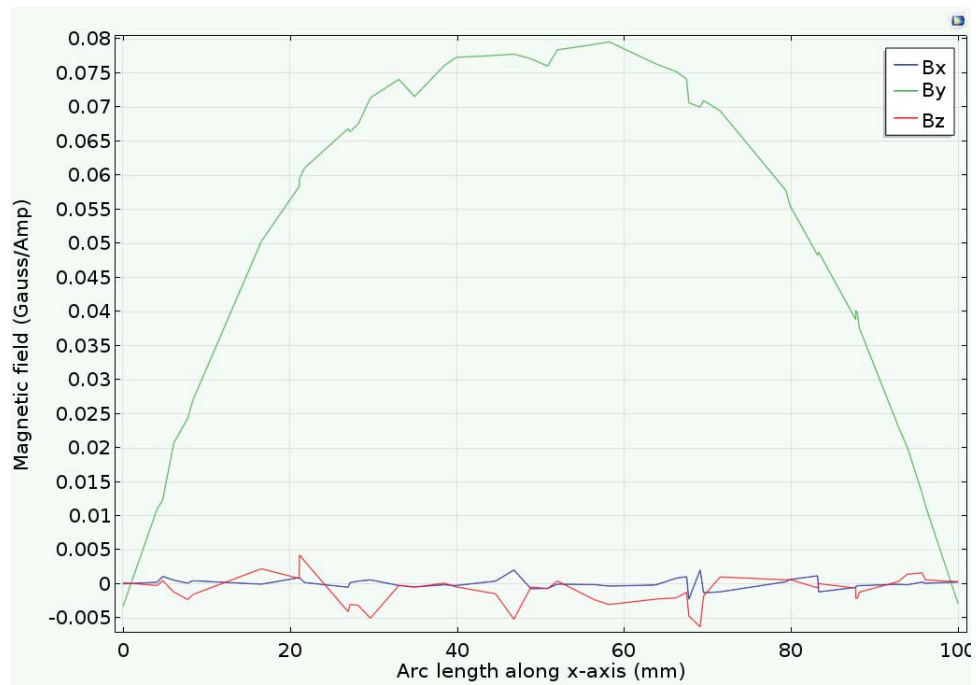


Figure 2.18: Magnetic field generated by the actual quadrant coils (after some engineering compromises) when configured to give a bias field in the y-direction. Plots were generated using a COMSOL simulation based on the coil geometry imported from a CAD model.

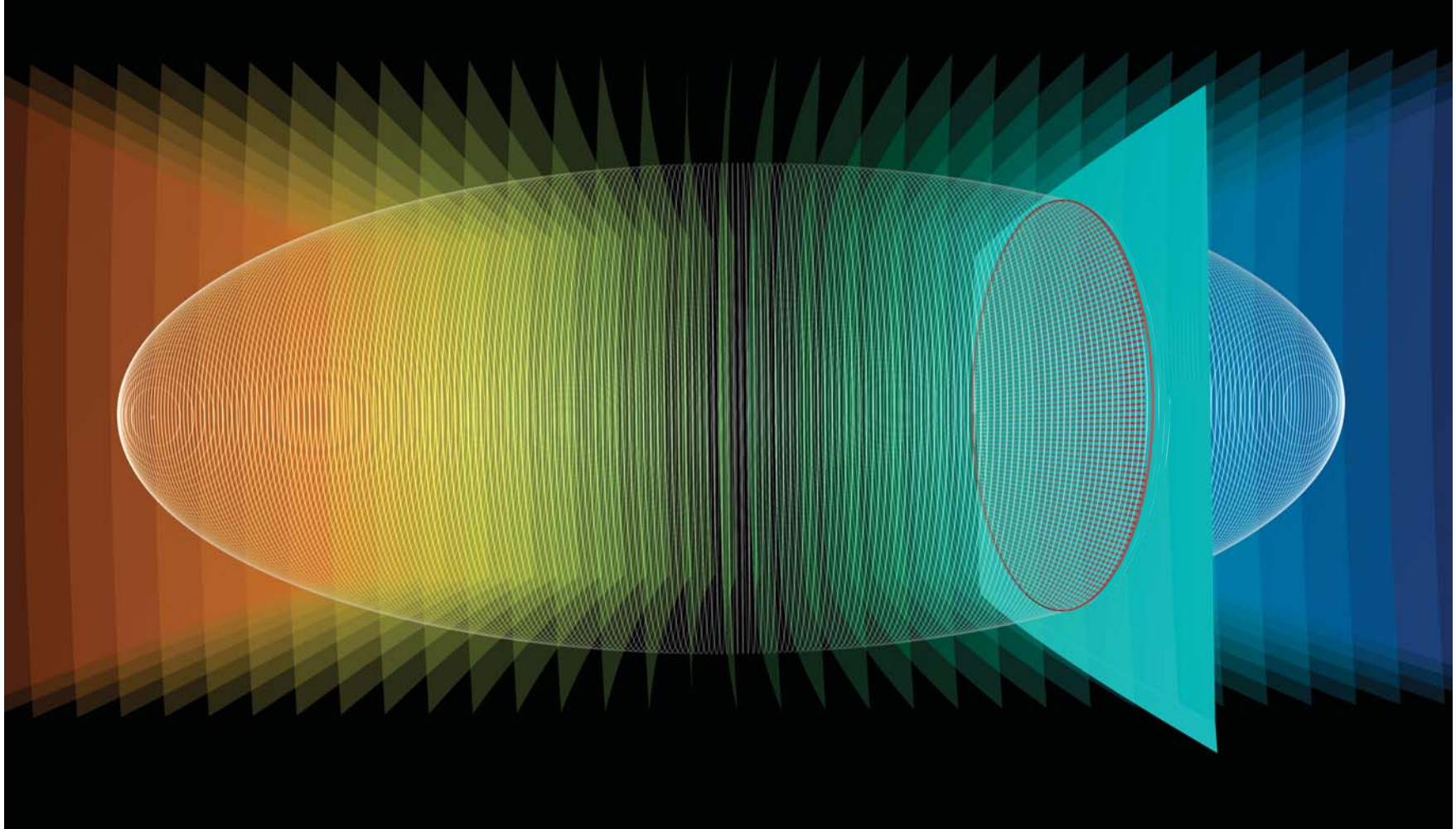


Figure 2.19: A to-scale schematic showing the selection of lattice layers in the x-direction. The white circles indicate lattice layers in the x-direction, and the multicolored surfaces are 3D contour surfaces of constant magnetic field. The atoms in one particular spectroscopically-selected layer are shown in red.

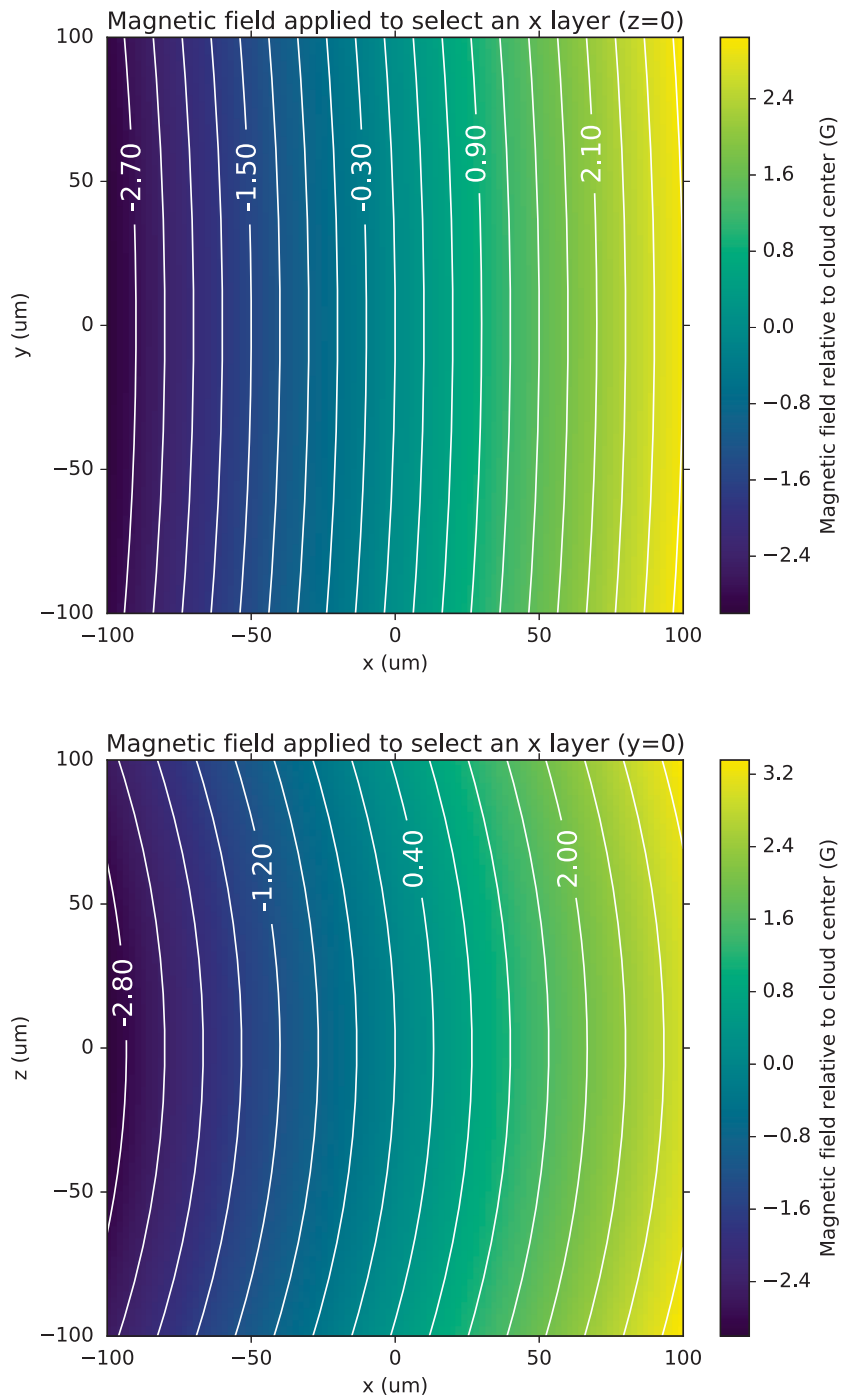


Figure 2.20: A gradient along all directions from the anti-Helmholtz coils, plus a strong bias field along the direction causes the magnitude of the magnetic field to vary predominantly along the x direction.

Range of clock transition frequencies due to magnetic field curvature

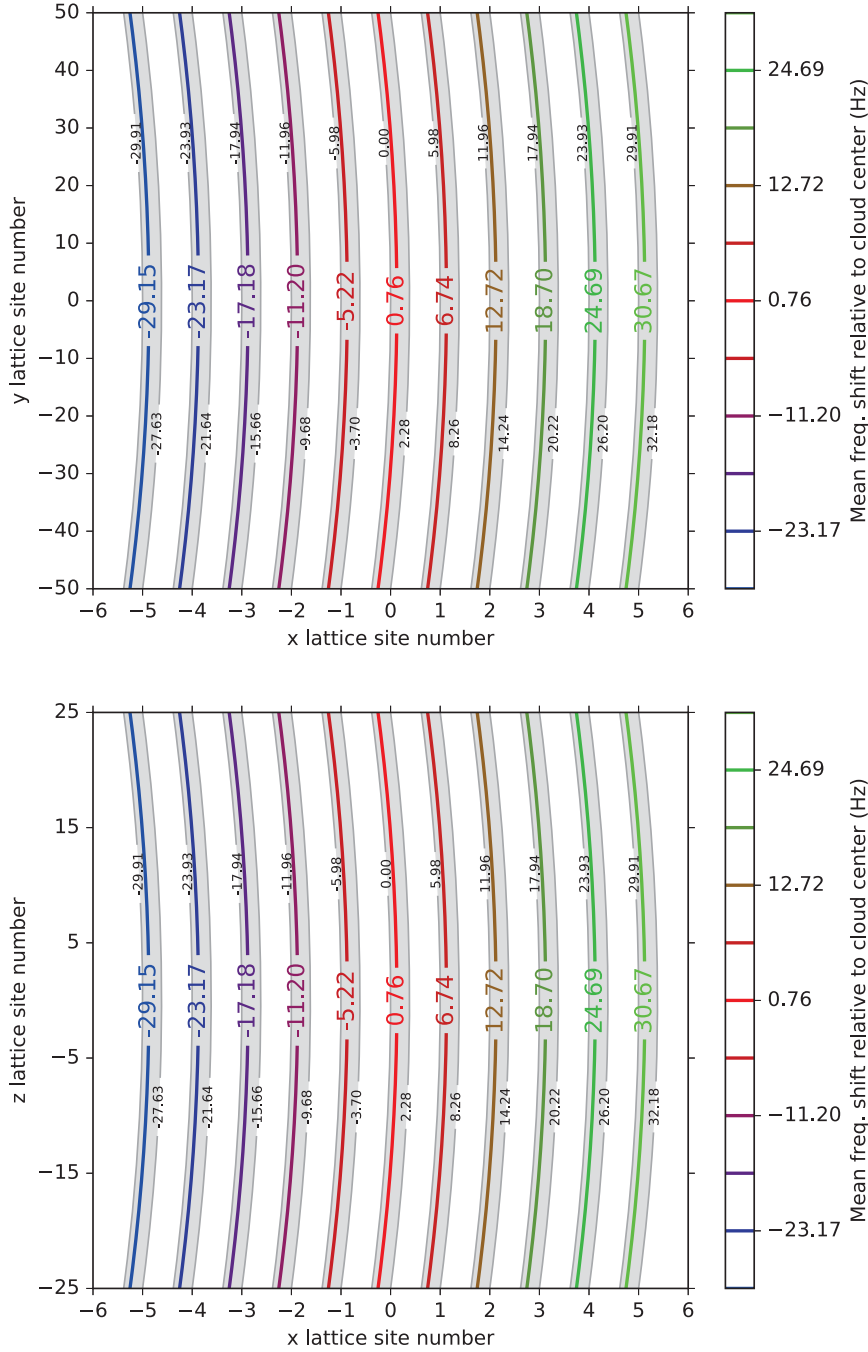


Figure 2.21: A large bias field in the direction of layer selection minimizes the gradient in the absolute value of the magnetic field along the two orthogonal directions, with the goal of achieving a constant clock transition frequency within the entire lattice layer that is to be selected. However, for lattice layers in the x direction that are resolved by 6 Hz, there is still a ≈ 2 Hz spread in transition frequencies along the y direction, and a ≈ 2 Hz spread in transition frequencies along the z direction. Therefore, when applying these techniques, the cloud size must be kept to within ± 50 and ± 20 lattice sites along the x/y directions and the z direction, respectively. This corresponds to atom cloud dimensions of $40 \mu\text{m}$ in the x and y directions, and $20 \mu\text{m}$ in the z direction.

inverters and MOSFET drivers that distribute the logic signals to the MOSFETs. Figure 2.24 provides a schematic description of how the two circuits work for each logic configuration.

The MOSFETs essentially act as shorts when given a logic high (5V) control signal and as open circuits when given a logic low (5V) control signal, so to help visualize how the circuit works, we represent them as normal switches that are closed for logic high and open for logic low. Both circuits use logic L1 to control the overall on/off state. For the quadrant coils, an H-bridge circuit controlled by logic L2 is used to reverse the current through half of the coils (as shown for switching between \hat{x} and \hat{y} bias fields in Figure 2.15) in order to switch between providing a bias field in the \hat{x} direction and the \hat{y} direction. For the anti-Helmholtz circuit, logic L2 is used to run with either the top coil only (for magnetic field gradient selection) or with both the top and bottom coils.

The MOSFETs that we are presently using for current switching are the Infineon IPT007N06N, which are rated up to 300 A. (These will need to be upgraded if we choose to use a higher-current power supply.) The MOSFETs are driven using an an LT1010 buffer chip driving a IXYS FDA217 photovoltaic MOSFET driver. The IT 400-s Ultrastab Hall probe is used to measure the current. It outputs a sense current of 1/2000 of the measured current, which is then run across a stable 20 Ω resistor to give a sense voltage of -1/100 V/A. The sense voltage then goes into the current servo shown in Figure 2.25 where I changed R6 so that the overall transfer function is -3/100 A/V. The actuator is the SKM900GA12E4 IGBT by Semitrans, which can handle 2kW of power dissipation. It is recommended to put a diode between the gate and the source, as word on the streets of JILA is that this prevents the IGBT from blowing up. The power supply used is the Sorensen DHP60-330. It is important to set the current limit high enough so that the power supply does not switch between constant current mode and constant voltage mode, which can result in very large (4000 amp) current spikes. The power supply should remain in constant voltage mode at all times.

Due to the large inductive load L of the coils, suddenly switching them off produces a back-EMF much larger than the maximum specification of the MOSFETS (which was accidentally experimentally verified!), so it is necessary to include varistors as shown in Figure 2.22 which will limit the voltage to the clamping voltage V_{var} of the resistor. Then the rate of change of current

through the coils will be limited to $dI/dt = -V_{\text{var}}/L$ so the current decreases linearly from an initial current I_0 with a switching time $T_{\text{off}} = I_0L/V_{\text{var}}$ and the MOSFETs do not explode.

2.3.6 Mounting and water cooling

As shown in Figures 2.26 and 2.27, the anti-Helmholtz and quadrant coils were potted inside Teflon cans using Duralco NM25 epoxy. This way, if the main chamber needs to be re-baked at all, the coils can withstand the heat and do not need to be removed from the bucket windows. Because the coils can vibrate when switched on and off, it is important to include damping material in the mounting structure. The Teflon cans are clamped inside the bucket windows with set screws that cause the Teflon can to push down on a layer of Viton foam placed between the can and the inside of the bucket window.

The coils are made from hollow wires which allow them to be water cooled from the inside. The square-shaped magnet wire is soldered inside a round adapter that allows for the connection to regular 1/4" copper tubing that can be connected using normal Swagelok. As shown in Figures 2.28 and 2.29, the wires are connected to manifolds that provide both electrical and water cooling connections.

Because any kind of failure in the water cooling system could cause a catastrophic disaster in the lab, we made sure to include a thorough interlock system, detailed in Figure 2.30. Each portion of water-cooled coil has an attached thermocouple, which then is read by a Keithley 2701 digital multimeter (via the Keithley 7710 differential multiplexer). If any of the coil temperatures exceeds a threshold of 22°C, it causes a TTL output signal to drop low. Our two high-power water-cooled 1064 nm fibers also have thermocouples going to the same interlock, as they can burn if their temperature becomes too high (due to misalignment, etc). Originally, I attempted to make my own hardware-based interlock based on the AD595 thermocouple reader chip, comparators, and a series of digital logic chips. However, since thermocouples sense such small voltages and are thus susceptible to electrical pickup and grounding issues when traveling across the lab, this is not such a trivial task: the interlock tripped every time the magnetic coils switched or somebody

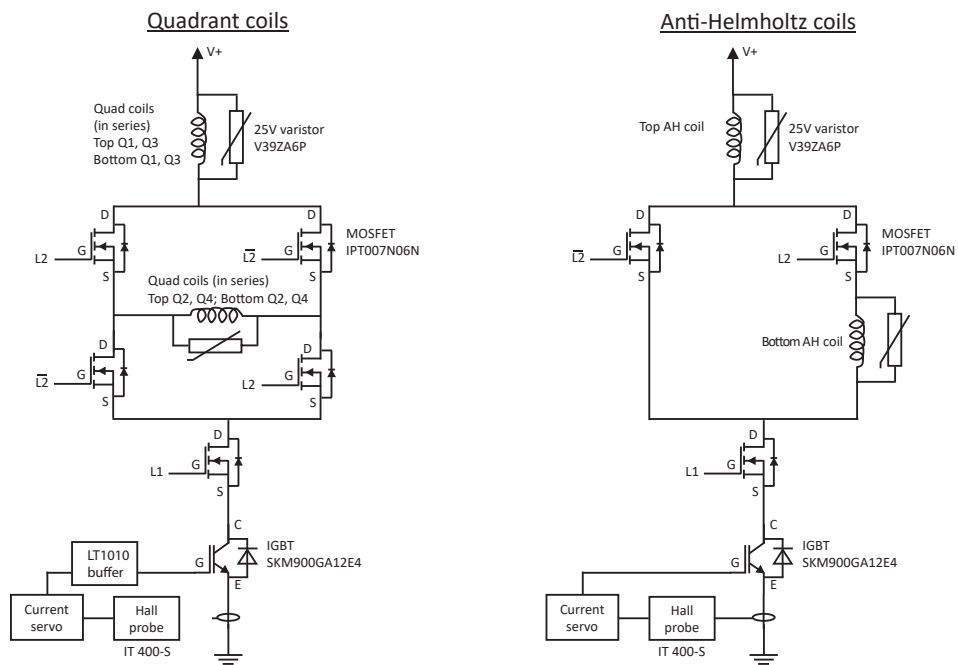


Figure 2.22: Schematic of coil switching and current servo electronics. The Anti-Helmholtz electronics switch between the anti-Helmholtz and top coil only configurations. The quadrant coil electronics switch between configurations that give a bias field in the x and y directions.

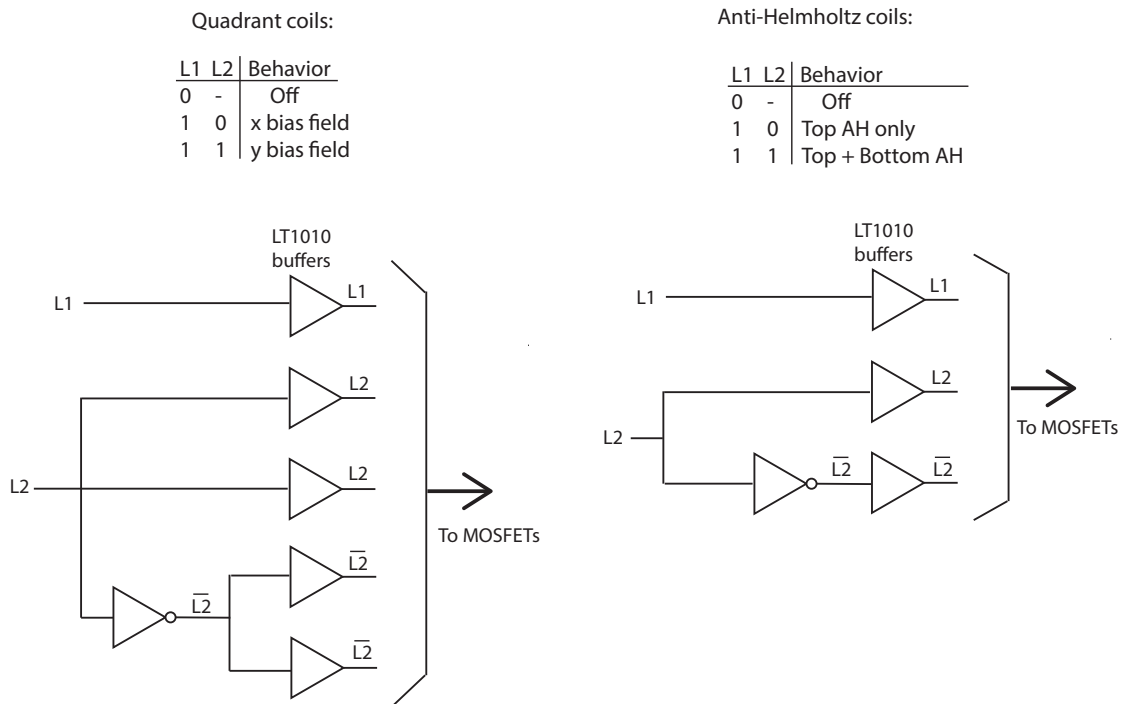


Figure 2.23: Truth table, inverters, and buffers for driving the MOSFETs for both the quadrant coils and the anti-Helmholtz coils.

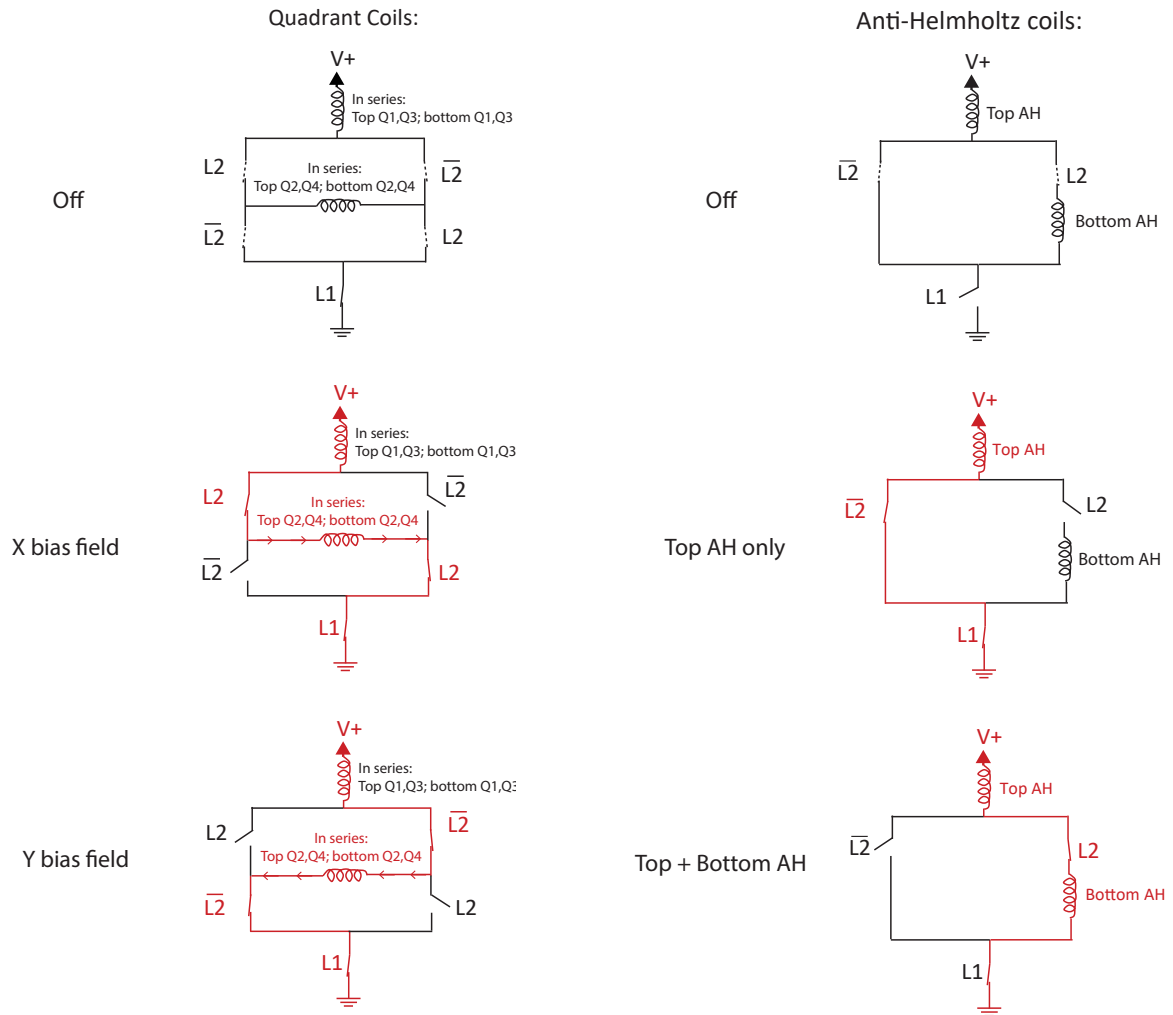


Figure 2.24: Schematic showing the principle of operation of both the quadrant coils and the anti-Helmholtz coils. Here, all the MOSFETs are depicted as switches controlled by the corresponding logic signals. The color red is used to indicate components that have current flowing through them; the color black is used to indicate components with no current flowing through them. Arrows indicate the direction of current flow. The logic signal $L1$ is used on both coils to control the overall on/off state. For the quadrant coils, $L2$ is used to control the H-bridge which can reverse the direction of current through half of the coils, thereby switching the bias field from the x direction to the y direction. For the anti-Helmholtz coils, $L2$ is used to either turn on the bottom coil or short it out so that no current flows.

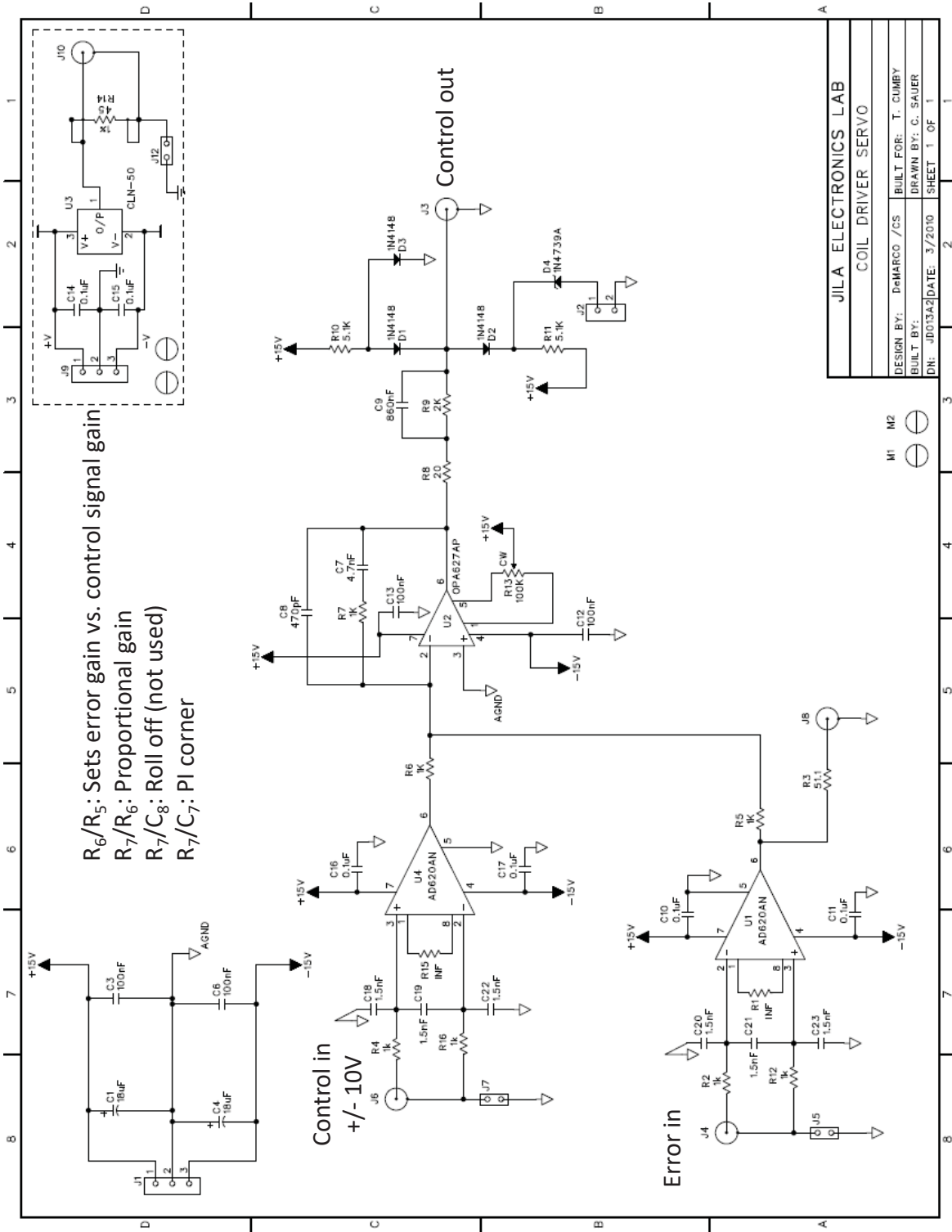


Figure 2.25: Circuit diagram for the servo used to control the current in the anti-Helmholtz and quadrant coils. For now, I have changed R6 to 3 kΩ in order to use more of the $\pm 10V$ range of the DAC output, giving $-3/100$ Amp/Volt.

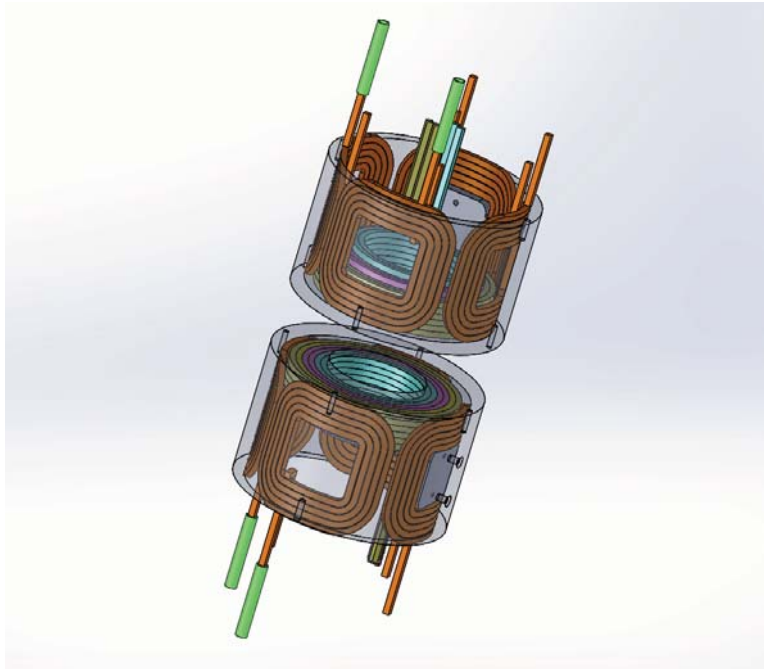


Figure 2.26: CAD model showing all magnetic coils inside the two Teflon cans that are clamped inside the top and bottom bucket windows.

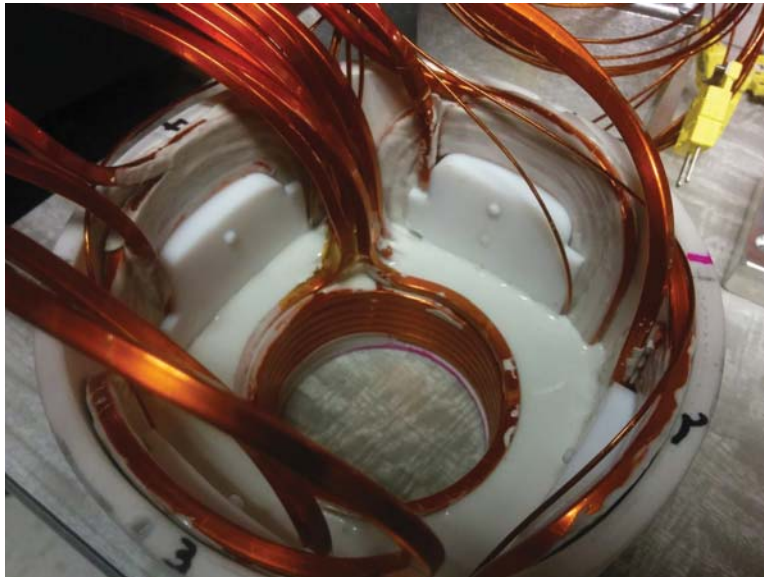


Figure 2.27: All bucket coils potted with epoxy in the Teflon can.

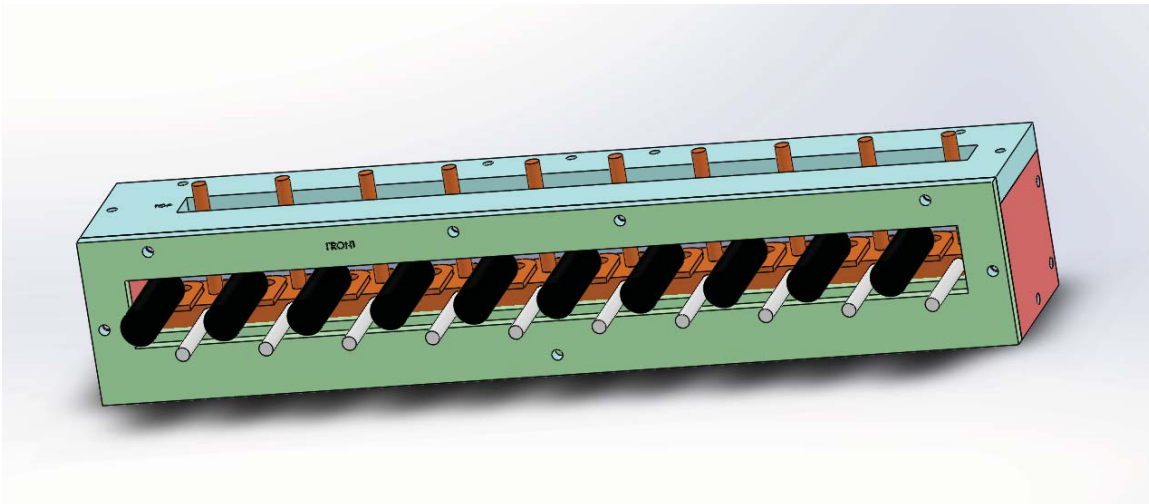


Figure 2.28: Top: CAD model of the water and electrical hookups for the bottom bucket coils. Bottom: Photo of the connections under the main chamber.

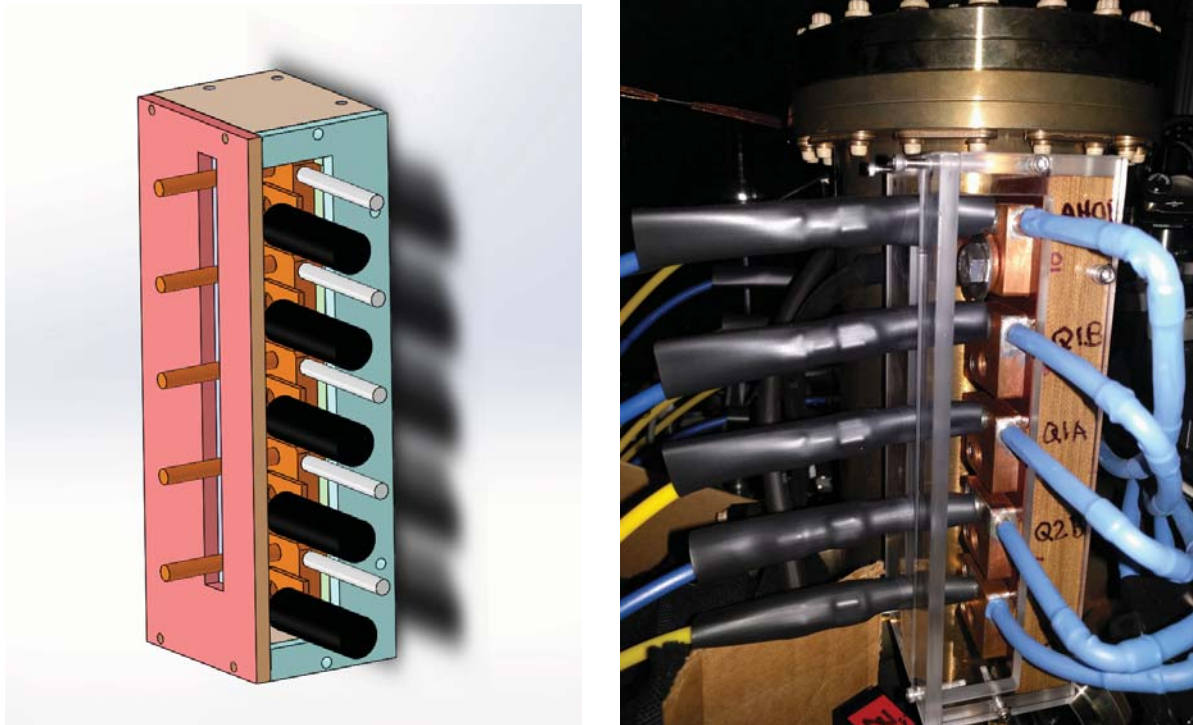


Figure 2.29: Left: CAD model of the water and electrical hookups for the top bucket coils. Right: Photo of the connections on the mounting tabs on main chamber.

with some static electricity touched the optical table and got shocked. It is rather difficult to get analog comparators to work when the lab ground sometimes swings by 10 V (as measured with an oscilloscope when delivering a shock to the lab ground... yes I kid you not). Of course it should have been possible to get this to work, but it would have been quite an ordeal. In the interest of time, we opted for the proven Keithley solution. In retrospect, if one is trying to make homemade electronics, it may be better to sense temperatures using a larger signal from thermistors, rather than spending great effort trying to shield and filter the tiny voltages from thermocouples. Keithley's off-the-shelf product does a fine job at this, however.

In addition to the thermocouples, the *return* lines of pairs of water coils are combined together so that there is a flowmeter for every two water-cooled coils, in order to detect a leak or any plumbing obstruction, as shown in Figure 2.31. We used the Proteus Industries 0804BN1 flowmeters which have an internal relay so that if any flow rate drops below a set value, the "normally open" channel shorts to ground and the signal which is attached with a pull-up resistor to logic high drops low. The quadrant coil was measured to have a nominal flow value of 1.6 L/minute and the middle anti-Helmholtz coil was measured to have a nominal flow rate of 1.25 L/m. The threshold values for tripping the interlock were adjusted in situ for the two coils going to each flowmeter. The two logic signals from the flowmeters and the Keithley are then fed through an AND gate that travels to both the power supply and through a second set of AND gates that turn off the AOMs to the high power fibers if either the interlock signal or the computer control drops low. After hearing some horror stories, we were sure to make it so that logic *high* means that things are ok, and we also added appropriate pulldown resistors, so that if anything is accidentally turned off or unplugged, the interlock will shut things off.

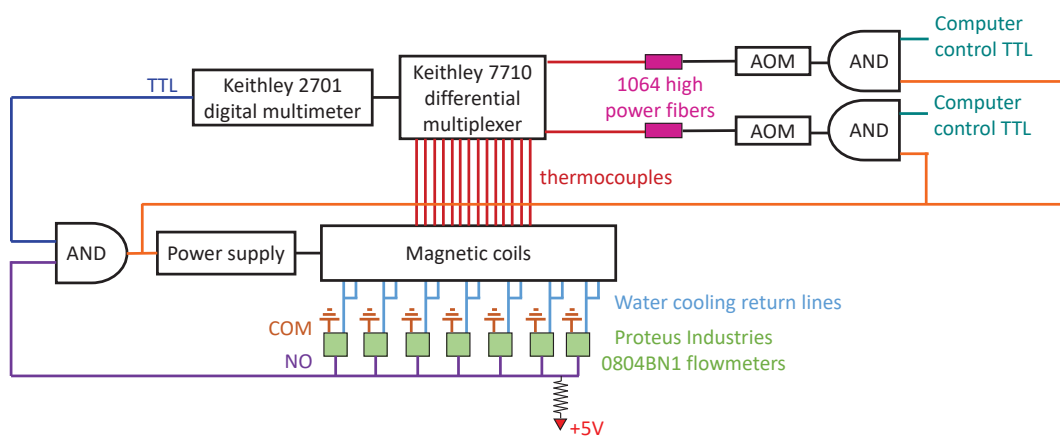


Figure 2.30: Schematic of safety interlock for both the magnetic coils and the 1064 high power fibers.

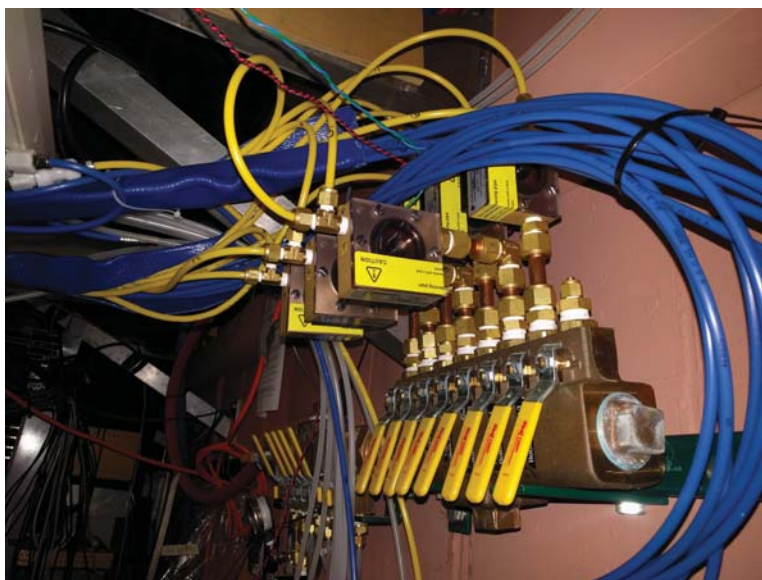


Figure 2.31: Photo of part of the water cooling manifold, with flowmeters shown.

| Beam | Transition | λ (nm) | Γ | I_{sat} | ω_0 | Typical power range |
|--------------------|--|----------------|----------|---------------------------|---|---------------------------|
| Blue MOT | $^1S_0 - ^1P_1$ | 461 | 30 MHz | 40 mW/cm ² | 2 cm | 30 mW total |
| Repump | $^3P_0 - ^3S_1$ | 679 | 1.4 MHz | 0.58 mW/cm ² | 1 cm | 5 mW total |
| Repump | $^1S_0 - ^1P_1$ | 707 | 7.3 MHz | 2.7 mW/cm ² | 1 cm | 5 mW total |
| Red MOT trapping | $^1S_0(J = 9/2) - ^3P_1(J = 11/2)$ | 689 | 7.4 kHz | 3 μ W/cm ² | 1 cm | 1 mW to < 1 μ W total |
| Red MOT stirring | $^1S_0(J = 9/2) - ^3P_1(J = 9/2)$ | 689 | 7.4 kHz | 3 μ W/cm ² | 1 cm | 1 mW to < 1 μ W total |
| Optical pumping | $^1S_0(J = 9/2) - ^3P_1(J = 9/2)$ | 689 | 7.4 kHz | 3 μ W/cm ² | 1 cm | 100 μ W |
| HODT | Far red-detuned $\alpha_{1064} = -1.3 \text{ Hz}/(\text{mW}/\mu\text{m}^2)$ | 1064 | - | - | $\omega_{0,x} = 340 \mu\text{m}$ $\omega_{0,z} = 17 \mu\text{m}$ | 10 W to 200 mW |
| VODT | Far red-detuned $\alpha_{1064} = -1.3 \text{ Hz}/(\text{mW}/\mu\text{m}^2)$ | 1064 | - | - | 25 μm $\omega_{0,z} = 17 \mu\text{m}$ | 2 W to 100 mW |
| Horizontal Lattice | Far red-detuned $\alpha_{813} = -1.1 \text{ Hz}/(\text{mW}/\mu\text{m}^2)$ | 813 | - | - | $\omega_{0,x} = 120 \mu\text{m}$ $\omega_{0,z} = 35 \mu\text{m}$ | 1 W each axis |
| Vertical Lattice | Far red-detuned $\alpha_{813} = -1.1 \text{ Hz}/(\text{mW}/\mu\text{m}^2)$ | 813 | - | - | 90 μm | 1 W |
| Clock laser | $^1S_0 - ^3P_1$ | 698 | 1 mHz | 0.4 pW/cm ² | 0.36 mm | 10 mW |

Table 2.1: Specifications for important lasers used in the experiment.

2.4 Laser systems

2.4.1 Optics layout around the main experiment

The laser beams required by our experiment are: blue Zeeman slower, blue 2D MOTs, blue 3D MOTs, two blue MOT repumps, red MOT trapping laser, red MOT stirring laser, vertical and horizontal optical dipole traps (ODTs), blue absorption imaging (horizontal, vertical high-resolution, vertical low-resolution), red absorption imaging, optical pumping, 3 lattice beams to form a 3D lattice, horizontal and oblique clock lasers, and a blue probe for PMT fluorescence detection during clock readout. We eliminated the need for the blue probe and enhanced our signal-to-noise by re-trapping the atoms in the blue MOT for clock readout, leaving only 20 more beams to figure out how to arrange around our experiment (see Figure 2.35)! The specifications for each of these beams are summarized in Table 2.1.

The optics layout for the mezzanine which surrounds the vacuum chamber is shown in Figure 2.32. It was helpful to import the Solidworks drawing into Adobe Illustrator and make the whole to-scale schematic beforehand, as it is easier to drag images around the screen than to realize something won't fit and then re-do half of the optics. We were able to save some space by putting high-resolution blue absorption imaging, red absorption imaging, and optical pumping beams all along the same path. We also added a low-resolution blue absorption imaging beam path with a larger field-of-view to aid in alignment.

The layout underneath the vacuum chamber on the main optical table is shown in Figure 2.33. To save space, we combined all red-colored beams (both blue MOT repumps and both red MOT lasers) on this level, and then launched the 4 combined beams up to the mezzanine with a periscope. The red MOT, blue MOT, high resolution absorption imaging, and vertical lattice beams are all launched from the bottom and combined with polarizers and dichroics as shown in Figure 2.33. They arrive on the top mezzanine breadboard, shown in Figure 2.34. After passing through the high-resolution imaging objective, the vertical MOT beams must be re-focused before they are retro-reflected. The high-resolution absorption imaging beam has the opposite helicity as

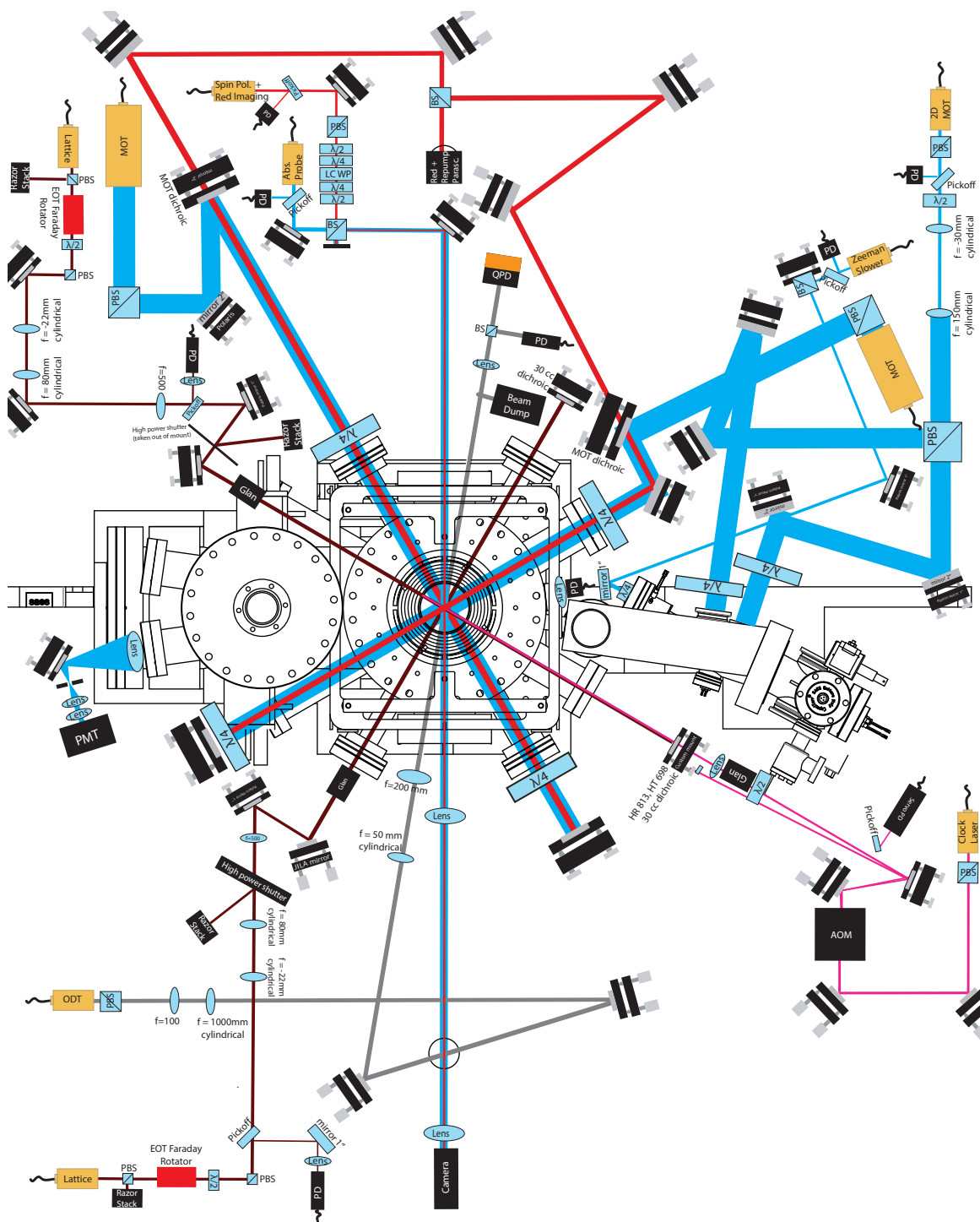


Figure 2.32: A to-scale drawing showing the layout of the optics on the mezzanine breadboard that surrounds the chamber.

the MOT beams and so it is separated via a PBS so it can then be imaged on the Andor camera. The low-resolution vertical absorption imaging beam travels at a slight angle to miss the other beam paths and is imaged on a cheaper Allied Vision Guppy camera. Additionally, the vertical ODT beam (VODT) and the oblique clock laser are launched from the top.

2.4.2 Blue system upgrades

As shown in Figure 2.36, we made some minor changes to our blue laser system in order to meet the specifications required by the commercial AOSense source. The master laser is a commercial external-cavity diode laser (ECDL) at 461 nm. We originally used a New Focus Vortex laser, which was the first available of its kind. The power output degraded over time (possibly to be expected with any blue diode), and also the laser controller seemed to have some noise and grounding issues, so we had to add a buffer and a low-pass filter between the controller and the servo that actuates on the PZT to stabilize the laser frequency to the atomic transition. We realized that much of our shot-to-shot atom number fluctuations from absorption imaging could actually be attributed to frequency noise on the blue master diode laser due to noise and grounding issues involved with the laser controller and the lock. In particular, though the servo has a high output-impedance, high frequency noise on the laser controller external PZT control input leaked backwards through the whole servo circuit, as the high output-impedance only applies for signals within the bandwidth of the circuit. In addition to this high-frequency noise, we also saw 60 Hz noise, and we struggled to find a grounding configuration that would minimize this. Eventually, we upgraded to a new blue master laser and controller from AOSense, which so far has not had any of the aforementioned noise and grounding problems.

The light from the blue master (≈ 30 mW output) is then appropriately frequency-shifted, then travels to 3 injection-locked slave lasers. The light from the 2D MOT slave is split equally between both of the 2D MOTs in the AOSense system. Previously we had used a high-frequency AOM from Brimrose for the Zeeman slower, with a quoted 40% efficiency. However, we realized that we could get up to twice as much power double-passing a 90% efficiency AOM. A 3-way fiber

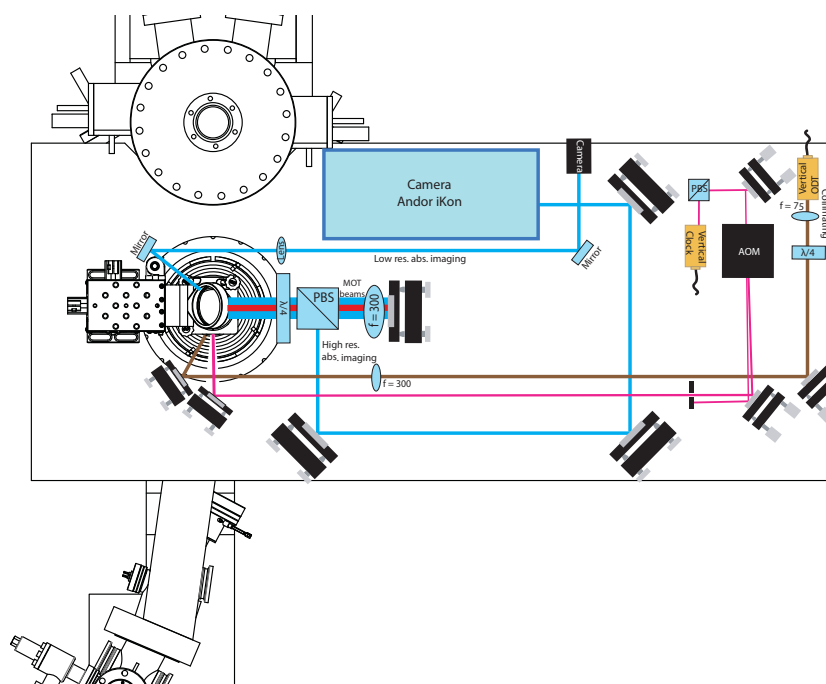


Figure 2.34: A to-scale drawing showing the layout of the optics on the optical table below the chamber.

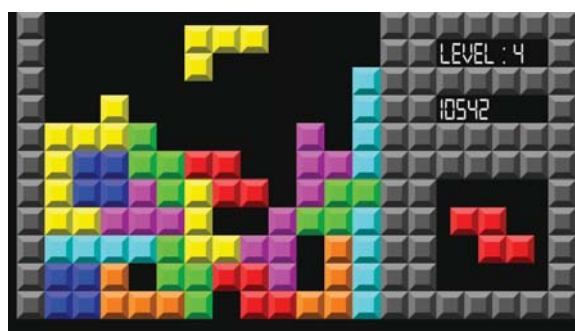


Figure 2.35: Artist's depiction of the optics layout process.

splitter carries the light to the 3 arms of the final blue MOT.

| Device | $1/e^2$ beam dimensions | Number of input beams | Detuning | Power | Polarization |
|--------------------|--|-----------------------|----------|---------------|-------------------------------|
| Slower | Round d = 5 mm Slight focusing into oven | 1 | -500 MHz | > 25 mW | circular |
| Transverse cooling | Round d = 4 mm | 1 | -40 MHz | > 5 mW | Linear along atomic beam axis |
| 2D MOTs | 5 mm x 25 mm | 1 for each trap | -40 MHz | > 25 mW total | circular |

Table 2.2: List of power, shape, and polarization requirements for the new AOSense strontium source.

2.5 Imaging system

A high-resolution imaging system helps us to characterize our atom cloud, eliminating some of the guesswork and indirect measurements in previous work. Combining the energy resolution of clock spectroscopy with the spatial resolution of a relatively high numerical aperture (NA) imaging system will both provide new tools for quantum simulation as well as the capability to diagnose spatially-dependent inhomogeneous broadening due to systematic shifts. As this system was built with both next-generation clocks and quantum simulation in mind, we decided to make the horizontal lattice beams parallel to the ground and make the vertical lattice beams parallel to gravity. Whereas tunneling is generally not desirable during clock operation, we still wanted to allow for tunneling for experiments that could investigate synthetic gauge fields [39, 151, 172, 15, 106] and simulate charge currents [104, 6]. Therefore, as the interesting physics in the lattice would occur along 2D sheets in the xy plane, we wanted the high-resolution imaging path to run parallel to the vertical lattice beam, as well as the vertical MOT beams.

The simplest design was to retroreflect the vertical lattice off of the first optical surface of the imaging system and pass both the red and blue MOT beams through the entire imaging system. A

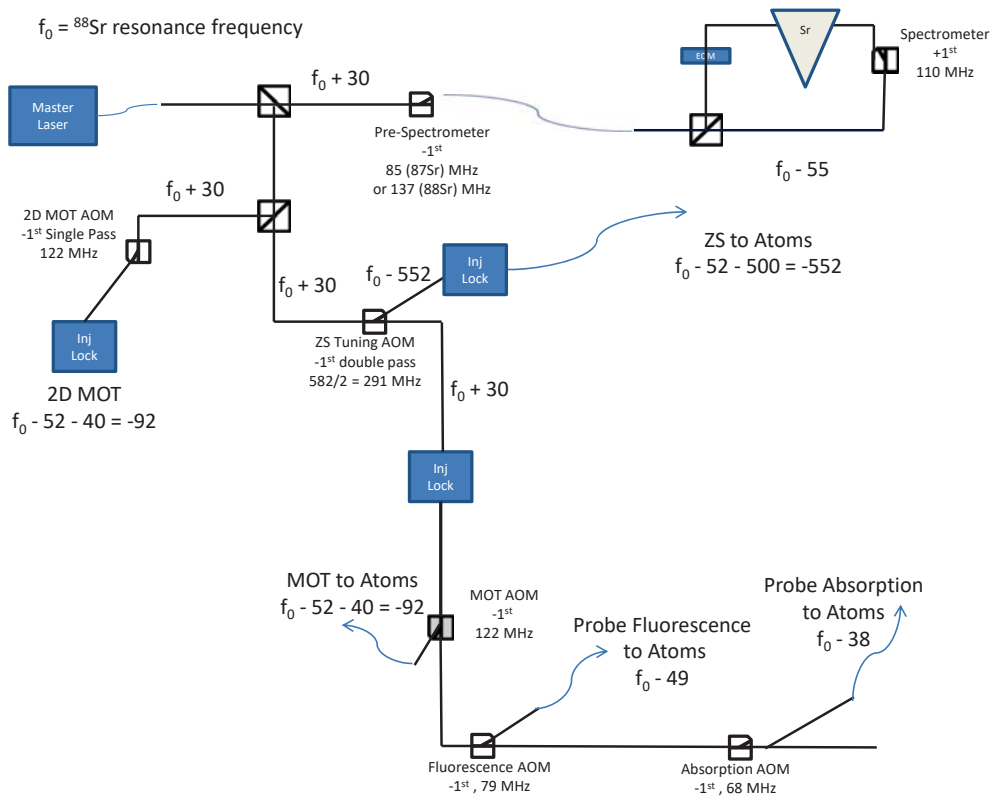


Figure 2.36: Schematic showing updates to the blue system that were made in order to satisfy the specifications required by the AOSense system. All frequency values are shown in units of MHz.

polarizing beam splitter (PBS) that works at both 461 and 489 nm then separates the MOT beams from the absorption imaging beam (these travel through the atom cloud with opposite helicities) so that the MOT beams can be re-collimated and retroreflected, while the imaging beam is sent to the CCD camera, as shown in Figure 2.34. The effective focal length f of the imaging system is approximately equal to the distance from the objective to the atoms. We wanted to use ≤ 50 mm optics ≈ 250 mm away from the objective to re-collimate and retroreflect the MOT beams. For an initial blue MOT beam diameter of 20 mm, this therefore requires that

$$\frac{(20\text{mm}) \cdot (250\text{mm})}{f} \leq 50\text{mm}, \quad (2.4)$$

so $f \geq 100$ mm. This therefore constrains the first lens to be ≈ 90 mm away from the atoms. A section view showing the imaging system's location in the main experiment is shown in Figure 2.37.

We also had to allow room for the vertical optical dipole trap (VODT), as we were planning to evaporate to quantum degeneracy in a crossed optical dipole trap (XODT) configuration. Since during the design phase we were unsure of our evaporation protocol and wished to maintain flexibility to refine this detail of our experiment, we allowed room for the VODT to pass at an oblique angle outside of the imaging objective. This also allowed room for an oblique clock laser for 3D band detection and manipulation, as well as a low-resolution vertical imaging beam path which, due to its larger field of view (FOV) is a convenient tool for alignment. Given those constraints, the maximum NA we can attain is 0.23.

2.5.1 Design

So how do you design a high-resolution microscope?² Because of the diffraction limit, you generally want to capture as much of the solid angle from the source as possible (given the geometric constraints of your system). This is characterized by the numerical aperture $\text{NA} = n \sin \theta$, where n is the index of refraction of the material surrounding the lens (air in our case), and θ is the half-angle of the cone of light traveling to the lens.

² Many groups seem to work with optics companies to do this. Our postdoc Ed Marti was chiefly responsible for this. This section aims to summarize and de-mystify the design process, as Ed was right that it's not too bad to just do it yourself!

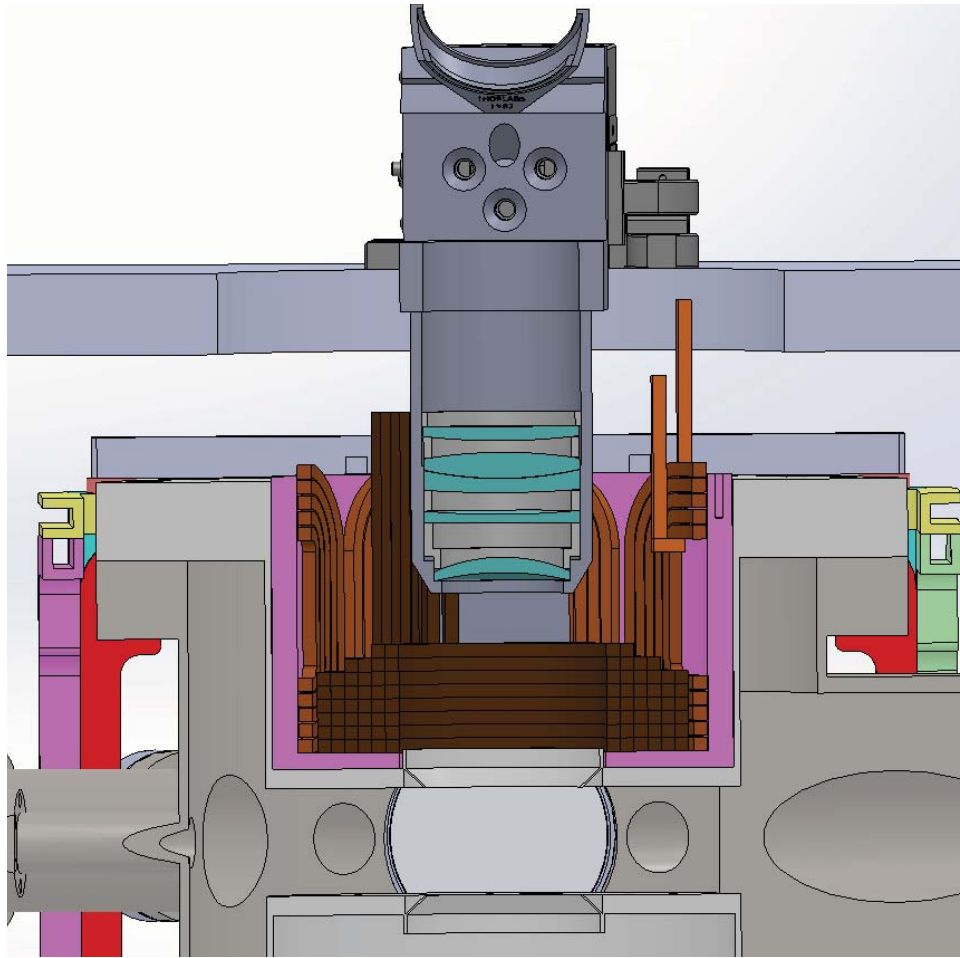


Figure 2.37: Section view of the high-resolution imaging system, in its position inside the top bucket window.

However, the diffraction limit is not the only thing that can limit microscope performance. The preceding discussion relied on the paraxial approximation, which assumes that a small angle of incidence between the all rays of light and the normal to the surface. So, whereas Snell's law describes refraction of a ray of light as it travels from a medium with index of refraction n_1 at an angle θ_1 to the surface normal, to a medium with index of refraction n_2 at an angle θ_2 to the surface normal according to $n_1 \sin \theta_1 = n_2 \sin \theta_2$. In the paraxial approximation where $\theta_{1,2} \approx 0$, this just becomes $n_1 \theta_1 = n_2 \theta_2$. The Taylor series expansion for $\sin \theta$ is,

$$\sin \theta = \theta - \frac{\theta^3}{3!} + \frac{\theta^5}{5!} - \frac{\theta^7}{7!} + \dots \quad (2.5)$$

So in other words, the paraxial approximation amounts to just taking the first term in this expansion. According to paraxial theory, all rays focus at the same point in space, with a spot size determined by Gaussian beam propagation. When the assumption that $\sin \theta \approx \theta$ begins to break down, this is no longer the case, leading to image distortion referred to as aberration. Spherical aberration refers to the way that different rays focus at different points in space, as shown in Figure 2.38 [41].

The first step in designing a new imaging system is to pick the first lens (closest to the object), which will set the NA of the system and thus the diffraction-limited resolution. In order to ensure that our imaging system is diffraction limited, we must take care to minimize aberrations. One option is an asphere where the lens surface is designed so that, to a certain polynomial order, all rays are incident at the same angle. Whereas small aspheres can be molded, custom-grinding a larger asphere is a bit too costly and difficult for our application (though it is done for telescopes, etc). A second option is an achromatic doublet, which combines two spherical lenses: a positive focal length lens made from low-index glass with a negative focal length lens made from high-index glass so that the θ^3 spherical aberrations cancel but the focusing powers do not [41]. This also has the effect of mitigating chromatic aberrations (hence the name).

Importantly, aberration cancellation must be done with particular angles of incidence and

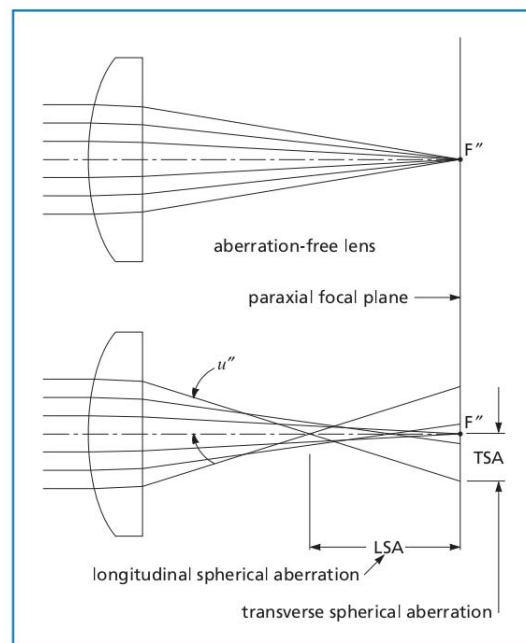


Figure 2.38: Illustration of aberrations from a plano-convex lens. Image from [41].

refraction in mind. In other words, aspheres and achromatic doublets only minimize aberrations for a particular magnification (also referred to as “conjugate ratio”). Commercial achromats are generally designed for an infinite conjugate ratio; that is, they are designed to collimate the light from a point source. A third option is to use a custom meniscus formed by two surfaces with different radii of curvature. Similar to an achromatic doublet, this gives us enough degrees of freedom to cancel third-order spherical aberrations.

In general, there is a bound on how short one can make the focal length before higher-order aberrations begin to dominate. Since achromats are designed for infinite conjugate ratio, they only minimize spherical aberrations when placed a focal length away from the source. Due to higher-order aberrations, they typically only work well for $NA \leq 0.1$. A custom meniscus has the advantage of being easier to manufacture than an asphere, and it also can achieve a higher NA, because we can design it to minimize aberrations for the conjugate ratio of our choosing. A custom meniscus can therefore achieve a higher NA than a commercial achromat, as it need not collimate the image in order to effectively minimize spherical aberrations, and so it can be placed closer to the image. We therefore choose a custom meniscus for the first lens of our system.

The four-lens imaging system is shown in Figure 2.40. Our design process began with the constraint of a 90 mm radius of curvature for the first surface of the meniscus, which is coated with the AR coating shown in Figure 2.39 to serve the dual purpose of retroreflecting the vertical lattice. The radius of curvature of the second surface was then chosen to minimize aberrations. The first lens brings the image location farther away so that a commercial achromat is then able to collimate it. One can try several different options for this achromat and then go back and modify the meniscus so that the combined two lens system minimizes aberrations. If this combination does not allow enough degrees of freedom to satisfactorily cancel aberrations, one can add a third lens between the two, such as the chosen plano-concave lens shown in Figure 2.40. Finally, a plano-convex lens is used as the last piece of the objective, and it focuses the collimated beam onto the CCD camera.

Sudden switching of the magnetic field coils can induce Eddy currents that could potentially

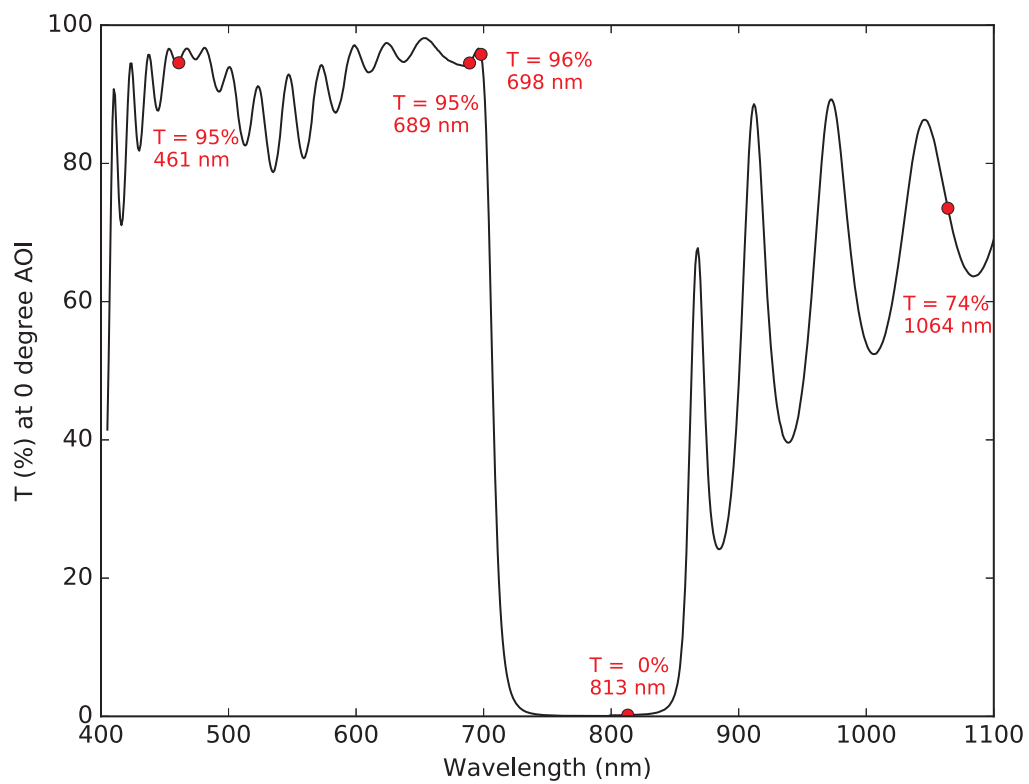


Figure 2.39: Coating curve for the meniscus, which transmits the 461 and 689 nm MOT beams and retroreflects the 813 nm lattice.

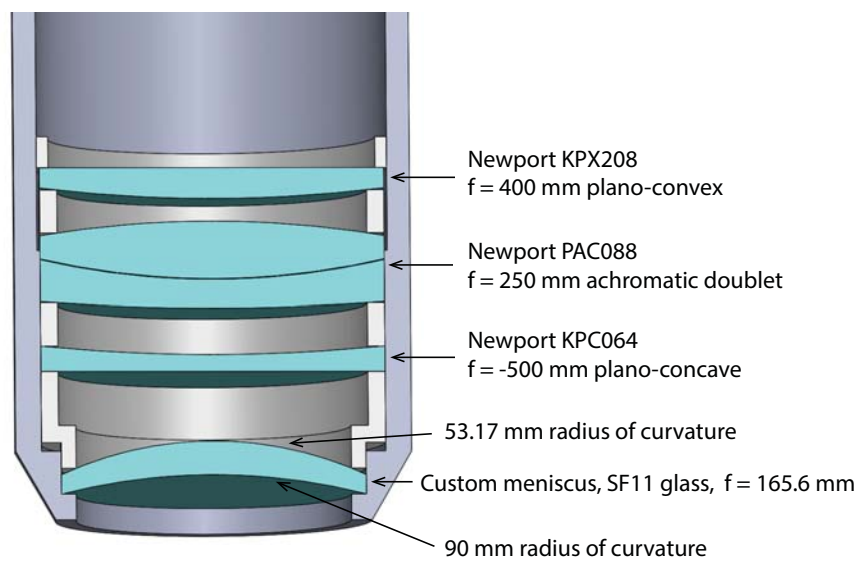


Figure 2.40: Section view of the high-resolution imaging system design, showing all part numbers and specifications.

shake the optical system. We avoid this by using a plastic (Delrin) lens holder and spacers. The only metal in the mount is a SM2RR Thorlabs retaining ring, which can be replaced with a plastic part as well.

2.5.2 Measuring and testing resolution

One way to test imaging system resolution is to image a pinhole. For our test pattern, we image two 350 nm pinholes,³ as shown in Figure 2.41. The Airy disk describes the diffraction-limited pattern formed by focusing a point source with a perfect lens with a spherical aperture, and the angular intensity I is given by,

$$I(\theta) = I_0 \left(\frac{2J_1(ka \sin \theta)}{ka \sin \theta} \right)^2, \quad (2.6)$$

where θ is the angle of observation, $k = 2\pi/\lambda$ is the wavenumber of the light from the point source, a is the radius of the aperture, and J_1 is the order-one Bessel function of the first kind. Figure 2.42 plots an azimuthal average of a 2D fit of the Airy function to the data.

There are many ways to define imaging system resolution. The Rayleigh criterion states that the minimum resolvable distance between two point sources occurs when the first diffraction minimum of one source overlaps with the maximum of the other. Theoretically, the minimum resolvable radius from an Airy disk r_{Airy} is,

$$r_{\text{Airy}} = 0.5 \cdot \frac{1.22\lambda}{\text{NA}} = 1.2\mu\text{m} \quad (2.7)$$

It is generally difficult to get data where the wings match well with the theoretical fit function. The fit in Figure 2.42 shows a first diffraction minimum at $1.5\mu\text{m}$, while the data itself shows a kink at $1.2\mu\text{m}$.

Another option is to use the $1/e^2$ radius of the fit,

$$\omega_{\text{Gaussian}} = 0.68r_{\text{Airy}} = 0.41 \frac{\lambda}{\text{NA}} = 0.82\mu\text{m}, \quad (2.8)$$

³ Made by and borrowed from the Kapteyn-Murnane group. Thank you!

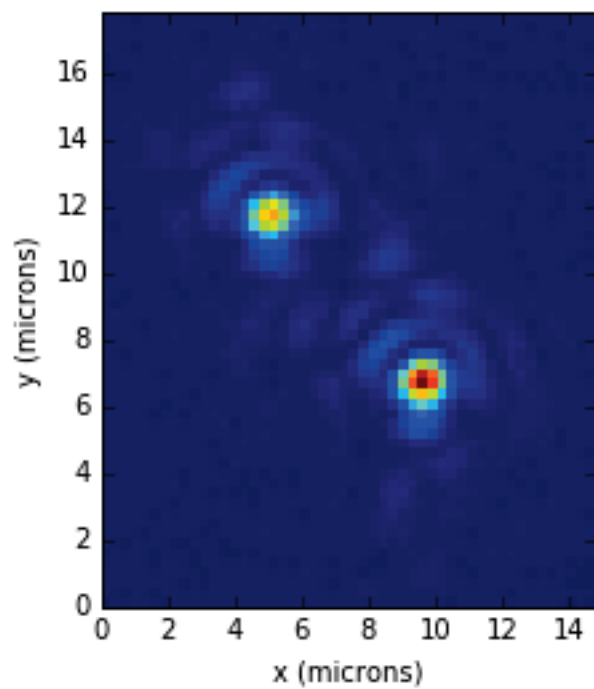


Figure 2.41: Image of two 350 nm pinholes taken with our lens system in order to test the resolution.

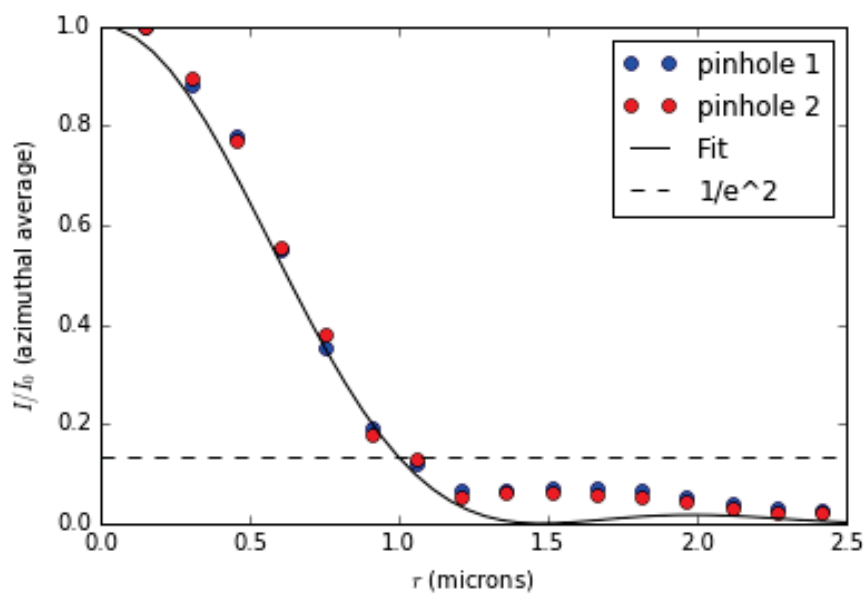


Figure 2.42:

which isn't too far off from the measured $1.0\mu\text{m}$. This corresponds to a depth of focus z_{Rayleigh} of

$$z_{\text{Rayleigh}} = \frac{\pi\omega_0^2}{\lambda} = 0.53 \frac{\lambda}{\text{NA}^2} = 4.6\mu\text{m} \quad (2.9)$$

and a field of view of $150\mu\text{m}$.

Chapter 3

Preparation

The strontium gas leaves a hot effusive oven at a temperature of 500°C and then undergoes a series of laser cooling and trapping stages to realize the goal of a degenerate Fermi gas in the ground band of a 3D optical lattice. In this section we summarize the steps necessary to bridge over 10 orders of magnitude in temperature in order to finally realize complete control over all internal and external degrees of freedom for atoms confined in a 3D lattice. All of the experiments described in this thesis use the fermionic ^{87}Sr isotope, which is the preferred choice for clock operation, and also has a large nuclear spin of $I = 9/2$, which is both advantageous for evaporative cooling and provides a sizable basis in a spin synthetic dimension which can be used for quantum simulation experiments.

3.1 Initial laser cooling stages

A simplified level diagram for strontium is shown in Figure 3.1. The first stages of laser cooling occur on the 32 MHz linewidth $^1S_0 - ^1P_1$ transition at 461 nm ("blue transition"). We use a commercial source from the company AOSense, which includes a Zeeman slower and two 2D MOTs, which slow the atoms and direct them into the main chamber. We just input the specified beam powers, shapes, and polarizations (see Table 2.2), and Tom Loftus produces a magical cold strontium beam. Then, once in the main chamber, the atoms are trapped in the "blue MOT" on this transition, with a magnetic field gradient of 30 G/cm. Up to 10^7 atoms are trapped in our blue MOT, at an optical density high enough that the atoms actually cast a shadow on the vertical

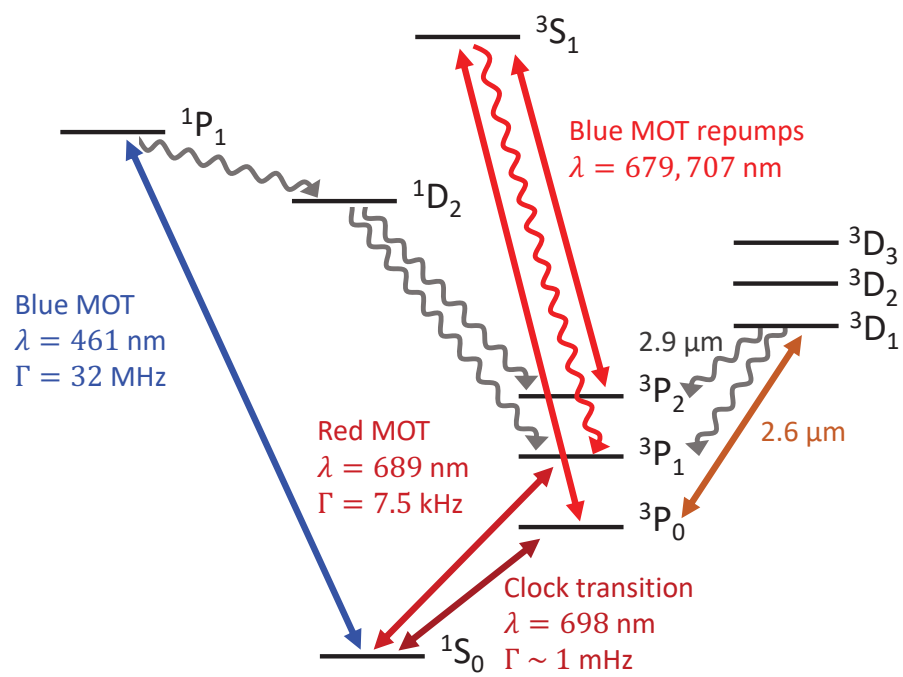


Figure 3.1: Level diagram of relevant states and transitions in ^{87}Sr .

MOT beam (and so sometimes MOT performance is enhanced by some slight misalignment of the retroreflection so that the shadow avoids the atoms).

The blue transition is mostly-closed, with some leakage to the 1D_2 state, which can then decay to the metastable 3P_2 state. Therefore, operation of the blue MOT benefits from repumping via the 707 nm $^3P_2 - ^3S_1$ state, which can decay to the 3P_0 clock state, thus requiring another repump to address the 679 nm $^3P_0 - ^3S_1$ transition. Note that this is not the only repumping option; other groups repump via the 497 nm 3P_2 to 3D_2 transition[149]. The repumps are free-running ECDLs (i.e. their wavelengths are not externally-referenced), and are modulated over a ≈ 3 GHz range by modulating their PZTs at a frequency of ≈ 1 kHz in order to address all the hyperfine levels of the $I = 9/2$ ^{87}Sr atom. In the absence of these repumps, atoms accumulate in the magnetically-trappable 3P_2 state and are trapped by the MOT fields [166]. Atoms in the magnetic trap do not suffer the same loss due to light-assisted collisions as atoms in MOT, and so measuring the lifetime of atoms in the magnetic trap offers a first lower-bound on the vacuum-limited lifetime. To measure the lifetime, first the MOT is operated without repumps, then all lasers are shut off while atoms are held in the magnetic trap, then after some hold time, the repumps and MOT beams are switched on to re-capture atoms in the MOT where they can be counted via side absorption imaging, as shown in Figure 3.2. Here, the lifetime is limited by blackbody radiation (BBR) driving the $2.9 \mu\text{m}$ $^3P_2 - ^3D_1$ transition, which can decay to both the non-magnetically trappable 3P_0 and (via decay through the 3P_1 state) 1S_0 states. The measurement in Figure 3.2 is consistent with an ≈ 40 s lifetime estimated from the intensity of room temperature BBR, and was thus the first confirmation that our vacuum-limited lifetime was greater than 40 s.

After the atoms have been cooled to 2-3 mK on the blue transition, they are then loaded into the second-stage "red MOT" which operates on the 7.4 kHz $^1S_0 - ^3P_1$ intercombination transition at 689 nm. Nice descriptions of this so-called "narrow-line MOT" are given in Refs. [110] and [9], so we just provide a quick summary here. One typically thinks of the Doppler limit to laser cooling T_{Doppler} on a transition of linewidth Γ as being the ultimate limit of MOT temperature, where $T_{\text{Doppler}} = h\Gamma/2k_{\text{B}}$ results from competition between the rates of cooling forces and spontaneous

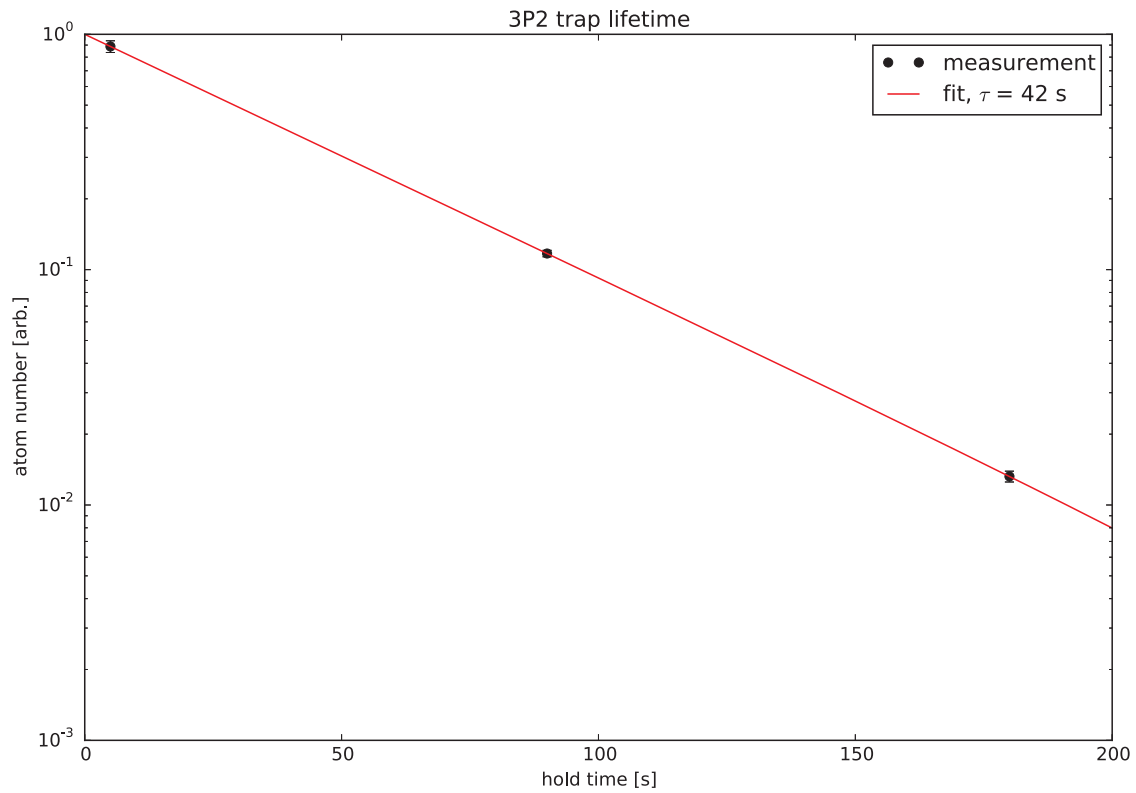


Figure 3.2: Lifetime of the 3P_2 atoms in the magnetic trap, limited by blackbody radiation photons that drive transitions which then decay to states that are not magnetically-trappable.

emission. However, because the intercombination transition has such a small Doppler limit of ≈ 180 nK, one must also consider the recoil temperature $T_{\text{recoil}} \approx 230$ nK, when the transition is so narrow that a single momentum kick from spontaneous emission of a cooling photon can Doppler-shift the atom out of resonance with the cooling laser. The theoretical limit on laser cooling due to this effect is $T_{\text{recoil}}/2$, and so narrow-line MOT dynamics are complicated by the interplay of Doppler and recoil effects, which are of similar order. Trapping and cooling forces come from our trapping laser “ α ” which drives the $^1S_0, F = 9/2 - ^3P_1, F = 11/2$ transition.

However, as the ground state only has nuclear spin, whereas the excited state has electron spin, the ground and excited states have very different g -factors. Because of this, the “less-stretched” states (with smaller $|m_F|$) are too far detuned (and sometimes detuned so they can absorb a photon from the wrong MOT beam), and so experience insufficient cooling forces. Luckily, these transitions also have the smallest line strengths, and so by using a second “stirring” laser “ β ” on the $^1S_0, F = 9/2 - ^3P_1, F = 9/2$ transition, we can quickly pump atoms back towards the stretched states, and thus achieve the desired trapping and cooling forces on average.

A timing diagram showing the red MOT loading, red MOT, and ODT loading is shown in figure 3.3. To span the temperature difference from the ≈ 2 mK blue MOT to the ≈ 1 μ K red MOT, the red MOT lasers are first operated at a higher intensity and frequency-modulated to maximally address all velocity classes from the blue MOT. Then, as shown in Figure 3.3, the frequency modulation envelope is ramped down until the red MOT is operated at a single frequency, while simultaneously the intensity is ramped down by a factor of 100. Note that midway through the broadband ramp, we switch the transimpedance gain for the in-loop photodiodes so that we may effectively servo the light intensity over 3 orders of magnitude.

3.2 Crossed optical dipole trap

3.2.1 Initial loading

For evaporative cooling, the atoms are next loaded into a 1064 nm crossed optical dipole trap (XODT), which is formed by a horizontal and a vertical beam crossing at their respective waists. The XODT is held on throughout both the broadband and narrow-line cooling stages in the second-stage MOT. To ensure that narrow-line cooling works efficiently inside the XODT, the spatially-dependent differential ac Stark shifts of the $^1S_0 - ^3P_1$ cooling transition must be minimized. The horizontal beam has a sheetlike geometry with waists of 340 μm and 17 μm in the horizontal and vertical directions, respectively. By focusing more tightly in the vertical direction, the horizontal beam achieves the same confinement against gravity for a lower light intensity. The vertical beam, which is aligned at a small angle with respect to gravity, is a circular Gaussian beam with a 25 μm beam waist. The HODT and VODT have initial powers of ≈ 10 W and ≈ 2 W, respectively. During XODT loading, the quadrupole magnetic field from the red MOT has cylindrical symmetry about the vertical axis, and so the following polarizations are listed with respect to a vertical quantization axis. Similar to [149], the vertical beam is circularly polarized to minimize differential ac Stark shifts. We perform a further stage of cooling by blue-detuning the cooling light relative to the free space resonance to address atoms inside the XODT. After the red MOT is switched off, 5×10^6 atoms at 1.5 μK are loaded into the XODT, in an equal mixture of all 10 nuclear spin states.

3.2.2 Theory

To calculate the vertical trap potential $U(z)$, we must include the effects of gravity, and find,

$$U(z) = -\frac{1}{2}\alpha\bar{E}^2 e^{-2z^2/\omega_{0z}^2} + mgz, \quad (3.1)$$

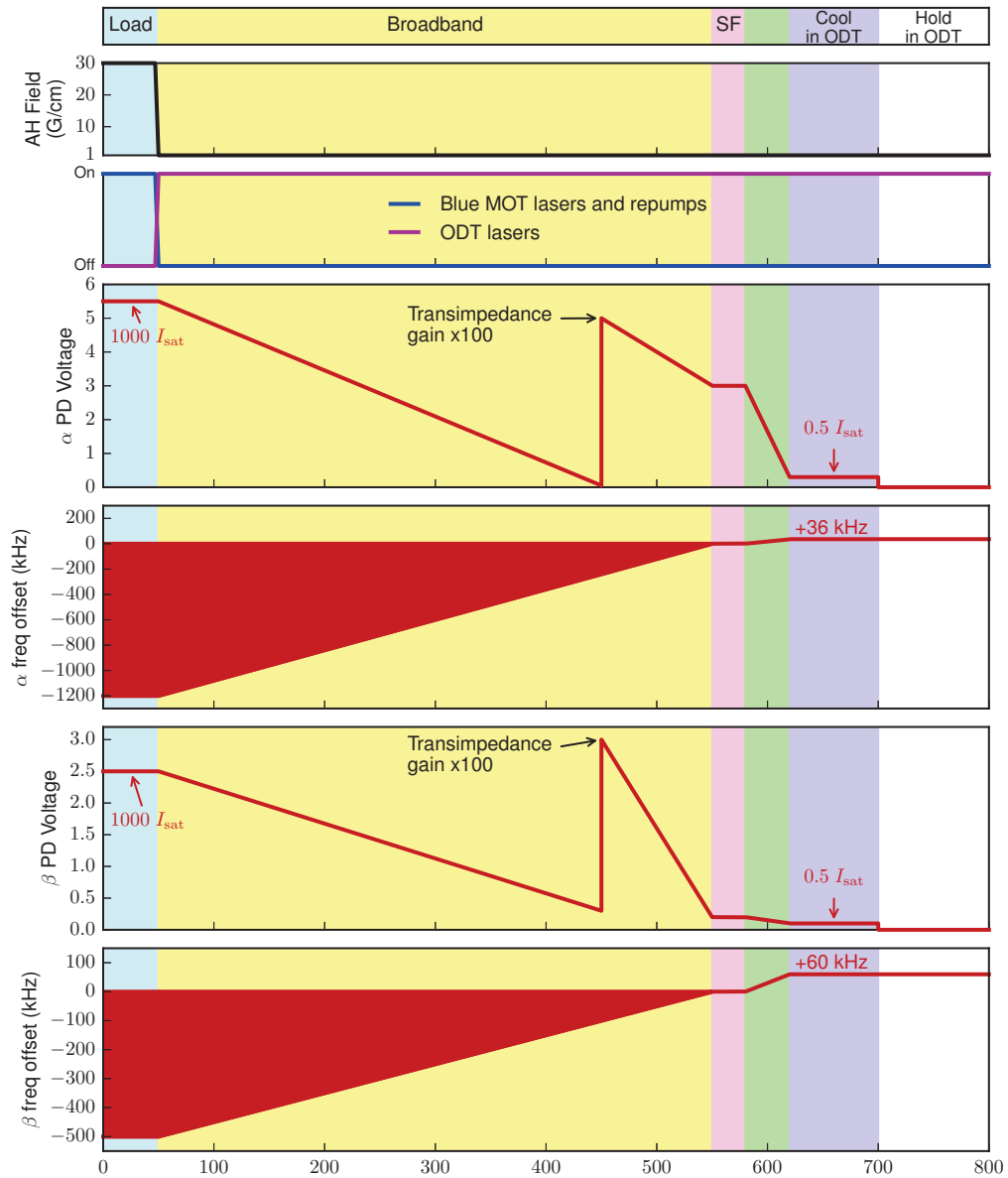


Figure 3.3: Timing diagram for the red MOT loading, red MOT, and ODT loading, showing the intensities and frequencies throughout the red MOT loading, broadband, single frequency and in-ODT cooling stages.

where \bar{E} is the average electric field,

$$\bar{E} = \sqrt{\frac{2P}{\pi\epsilon_0 c \omega_z \omega_x}}, \quad (3.2)$$

$\omega_{0x,z}$ are the beam waists along the x and z axes, respectively, P is the average beam power, α is the atomic polarizability which depends on the frequency of the trapping light.

The trap depth ΔU is given by the difference between the local minimum and local maximum,

$$\Delta U = U(z_{\max}) - U(z_{\min}), \quad (3.3)$$

and the vertical trap frequency ν_z is given by the curvature of the potential at the local minimum,

$$m(2\pi\nu_z)^2 = \left. \frac{d^2U(z)}{dz^2} \right|_{z=z_{\min}} \quad (3.4)$$

3.2.3 Measuring trap frequencies

With the atoms now loaded into the XODT, we still must do a few measurements before we can determine the Fermi temperature and optimize the evaporation trajectory. Here we discuss the measurement of trapping frequencies in the XODT.

Initially, it seemed like it would be convenient to measure the trapping frequency via parametric heating, a process by which intensity noise of the trapping beam at twice the trap frequency causes heating (and therefore atom loss) by exciting harmonic oscillator modes $|n\rangle \rightarrow |n+2\rangle$. The heating rate is given by $\langle \dot{E} \rangle = \Gamma \langle E \rangle$, where $\Gamma = \pi\nu_{\text{tr}}^2 S_\epsilon(2\nu_{\text{tr}})$ [137], $S_\epsilon(\nu)$ is the power spectral density of the laser intensity noise, and ν_{tr} is the trapping frequency. However, attempts to measure the trapping frequencies in this way resulted in spectra such as those in Figure 3.4. Since the temperature of the atoms was too close to the trap depth, parametric heating was influenced by trap anharmonicities and coupling of the vibrational modes along all three axes. This difficulty was further compounded by the fact that at the time of initial loading, we try and get as much power to the optical table as possible, so we are close to saturating our mixers, RF amplifiers, and AOMs, thus operating all of the intensity control electronics in a very nonlinear regime where it is difficult to modulate the intensity at a particular frequency without also introducing Fourier components at

harmonics and sub-harmonics. In retrospect, it makes sense why this should work for cold atoms in a deep optical lattice, but not for atoms in the ODT, where the temperature is generally fixed via the trap depth during the loading and evaporation process.

We had much better luck measuring trap frequencies via dipole oscillations, where, at a particular trap depth, we pulse on a second dipole trap with a slight offset from the atom cloud in order to “kick” the atoms along a particular axis, thus causing “sloshing” along that axis. Initially, this was accomplished using a second 1064 trap; now that we have our 3D optical lattice beams installed, we can conveniently flash them on one at a time. We perform 2D Gaussian fits to find the center of the atom cloud in absorption images taken at different times after the kick, resulting in measurements of the trapping frequencies like those shown in Figure 3.6.

3.3 Red absorption imaging

Red absorption imaging is performed with the same laser on the same $^1S_0, F = 9/2$ to $^3P_1, F = 9/2$ transition, along the same beam path used for blue absorption imaging. $50 \mu\text{s}$ seemed to be a good pulse duration. By scanning the frequency of the absorption imaging laser and counting the atom number as a function of frequency, we are able to measure the relative spin populations in the optical dipole trap, as shown in Figure 3.10.

3.3.1 Magnetic field cancellation and calibration

We first perform red absorption imaging to zero the background magnetic fields and calibrate the compensation coils. By measuring the frequency splitting between different nuclear spin states as shown in Figure 3.7 for different bias coil control voltage settings, we were able to both zero the magnetic field and calibrate the control voltage to field conversion factors for all three axes as shown in Figure 3.8

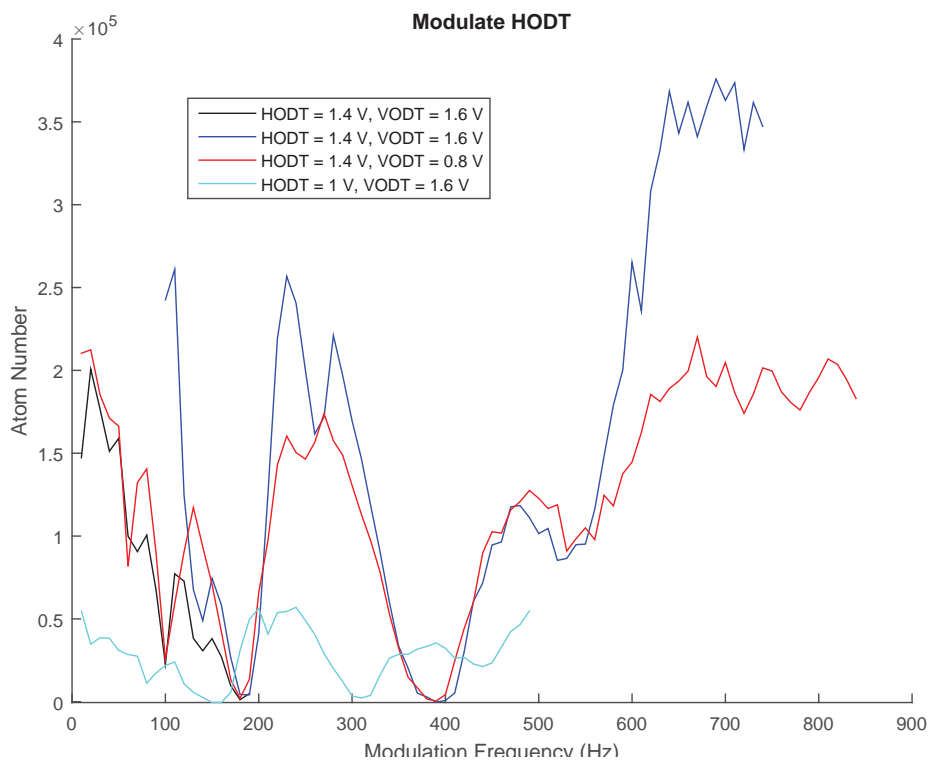
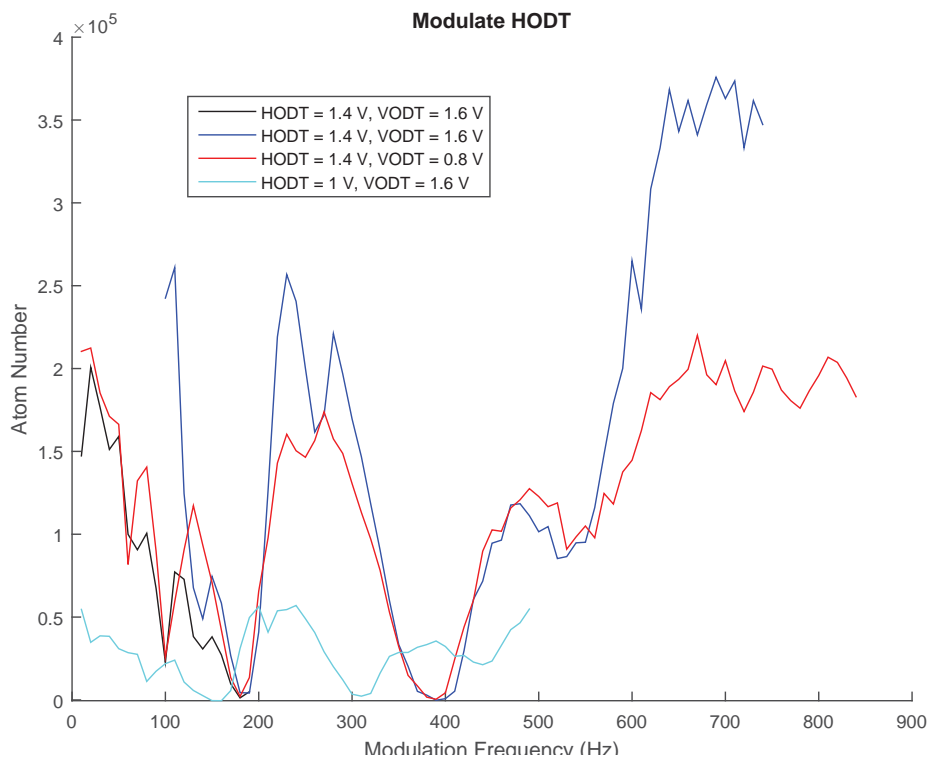


Figure 3.4: Attempt to measure XODT trap frequencies via parametric heating. I do not recommend trying to measure trap frequencies in this way. The vibrational modes along all three axes were coupled, and also some nonlinearities in the RF electronics made a confusing forest of sub-harmonics, super-harmonics, and god-knows-what.

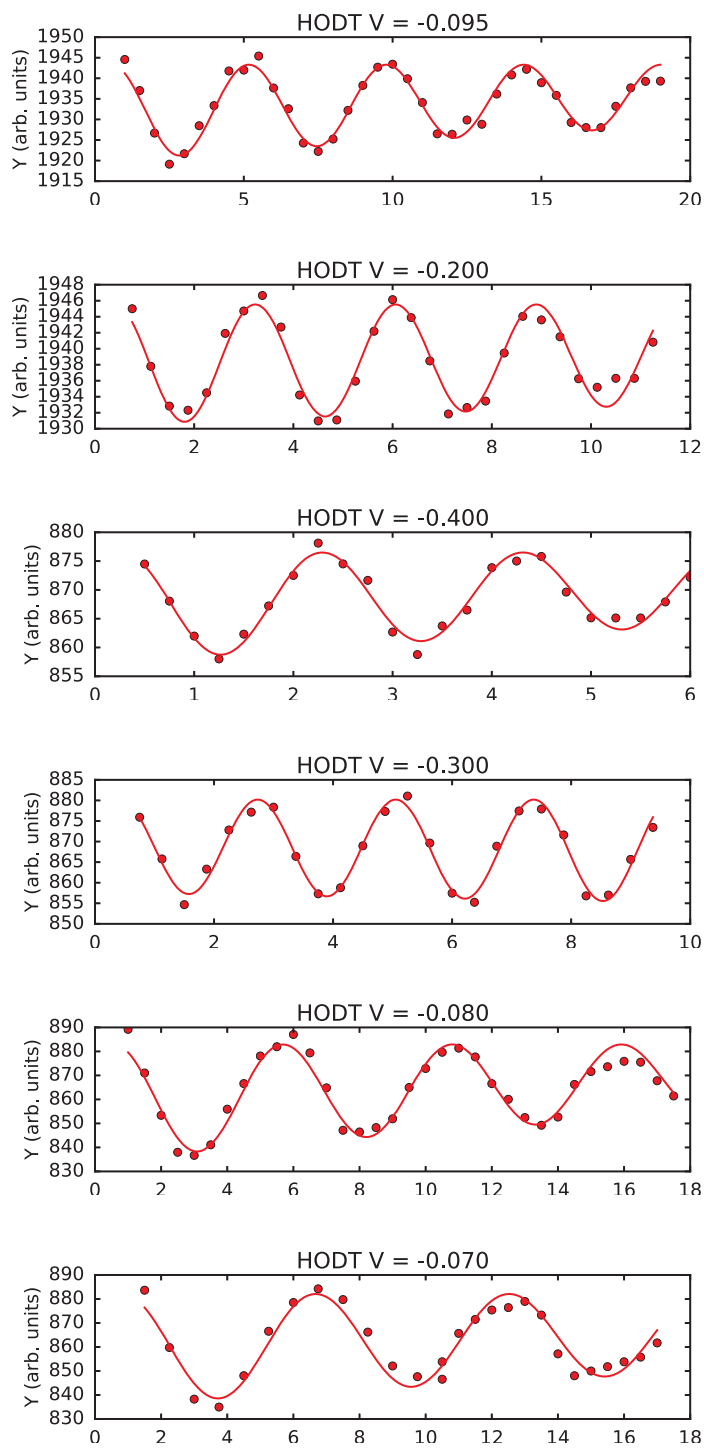


Figure 3.5: Measuring HODT trap frequencies as a function of photodiode voltage (calibration: 5W/1V) by pulsing on the the lattice beams and causing dipole oscillations.

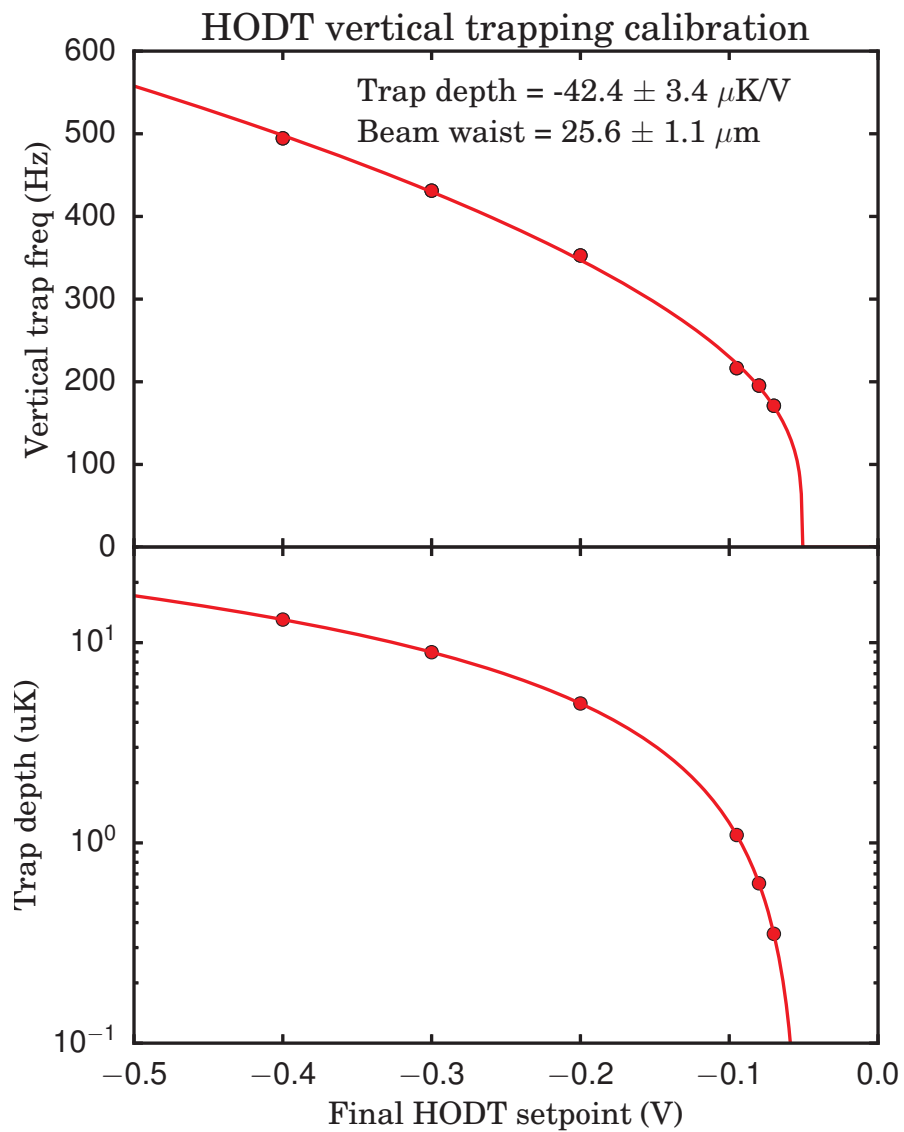


Figure 3.6: A two-parameter fit to the data shown in Fig. 3.6 determines both the voltage (calibration: 5W/1V) to trap depth conversion factor and the beam waist at the location of the atoms.

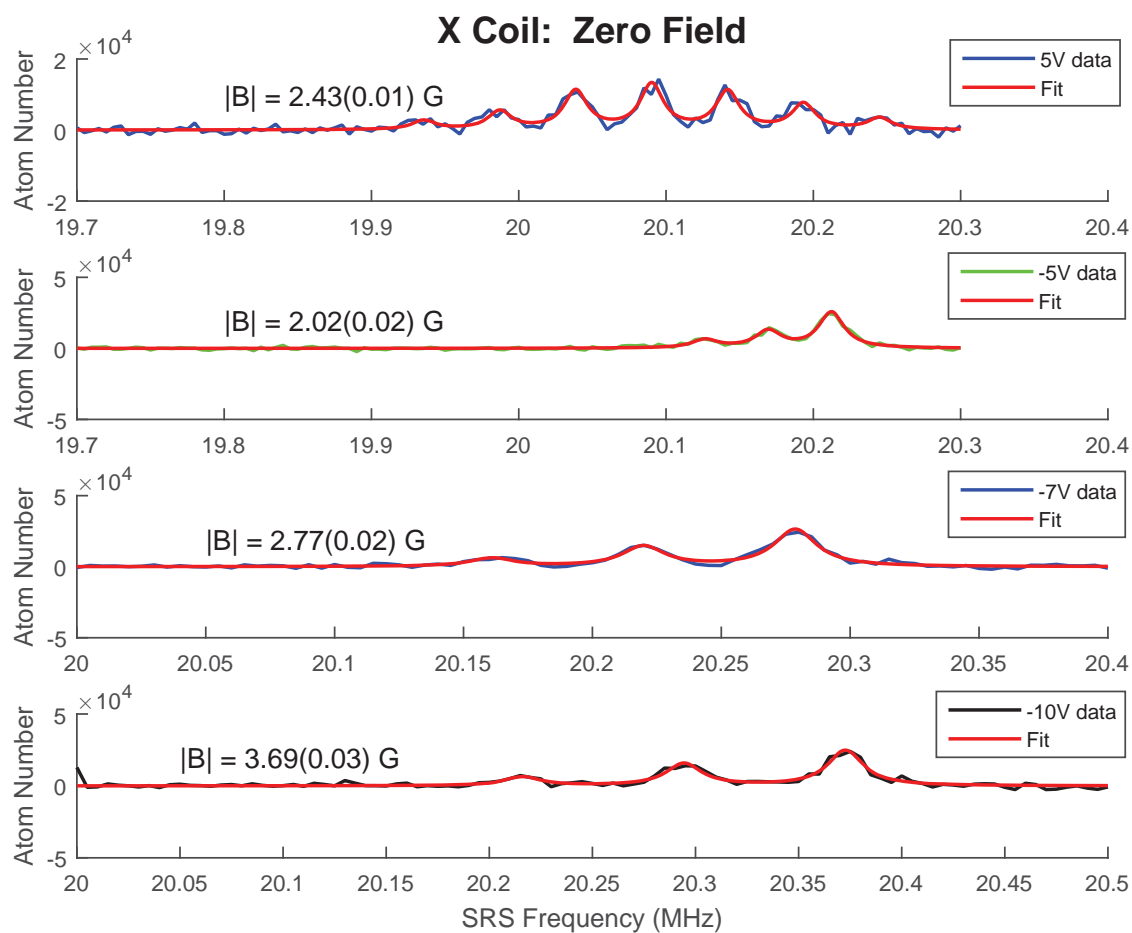


Figure 3.7: Measuring the frequency splitting between different nuclear spin states in order to zero the magnetic field for atoms in the XODT.

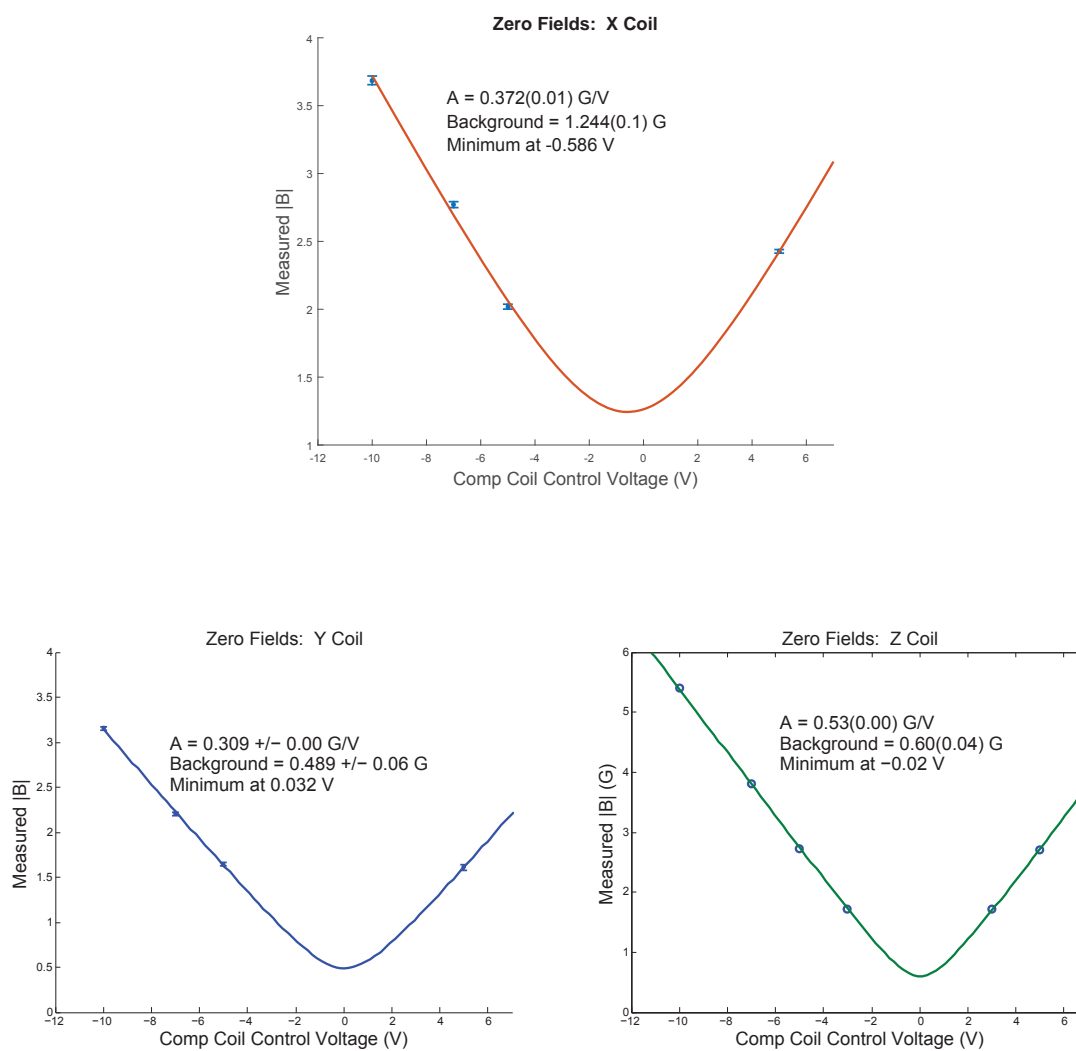


Figure 3.8: Zeroing the magnetic field and calibrating the compensation coils using absorption imaging on the 3P_1 transition. (Each plot is formatted slightly differently, just to annoy you.)

3.3.2 Optical pumping and spin state detection

To prepare an equal mixture of the stretched $m_F = \pm 9/2$ states, we perform optical pumping via the $^1S_0, F = 9/2 \leftrightarrow ^3P_1, F = 9/2$ transition in a 3 G magnetic bias field, which splits neighboring m_F states by 260 kHz. First, a σ^- -polarized (relative to the bias field axis) optical pumping beam is frequency-chirped from the $m_F = -1/2 \rightarrow -3/2$ transition to the $m_F = -7/2 \rightarrow -9/2$ transition, which pumps all $m_F < 0$ atoms into the $m_F = -9/2$ state. In the second step, a liquid crystal waveplate is used to switch the laser polarization to σ^+ , and similarly all the $m_F > 0$ atoms are pumped into the $m_F = 9/2$ state.

In order to get an accurate comparison of the relative number of spin states, we must ensure equal scattering cross sections for each of the spin states. We therefore operate with the absorption imaging laser polarization at a 54.6° to the quantization axis. This is the “magic angle” known from NMR, where $\theta = \cos^{-1}(1/\sqrt{3})$. This gives equal amplitudes of π, σ^- , and σ^+ transitions, which when added together, give the same scattering cross section for each spin state, as shown in Figure 3.9.

3.4 Evaporation

Laser cooling followed by optical pumping to the $m_F = \pm 9/2$ stretched nuclear spin states produces two separate Fermi gases with $m_F = +9/2$ and $m_F = -9/2$, each with an initial phase space density of ≈ 0.1 in the crossed optical dipole trap. (This estimate ignores atoms that are in the HODT but not in the VODT as well, and so the actual phase space density is lower.) Evaporative cooling to degeneracy proceeds by exponentially decreasing the trap depth in a 7 s, two-stage ramp [48, 149]. For different measurement goals, we optimize particular final parameters such as temperature (10 to 60 nK) and atom number (10^4 to 10^5). Figure 3.11 shows a freely expanding degenerate Fermi gas of 4×10^4 atoms. The temperature T and Fermi temperature T_F are determined from a fit to the Fermi-Dirac distribution, giving $T = 60$ nK and $T/T_F = 0.2$.

After evaporation, we are also able to perform a better measurement of our vacuum-limited

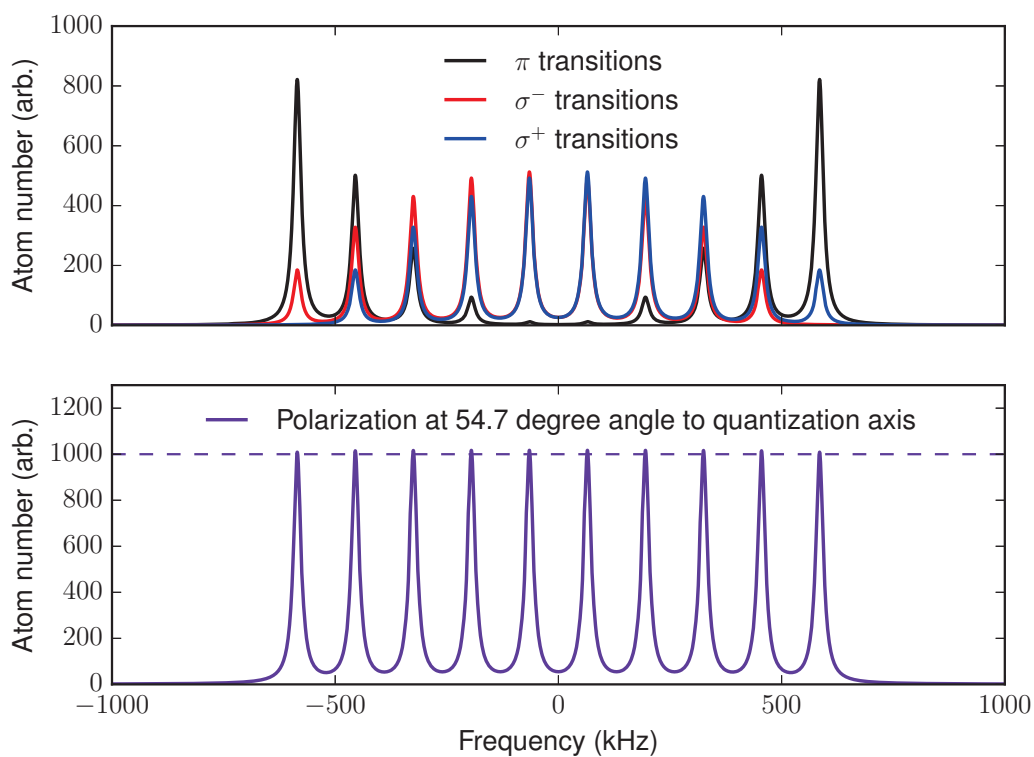


Figure 3.9: Illustration of the transition amplitudes for different polarization configurations with respect to the quantization axis for the $^1S_0, F = 9/2$ to $^3P_1, F = 9/2$ transition.

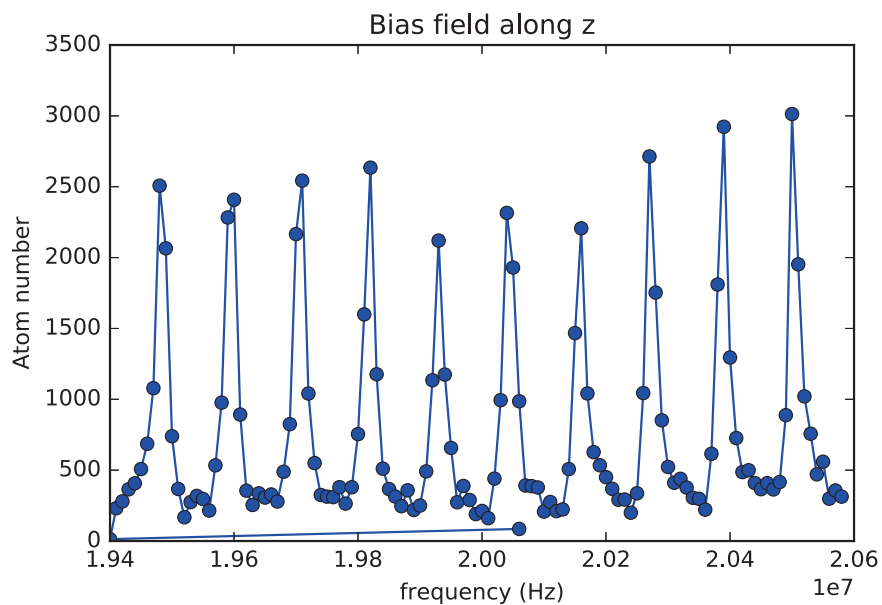


Figure 3.10: Measurement of the mixture of 10 nuclear spin states in the crossed optical dipole trap via absorption imaging on the $^1S_0, F = 9/2$ to $^3P_1, F = 9/2$ transition.

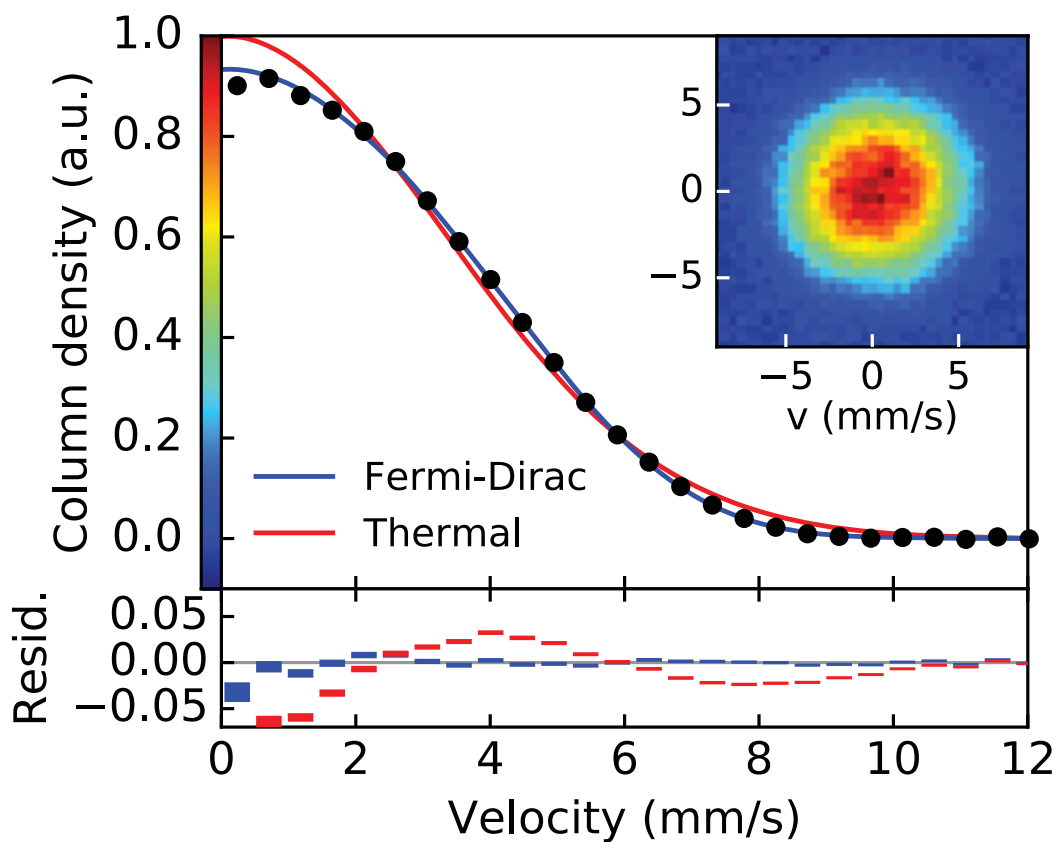


Figure 3.11: Momentum distribution data of a two-spin Fermi gas after being released from the crossed optical dipole trap. The inset shows an absorption image of the freely expanding gas. The azimuthally averaged column density deviates from a Maxwell-Boltzmann fit, but agrees well with a Fermi-Dirac fit giving $T/T_F = 0.2$.

lifetime by ramping the ODT depth back up (so that heating is not mistaken for atom loss) and measuring the number of atoms as a function of time, as shown in Figure 3.12. We measure a $1/e$ lifetime of ≈ 90 s, so we know that our vacuum-limited lifetime is at least that long. In the process of making these measurements, we realized that the atoms are very sensitive to any stray light, especially from our blue laser system, which is on the same optical table. The blue laser system is now housed inside a black plastic box to seal out any stray photons.

3.5 Kapitza-Dirac scattering

Another measurement that can be performed after evaporation is Kapitza-Dirac scattering [82] in order to calibrate the high-resolution top imaging system. To do this, we quickly pulse on one axis of the optical lattice for $4 \mu\text{s}$ which is less than $1/\omega_{\text{rec}}$, where ω_{rec} is the recoil frequency of the particle, given by $\hbar\omega_{\text{rec}} = \hbar^2 k^2 / 2m$, where k is the wavevector of the 813 nm lattice photons, and m is the mass of the strontium atom. In this case, we can disregard the motion of the atoms with respect to the light field (Raman-Nath approximation).

The potential produced by the lattice can be written as $U(z, t) = U_0(t) \sin^2(kz)$ where $U_0(t)$ is the time-dependent envelope for the potential. Then, starting with an initial wavefunction $|\psi_0\rangle$, the wavefunction $|\psi\rangle$ immediately after the lattice is pulsed on and off can be written as,

$$\begin{aligned} |\psi\rangle &= e^{\frac{-i}{\hbar} \int dt U_0(t) \sin^2 kz} |\psi_0\rangle \\ &= e^{-iA} e^{iA \cos 2kz} |\psi_0\rangle, \end{aligned}$$

where,

$$\frac{A}{2} = \frac{1}{\hbar} \int dt U_0(t). \quad (3.5)$$

Using the identity,

$$e^{i\alpha \cos \beta} = \sum_{n=-\infty}^{\infty} i^n J_n(\alpha) e^{in\beta}, \quad (3.6)$$

where J_n are Bessel functions of the first kind, we find,

$$\psi = e^{-iA} \sum_{n=-\infty}^{\infty} i^n J_n(A) e^{in(2kz)} |\psi_0\rangle \quad (3.7)$$

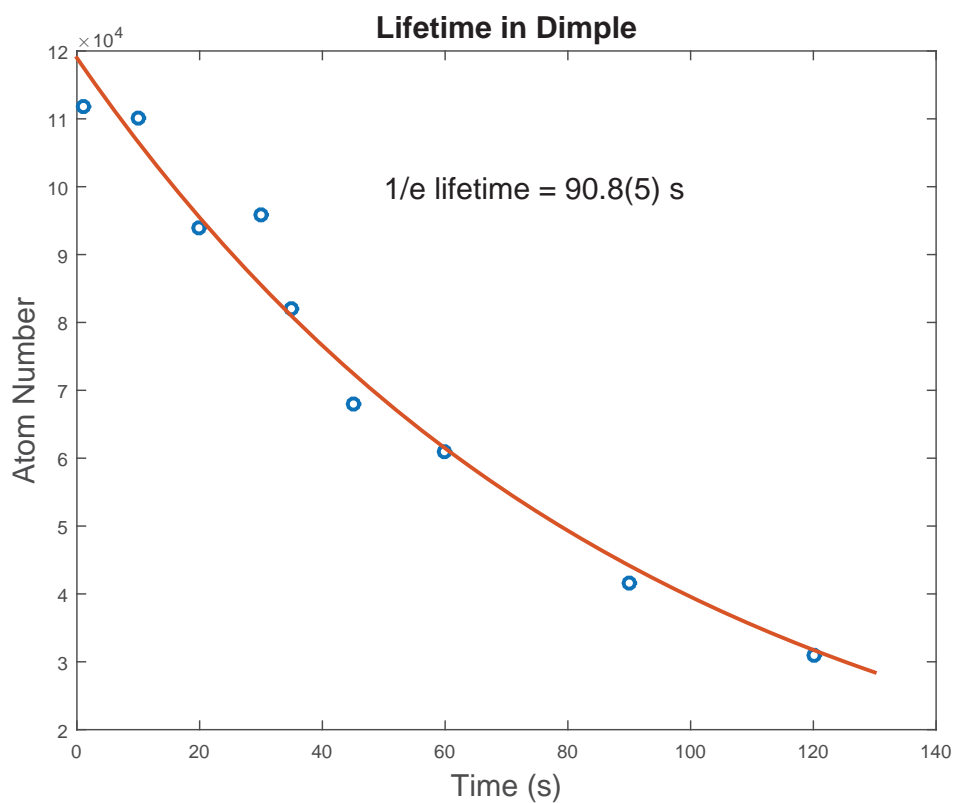


Figure 3.12: Lifetime of ground state atoms in the optical dipole trap, demonstrating that the vacuum lifetime is at least 90 seconds.

Therefore, pulsing the lattice on quickly causes states with momentum $2n\hbar k$ to be populated with probability $J_n(A)$. For our purpose of calibrating the top imaging system, it is sufficient to just know that the momenta will be multiples of $2\hbar k$, where k is the lattice laser wavevector, and so the velocity packets will be multiples of $2h/m\lambda_{813} = 11.28$ mm/s. Then for a time-of-flight τ , we precisely know the distance between the momentum packets will be $(11.28 \text{ mm/s})\tau$ and that is how we calibrate the magnification of the imaging system.

3.6 Lattice loading and characterization

The atoms are then adiabatically loaded from the crossed optical dipole trap into the ground band of a 3D optical lattice. We use the high resolution vertical imaging system for horizontal alignment of the lattice beams to the atom cloud at the end of evaporation. Vertical alignment, however, is trickier, as all dimensions in the vertical direction are smaller and also we do not have high-resolution imaging in the horizontal direction. Initially, we overlapped the location of the atoms at the end of evaporation with the location of the atoms in the lattice loaded directly from the red MOT. However, this was not a very precise method for vertical alignment, as, due to gravitational sag, the position of the thermal atoms in the lattice beam depends on variables such as the beam intensity and atom temperature. A better method of vertical alignment is to use the same technique used to measure the XODT trapping frequency: pulse the lattice on for $400 \mu\text{s}$ and measure dipole oscillations. Measuring the oscillation amplitude for different lattice steering mirror positions enables us to find the center position which causes minimal oscillations in the plane transverse to the vertical beam.

A timing diagram for the loading procedure is shown in Figure 3.14. Whereas in previous stages of the experiment, the atoms were hot enough that we did not have to worry about transients when initially engaging any servos; here, we had to be very careful to make sure that integrator windup (from having the lattice beam intensity servos disengaged until now) and other transients did not add any entropy to the gas. Therefore, we added analog switches across the capacitors for all integrators in the intensity servo circuit so that the integrators are all shorted out until it is

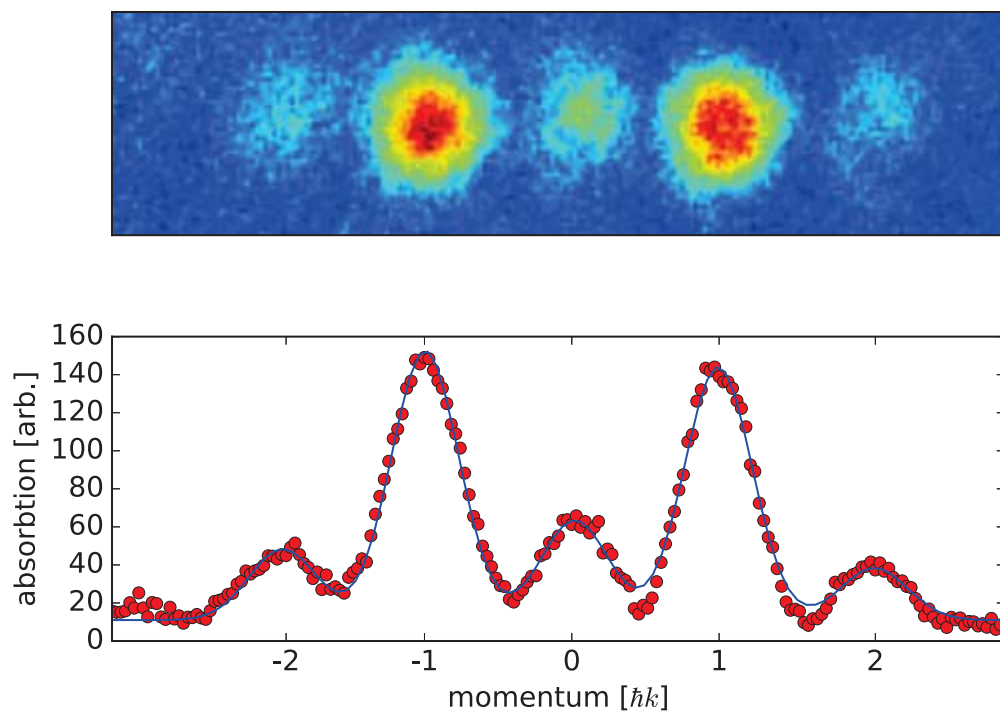


Figure 3.13: Kapitza-Dirac scattering for calibration of the vertical imaging system.

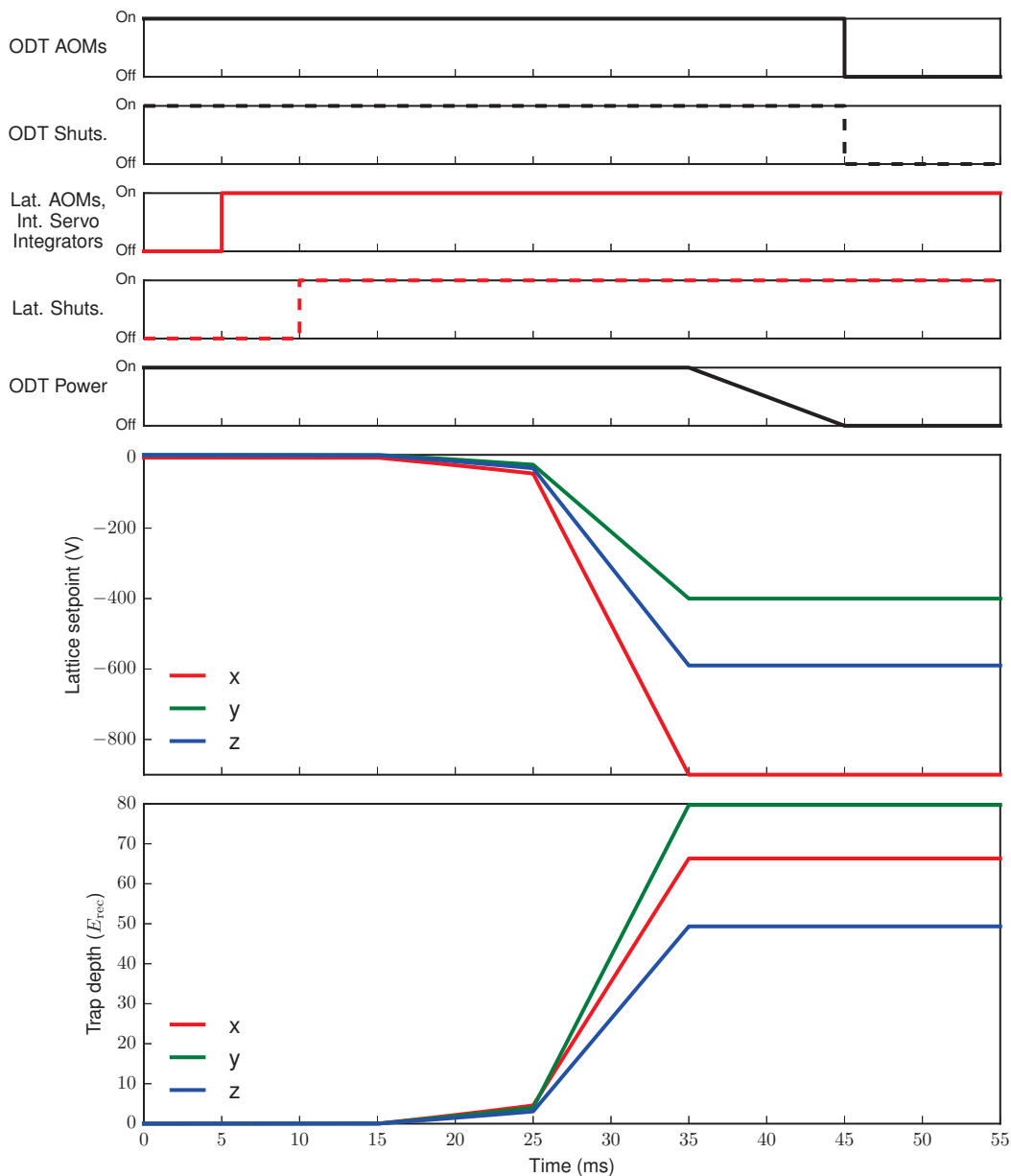


Figure 3.14: Timing diagram for the lattice loading. Importantly, the mechanical shutters for the lattice are close to the experiment, after the in-loop photodiodes used for the intensity servos. Therefore, we can turn on the lattice AOMs and servo integrators before opening the shutters, so that the atoms are protected from any transients resulting from engaging the servos.

time to turn the lattice on. Then the AOMs and integrators are turned on to a very low setpoint voltage while the shutter remains closed so that the atoms are still shielded from any transients while the lattice beams are still being ramped up. Finally, after 5 ms, the shutters are opened.

Loading the ground band requires that $E_F \ll E_{\text{rec}}$, where E_F is the Fermi energy, k_B is the Boltzmann constant, and T is the temperature. As the lattice depth rises, the increasing role of interactions relative to tunneling suppresses multiple occupancies in the Mott-insulating regime. At the final lattice depths of 40 to 100 E_{rec} , where E_{rec} is the lattice photon recoil energy, the Lamb-Dicke requirement is satisfied for clock light along all directions [100].

With a low-entropy Fermi gas loaded into a 3D lattice, clock spectroscopy is then performed on the 698 nm $^1S_0 (|g; m_F\rangle) \leftrightarrow ^3P_0 (|e; m_F\rangle)$ clock transition. As shown in Fig. 3.15, the clock laser propagating along the \hat{x} lattice beam is used for precision spectroscopy, while an oblique clock laser enables a systematic characterization of the lattice via motional sideband spectroscopy (see Fig. 3.16). Adiabatic loading of the lattice with respect to the lattice band spacing is verified by the lack of visible red sidebands in motional sideband spectrum, indicating nearly perfect loading of the ground motional band. For data presented in this thesis, we detected no population in excited bands of the lattice.

However, there are much stricter requirements for adiabaticity when considering interactions between atoms. We quantify the amount of entropy added to the system through a “round-trip” loading from the XODT (crossed optical dipole trap) to the lattice and subsequent unloading of the lattice back into the XODT. We verify lattice loading adiabaticity by measuring the T/T_F both before ramping up the lattice and after a subsequent reversed ramp back into the XODT. For the conditions of $N = 10^5$ and $T = 50$ nK, we observe no increase for $T/T_F = 0.30 \pm 0.05$, which allows us to put a conservative upper bound on the bulk gas entropy for the data in Figs. 3.11 and 4.6. Our lowest-temperature data was taken under different conditions: $N = 10^4$, $T = 15$ nK and $T/T_F = 0.2$. We have verified, again through a round-trip measurement of T/T_F , that loading of such a sample to the lattice is nearly adiabatic. We detected less than a few nK increase in temperature and a 30% loss in atom number, corresponding to a increase in T/T_F of 10%.

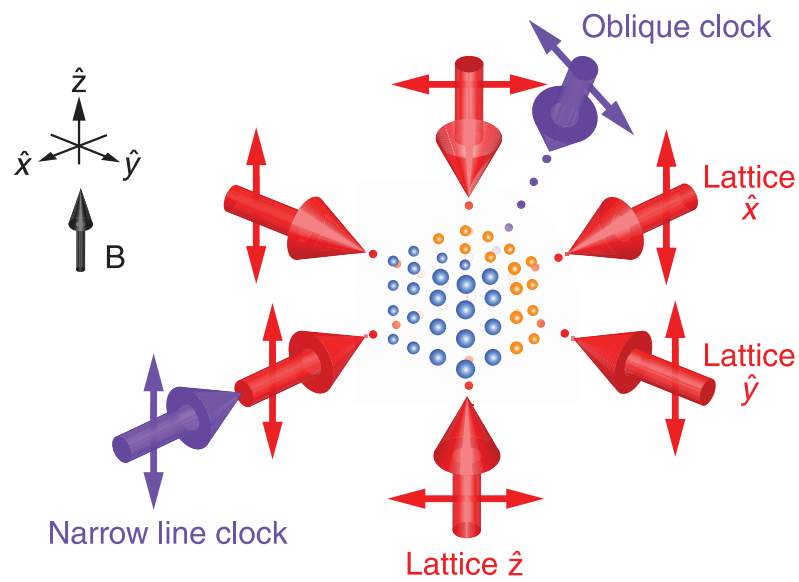


Figure 3.15: Schematic showing propagation direction (large arrows) and polarization (double arrows) of the 3D lattice and clock laser beams. The quantization axis is defined by the magnetic field B . The narrow line clock laser used for precision spectroscopy is phase-stabilized to lattice \hat{x} . The oblique clock laser is used drive motional sidebands along all three lattice axes.

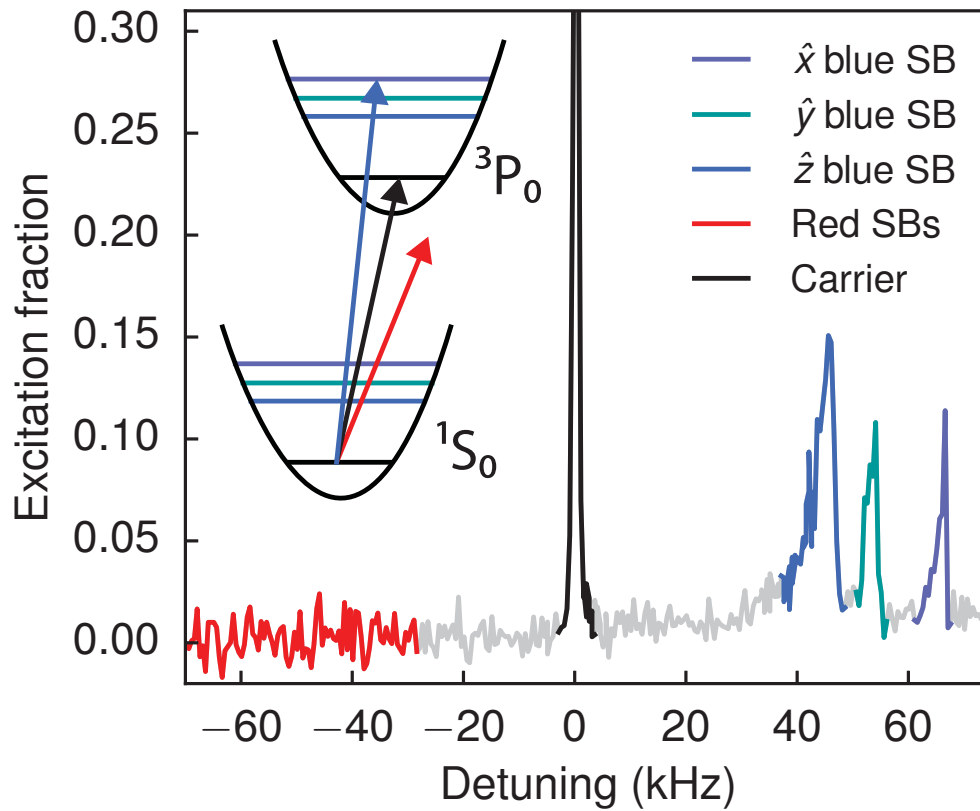


Figure 3.16: Motional sideband spectroscopy using the oblique clock laser shows no observable red sidebands, illustrating that atoms are predominantly in the ground band of the lattice.

Since the interactions between ground state strontium atoms cannot be “turned-off,” we estimate the effects of interactions as compared to a non-interacting system through numerical calculations based on the measured trap frequencies, temperature, and entropy of the bulk Fermi gas before applying the lattice potential.

To estimate suppression of doubly-occupied sites (doublons) in the lattice due to interactions, we use a model which assumes conservation of the total entropy and atom number measured in the XODT to compare the doublon fraction for the interacting and non-interacting cases [80, 142]. For our coldest samples, a large suppression of doublons, as well as a central region of vanishing compressibility, is expected (see Fig. 3.18). The model predicts a doublon fraction more than 100 times smaller than that of the non-interacting case. Clock spectroscopy confirms the suppression of doublons. The next step is to use a high-resolution imaging objective to verify the vanishing compressibility in the center of the trap and the existence of a low-entropy Mott-insulator [80, 142].

(see Fig. 3.17 below). From this investigation, we conclude that we operate our clock in the Mott-insulating regime where atomic interactions suppress the number of doubly-occupied sites (doublons) [80, 142]. We have also explored lower-temperature conditions in the XODT: $N = 10^4$, $T = 15$ nK and $T/T_F = 0.2$ in the XODT. Here, a much greater suppression of doublons, as well as a central region of vanishing compressibility, is expected (see Fig. 3.18 inset). For our coldest samples ($N = 1 \times 10^4$, $T = 15$ nK, $T_F = 0.2$) used in spectroscopy, a non-interacting model would predict a doublon fraction greater than 60%. In contrast, both the interacting model and our clock spectroscopy demonstrate a vanishing number of doublons. This level of suppression of double occupancies is characteristic of a unit-filled Mott-insulator.

The next step in our experiment is to use a high-resolution imaging objective to verify the vanishing compressibility in the center of the trap for a low-entropy Mott-insulator [80, 142].

Accurate temperature measurement in the lattice is experimentally challenging and represents an active area of research. We estimate the temperature in the lattice through numerical calculations based on an interacting model. In the case of $T_{\text{ODT}} = 15$ nK and $N = 1 \times 10^4$ in the XODT, the temperature drops in the lattice yielding $T_{\text{lattice}} = 4$ nK.

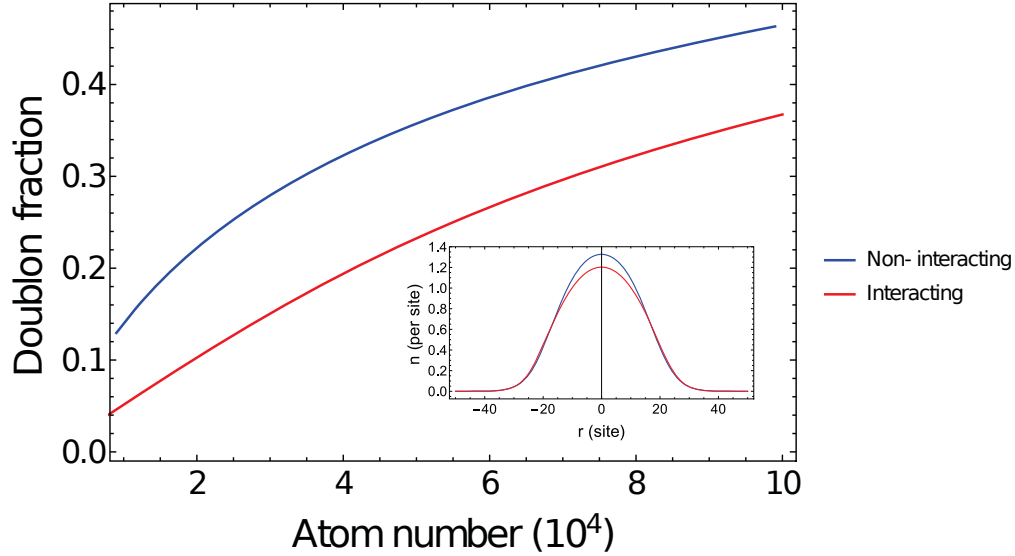


Figure 3.17: Suppression of doubly occupied sites (doublons) in the Mott-insulating regime. A comparison of calculated doublon fraction between interacting and non-interacting cases is plotted for $T = 50$ nK and $T/T_F = 0.2 - 0.4$ in the XODT, depending on atom number. The inset shows the calculated density profile in the lattice for $N = 4 \times 10^4$ and $T/T_F = 0.25$.

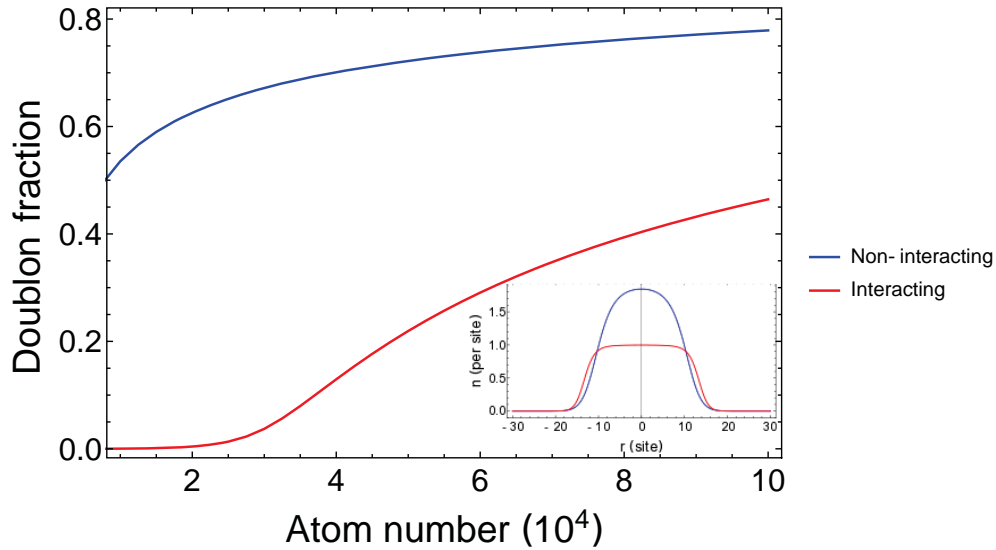


Figure 3.18: Suppression of doubly occupied sites (doublons) in the Mott-insulating regime. A comparison of calculated doublon fraction between interacting and non-interacting cases is plotted for $T = 15$ nK and $T/T_F = 0.1 - 0.2$ in the XODT. The inset shows the calculated density profile in the lattice for $N = 1 \times 10^4$ and $T/T_F = 0.2$. For our coldest samples at $T = 15$ nK and $N = 1 \times 10^4$ used for narrow-line spectroscopy in Fig. 4, the number of doubly occupied sites is greatly suppressed as compared to calculations for the non-interacting case.

Chapter 4

Experiments

Now that we have produced a degenerate Fermi gas, loaded it into the ground band of a 3D optical lattice, and verified doublon suppression, we can finally answer the question: Is it possible to employ correlated quantum matter to enhance *both* stability and accuracy in a state-of-the-art atomic clock?

We still had to do a lot of technical groundwork to answer this question. First, there has been a long-standing question as to whether or not state-independent trapping in a 3D lattice could be achieved at a level to accommodate state-of-the-art narrow line spectroscopy and atomic clock. The challenge arises from complications involving vector and tensor ac Stark shifts, as well as interference between different lattice beams. Next, we had to measure the interaction energies and characterize the clock shifts due to clock transitions occurring for any residual doublons.

With these questions answered, we demonstrated a record quality factor in the first implementation of this new technology. We conclude this chapter by discussing future clock protocols for enhancing stability, and discuss the implications of our work for the stability of future clocks.

4.1 Lattice AC Stark Shifts

There has been a long-standing question as to whether the overall ac Stark shift in a 3D lattice can be managed to allow state-of-the-art narrow line clock spectroscopy. We implement a solution to this challenge, inspired by the proposal in [160]. The differential ac Stark shift from the lattice trapping beams at a particular trap depth \mathcal{U}_0 can be expressed in terms of its scalar, vector,

and tensor components as [160, 25],

$$\Delta\nu = (\Delta\kappa^s + \Delta\kappa^v m_F \xi \hat{e}_k \cdot \hat{e}_B + \Delta\kappa^t \beta) \mathcal{U}_0, \quad (4.1)$$

where $\Delta\kappa^{s,v,t}$ are the scalar, vector, and tensor shift coefficients, respectively, ξ is the lattice light ellipticity, and \hat{e}_k and \hat{e}_B are unit vectors along the lattice beam wave vector and magnetic field quantization axis, respectively. The parameter β can be expressed as $\beta = (3 \cos^2 \theta - 1)[3m_F^2 - F(F + 1)]$, where θ is the angle between the nearly-linear lattice polarization and \hat{e}_B .

4.1.1 Experimental configuration and measurement

We achieve state-independent trapping by operating the lattice at the combined scalar and tensor magic frequency and ensuring that the vector shift is zero [56, 121]. Linearly polarized lattice light ($\xi = 0$) suppresses the vector shift, and the tensor shift is minimally sensitive to drifts in θ when the polarization either parallel ($\theta = 0^\circ$) or perpendicular ($\theta = 90^\circ$) to the quantization axis. The frequency of the trapping light is then tuned to adjust the scalar shift so that it precisely cancels the tensor component. The $\theta = 0^\circ$ configuration has been thoroughly studied in 1D lattice clocks [121, 56]. For the 3D lattice, we set the horizontal (\hat{x}, \hat{y}) and vertical (\hat{z}) lattice polarizations to be parallel and perpendicular to \hat{e}_B , respectively, as shown in Fig. 3.15. The two polarization configurations have distinct magic frequencies due to their different tensor shifts.

We measure the magic frequencies for the vertical and horizontal lattice beams. A continuous-wave Ti:Sapphire laser is used for the lattice light because of its low incoherent background [144]. The absolute frequency of the lattice laser is traceable to the UTC NIST timescale through an optical frequency comb. For a given lattice laser frequency, we measure the differential ac Stark shift using four interleaved digital servos that lock the clock laser frequency to the atomic resonance for alternating high and low lattice intensities and $m_F = \pm 9/2$ spin states [23, 121, 56]. From the data shown in Figure 4.2, we measure that the vertical ($\theta = 90^\circ$) and horizontal ($\theta = 0^\circ$) magic frequencies are 368.554839(5) THz and 368.554499(8) THz, respectively, in agreement with [121, 56, 144]. From these two magic frequencies, we find that the scalar magic frequency is

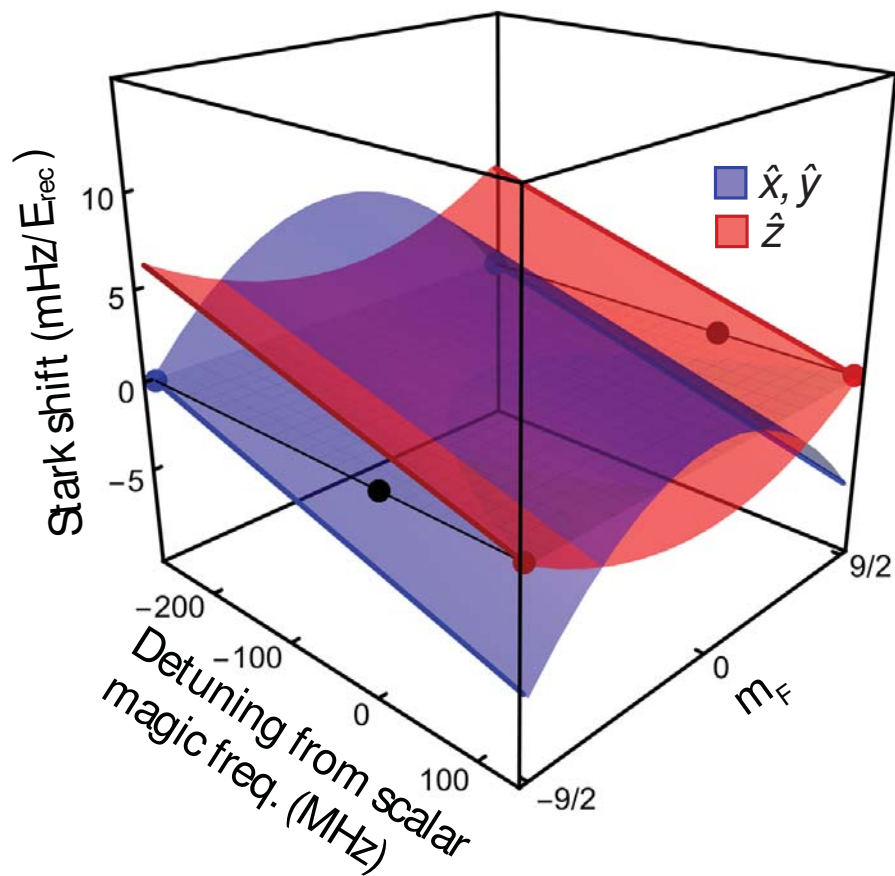


Figure 4.1: Depiction of the different lattice AC stark shifts for the two different beam orientations, showing the quadratic dependence of the tensor component on the nuclear spin state.

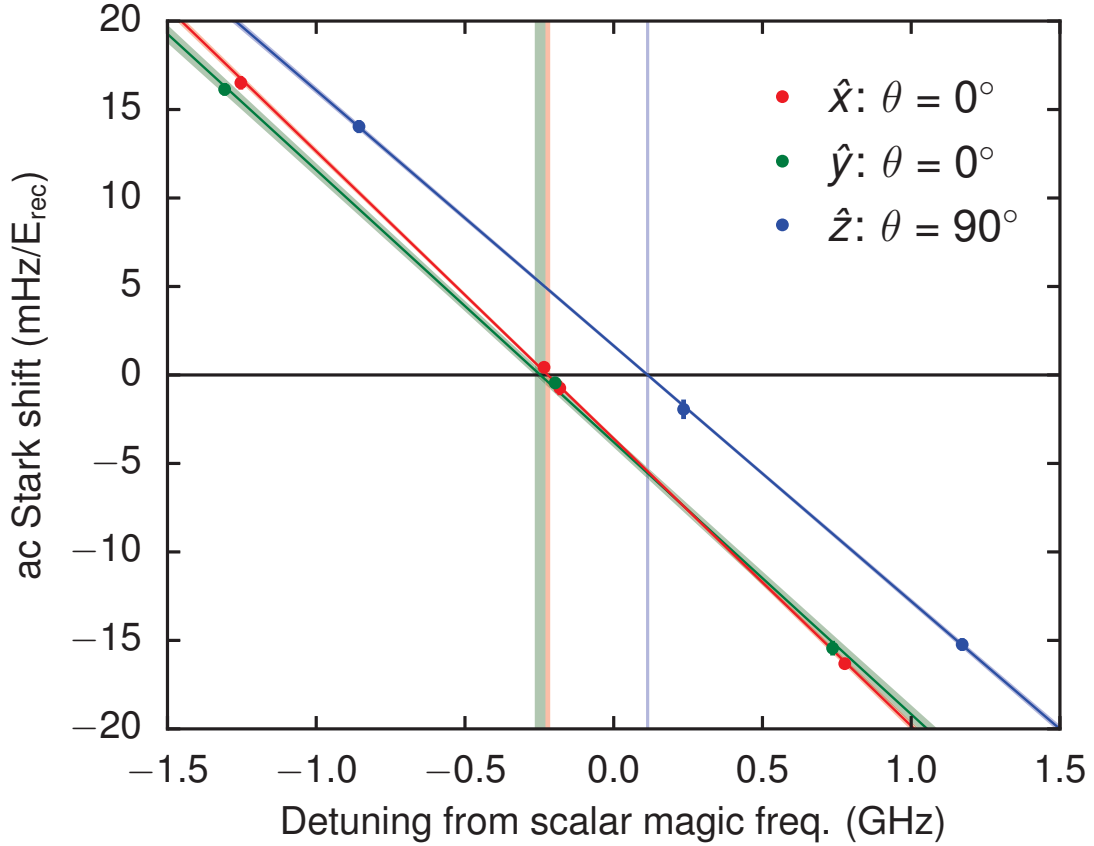


Figure 4.2: Determination of the magic wavelengths for the horizontal (\hat{x}, \hat{y}) and vertical (\hat{z}) lattices, with $|m_F| = 9/2$. The vertical and horizontal lattices have distinct magic wavelengths due to their different tensor shifts arising from different angles θ between the lattice polarization and magnetic field quantization axes. For presentation, the measured frequency shift is scaled by the difference in peak trap depths at the high and low lattice intensities. The difference in slopes is caused by trapping potential inhomogeneities and does not affect the determination of the magic frequencies.

368.554726(4) THz, in agreement with [144].

Since there are only two θ configurations with a stable tensor shift, in a 3D lattice two of the three lattice beams will necessarily have the same magic frequency. However, the frequencies of all lattice beams must be offset to avoid interference, which is known to cause heating in ultracold quantum gas experiments [107]. We choose our two horizontal beams to have the same polarization and operate them with equal and opposite detunings (± 2.5 MHz) from their magic frequency, giving equal and opposite ac Stark shifts from the two beams. From the slopes in Fig. 4.2, we determine that for a 10% imbalance in trap depths, detuning the two horizontal beams ± 2.5 MHz from their magic wavelength results in a $< 1 \times 10^{-18}$ systematic shift, the exact magnitude of which can be measured to much better accuracy.

Another issue resulting from our 3D geometry is that one lattice beam must operate with $\hat{e}_k \cdot \hat{e}_B = 1$, which can give rise to a vector ac Stark shift due to residual circular polarization. The vertical (\hat{z}) beam has this configuration, and we measure a $3 \times 10^{-18} \times m_F/E_{\text{rec}}$ vector shift, corresponding to an ellipticity of $\xi = 0.007$ [160]. In contrast, the horizontal beams (\hat{x}, \hat{y}) with $\hat{e}_k \cdot \hat{e}_B = 0$ enjoy an additional level of vector shift suppression. Nevertheless, the clock operates by locking to alternating opposite $m_F = \pm 9/2$ spin states, so the net vector shift is removed by averaging the two spin states, the same as for the 1st order Zeeman effect.

4.1.2 Data analysis and statistical methods

“Yo dawg, I heard you like precision measurement. So I put some systematics on your systematics.” -Xzibit

Elimination of systematic shifts and accurate error estimation are the two complementary cornerstones of precision measurement; in this section, we discuss our techniques for handling both. We evaluate the ac Stark shift using four interleaved but independent servos locked to the $m_F = \pm 9/2$ transitions for each of the high and low lattice intensity configurations, with high and low lattice depths differing by approximately $30E_{\text{rec}}$. Each servo tracks the detuning between one

transition of the strontium atoms and the TEM00 mode of an ultra-stable cavity [109].

Laser frequency drift gives a nonuniform shift to the interleaved locks that can lead to an erroneous systematic offset in the measured ac Stark shift. Every four experimental cycles, we measure independent frequencies locked to the four configurations $\{f_{\text{high},+9/2}^i, f_{\text{low},+9/2}^i, f_{\text{high},-9/2}^i, f_{\text{low},-9/2}^i\}$, where high and low refer to lattice depths, $\pm 9/2$ refer to the m_F states, and i is the iteration number of the experiment. A four-point string analysis [53, 112] removes linear and quadratic laser drift using the following linear combination of eight consecutive measurements:

$$\begin{aligned} \Delta f_{\text{scalar+tensor}}^i &= \frac{3}{16} \left(f_{\text{high},+9/2}^i + f_{\text{high},-9/2}^i \right) - \frac{5}{16} \left(f_{\text{low},+9/2}^i + f_{\text{low},-9/2}^i \right) \\ &\quad + \frac{5}{16} \left(f_{\text{high},+9/2}^{i+1} + f_{\text{high},-9/2}^{i+1} \right) - \frac{3}{16} \left(f_{\text{low},+9/2}^{i+1} + f_{\text{low},-9/2}^{i+1} \right), \end{aligned} \quad (4.2)$$

$$\begin{aligned} \Delta f_{\text{vector}}^i &= \frac{3}{16} \left(f_{\text{high},+9/2}^i - f_{\text{high},-9/2}^i \right) - \frac{5}{16} \left(f_{\text{low},+9/2}^i - f_{\text{low},-9/2}^i \right) \\ &\quad + \frac{5}{16} \left(f_{\text{high},+9/2}^{i+1} - f_{\text{high},-9/2}^{i+1} \right) - \frac{3}{16} \left(f_{\text{low},+9/2}^{i+1} - f_{\text{low},-9/2}^{i+1} \right). \end{aligned} \quad (4.3)$$

In addition to the dominant effect of clock laser reference cavity drift, this technique of point string analysis also removes systematic offsets due to linear and quadratic drifts in uncontrolled systematics, including shifts from room temperature BBR, a drifting quadratic Zeeman shift due to background magnetic field fluctuations, and potential DC Stark effects. It is crucial to perform the analysis in this way so that we extract frequency changes corresponding to the one systematic we are modulating: the AC Stark effect.

With systematic shifts mitigated, we now turn to proper estimation of statistical error. In previous clock experiments with an ≈ 1 s duty cycle, the interleaved servos were able to adequately track the fundamental “ $1/f$ ” noise from the local oscillator. However, thus far, our new degenerate gas experiment has not been optimized for quick evaporation and thus runs on an ≈ 20 s duty cycle where $1/f$ noise plays a role. The measured frequencies are then correlated in time because the servos low-pass filter the system response. We correct the servo frequency using the error signal,

which contains higher-frequency components of the system response, according to,

$$f_{\text{corrected}} = f_{\text{uncorrected}} + \frac{\Gamma}{2A} \times e, \quad (4.4)$$

where Γ is the FWHM linewidth, e is the error signal (the difference between the excitation fraction from probing the left and right sides of the line), and A is the maximum peak height of the spectroscopic feature. Fig. 4.3 demonstrates that this procedure flattens the autocorrelation function of the corrected data (blue) compared to the uncorrected data (green).

To estimate the autocorrelation function from the data, we use the formula [13],

$$\rho_j = \frac{\sum_{i=1}^{n-j} [X_i - \bar{X}(n)][X_{i+j} - \bar{X}(n)]}{(n-j)S^2(n)}, \quad S^2(n) = \frac{\sum_{i=1}^n [X_i - \bar{X}(n)]^2}{n(n-1)}. \quad (4.5)$$

The standard deviation of the mean is only a good measure of error when the noise is Gaussian and the data points that are averaged together are statistically independent; it underestimates the error when the data is correlated and overestimates the error when the data is anti-correlated. We must therefore use the autocorrelation function to calculate the unbiased error for correlated data,

$$\frac{\sigma}{\sqrt{n}} \sqrt{1 + 2 \sum_{j=1}^{n-1} \left(1 - \frac{j}{n}\right) \rho_j}, \quad (4.6)$$

where σ is the standard deviation of the point-string difference frequencies Δf^i , ρ_j is the autocorrelation function for data separated by j points, and n is the number of measured frequencies [13].

This empirical formula for the autocorrelation function is known to be unreliable unless one uses hundreds of data points (we only had tens of data points for each measurement), so to verify the validity of this technique, all of these steps are validated on simulated data modeled by clock laser noise similar to the actual laser [19], with a power spectral density $S \propto 1/f$, where f is the frequency, and a linear frequency drift from imperfectly canceled material creep of the reference cavity between -2 and 2 mHz/s. We use weighted least-squares fitting to determine the magic wavelength for each lattice direction. From the difference in the splittings between the $\pm 9/2$ states for the high and low lattice intensities, we also extract the vector ac Stark shift, as shown in Fig. 4.4.

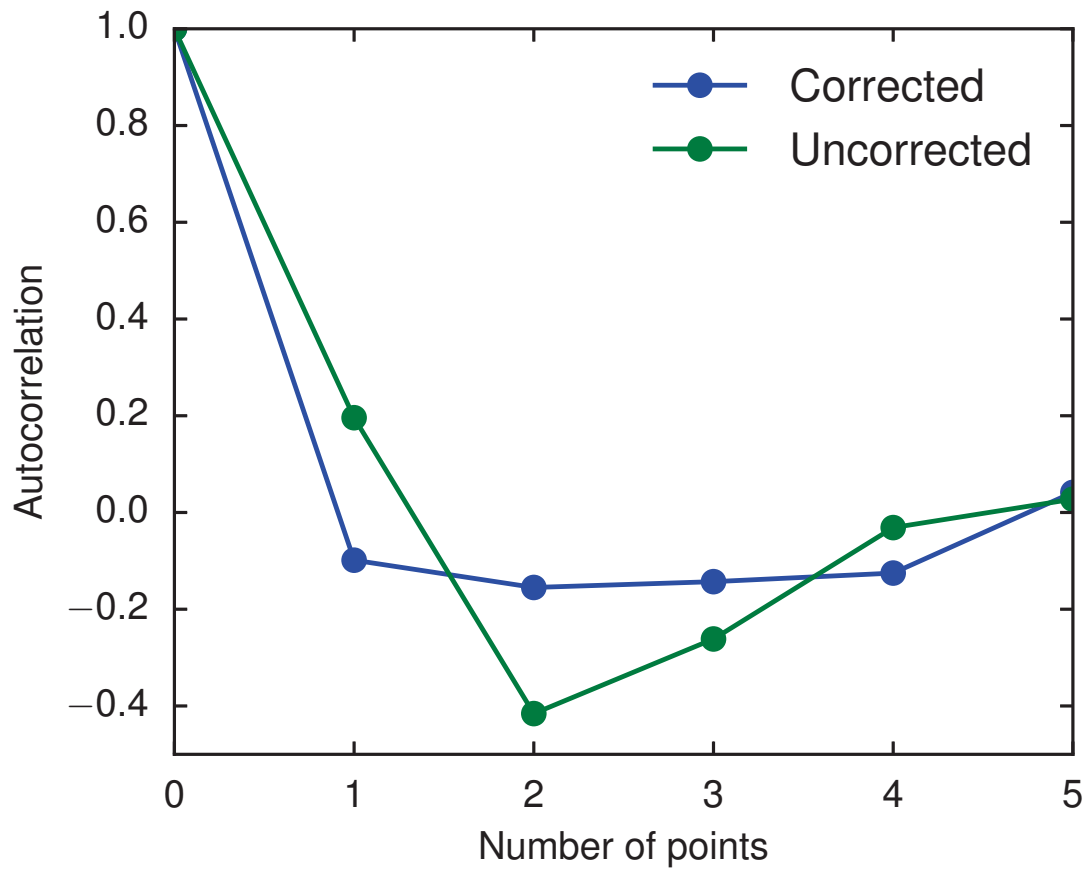


Figure 4.3: Autocorrelation functions of the measured ac Stark shifts for clock laser servo frequencies uncorrected (green) and corrected by the measured error signal (blue).

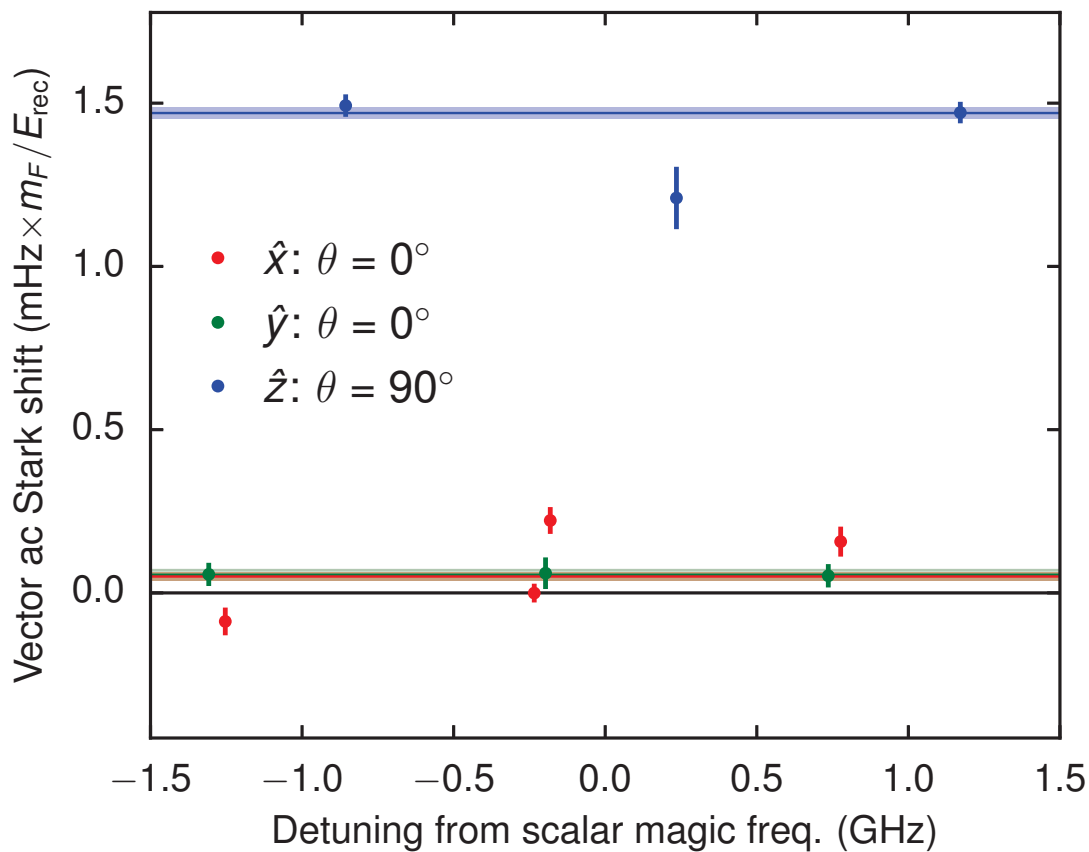


Figure 4.4: Measuring the vector ac Stark shift for the horizontal (\hat{x}, \hat{y}) and vertical (\hat{z}) configurations. The vector shift from the vertical lattice beam is sensitive to a small ellipticity in the polarization because $\hat{e}_k \cdot \hat{e}_B = 1$, while the horizontal beams with $\hat{e}_k \cdot \hat{e}_B = 0$ benefit from additional suppression of the vector shift.

The reduced chi-squared χ_{red}^2 provides some estimate of whether or not we modeled the noise properly. Note that according to [8], it is bad practice to rescale the error bars such that $\chi_{\text{red}}^2 = 1$, as this assumes that the noise is Gaussian (it is not: it is dominantly $1/f$ noise), the model is linear in all parameters (it is not: the frequency lists come from a digital servo which includes a double integrator), and it already assumes that the noise model is correct (it might not be: that is the point of using χ_{red}^2 to test whether it is!).

4.2 Interactions

4.2.1 On-site contact interactions

In the ground band of the lattice, each site can be occupied by either one atom, or by two atoms with opposite nuclear spin. Tight confinement in the 3D lattice gives rise to strong interactions on doubly occupied sites. We label the two-particle eigenstates of the two-orbital interaction Hamiltonian as $|gg; m_F, m'_F\rangle = |gg\rangle \otimes |s\rangle$, $|eg^+; m_F, m'_F\rangle = (|eg\rangle + |ge\rangle)/\sqrt{2} \otimes |s\rangle$, $|eg^-; m_F, m'_F\rangle = (|eg\rangle - |ge\rangle)/\sqrt{2} \otimes |t\rangle$, and $|ee; m_F, m'_F\rangle = |ee\rangle \otimes |t\rangle$ with corresponding energies U_{gg} , U_{eg}^+ , U_{eg}^- , and U_{ee} [61, 171, 138, 31]. Here, $|s\rangle$ and $|t\rangle$ represent the singlet and triplet wavefunctions for the two spins, m_F and m'_F . A schematic showing the relative energy levels and symmetries of these eigenstates is shown in Figure 4.5. An applied magnetic bias field mixes the $|eg^+; m_F, m'_F\rangle$ and $|eg^-; m_F, m'_F\rangle$ states due to a differential Landé g -factor between the two orbitals. We label the new eigenstates of the combined interaction and Zeeman Hamiltonian as $|eg^u; m_F, m'_F\rangle$ and $|eg^d; m_F, m'_F\rangle$.

Clock light resonantly couples the ground state $|gg; m_F, m'_F\rangle$ only to the states $|eg^{u,d}; m_F, m'_F\rangle$. The energies U_{eg}^+ and U_{eg}^- differ from U_{gg} on the h -kHz scale, where h is the Planck constant, resulting in transitions on doubly occupied sites that are well-resolved from the single-atom clock transitions and strong suppression of two-photon transitions to the $|ee; m_F, m'_F\rangle$ state. In 1D optical lattice clocks, interaction shifts are less than clock transition Rabi frequencies; in 2D clocks, interaction shifts and Rabi frequencies are comparable [152]. In contrast, the interaction shifts in

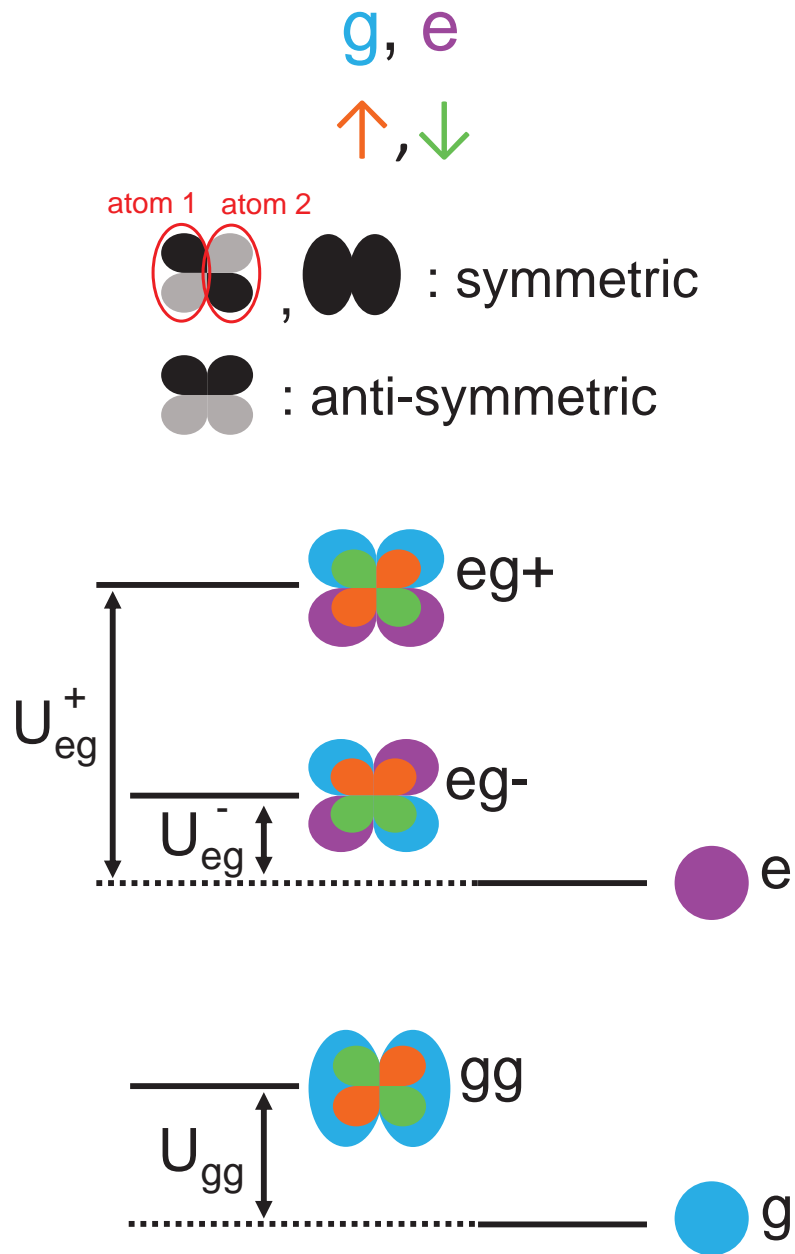


Figure 4.5: Level diagram showing transitions for lattice sites with one atoms and two atoms at zero magnetic field.

a 3D lattice are 10^3 times greater than the clock transition Rabi frequency. Although for normal clock operation we load at most one atom per site, to measure contact interactions we increase the final Fermi temperature so that a small fraction of lattice sites are filled with two atoms in the $|gg; +9/2, -9/2\rangle$ state. Fig. 4.6A shows clock spectroscopy for a magnetic field $B = 500$ mG. At this field, π -polarized clock light gives a negligible transition amplitude to the $|eg^u; +9/2, -9/2\rangle$ state due to destructive interference between the two oppositely signed transition dipole moments for the stretched states. Therefore, we observe excitation to the $|eg^d; +9/2, -9/2\rangle$ state, highlighted in red, and no excitation to the $|eg^u; +9/2, -9/2\rangle$ state, highlighted in blue.

Clock operation predominantly probes atoms in singly occupied sites, with only a negligible systematic shift due to line pulling caused by transitions from the few atoms in doubly occupied sites. For a comprehensive study of line pulling from doubly occupied sites, we use our measurements of $U_{eg}^- - U_{gg}$ and $U_{eg}^+ - U_{gg}$ at $B = 0$ to calculate the spectrum of all transitions on doubly occupied sites as a function of B , as shown in Fig. 4.6 B. We account for imperfect clock laser polarization and residual spin populations by considering π, σ^+ , and σ^- transitions to all $|eg^{u,d}; m_F, m'_F\rangle$ states, as indicated in the shaded regions in Fig. 4.6B. At intermediate magnetic fields, transitions from doubly occupied sites can cross clock transitions and potentially cause significant frequency shifts. However, this is avoided if B is kept sufficiently low. At our chosen bias field of 500 mG [23, 121], transitions on doubly occupied sites are at least 500 Hz away. From a 1% upper bound on residual transition amplitudes, we estimate the fractional frequency shift due to line pulling effects from doubly occupied sites to be below 1×10^{-24} for 1 Hz linewidths. We also calculate the fractional frequency shifts due to superexchange interactions [156] between neighboring sites at typical lattice depths and find them to be below 1×10^{-22} .

While on-site interaction shifts can be eliminated in 3D lattice clocks, atoms may also interact via long-range electric dipole forces, which can lead to many-body effects such as collective frequency shifts, superradiance, and subradiance [28]. At unit filling, clock shifts from dipolar interactions could reach the 10^{-18} level [32, 93], though employing different 3D lattice geometries is a promising approach for canceling these shifts. Exploring different strategies for accurately measuring and

eliminating dipolar frequency shifts will be a fruitful avenue of future study.

We calculate the detunings of transitions from doubly occupied sites, relative to the single-atom clock transition $|g; m_F\rangle \rightarrow |e; m_F\rangle$ at zero magnetic field. Since the clock operates under a magnetic bias field B , we consider how competing Zeeman and interaction energies determine the energy eigenstates for atoms on doubly occupied sites with arbitrary m_1 and m_2 . The Zeeman shifts for $|g; m_F\rangle$ and $|e; m_F\rangle$ are $g_I \mu_B B m_F$ and $(g_I + \delta g) \mu_B B m_F$, where g_I is the nuclear g -factor ($g_I \mu_B = h \cdot 184.4$ Hz/Gauss) and δg is the differential g -factor between the ground and clock states ($\delta g \mu_B = h \cdot 108.4$ Hz/Gauss). The differential Zeeman shift between the two clock states introduces a coupling between the $|eg^+; m_1, m_2\rangle$ and $|eg^-; m_1, m_2\rangle$ states. Thus, the combined interaction and differential Zeeman Hamiltonian in the $|eg^\pm; m_1, m_2\rangle$ basis can be expressed as [171, 138]:

$$\hat{H} = \begin{pmatrix} U_{eg}^+ + \frac{\Delta_1 + \Delta_2}{2} & \frac{\Delta_1 - \Delta_2}{2} \\ \frac{\Delta_1 - \Delta_2}{2} & U_{eg}^- + \frac{\Delta_1 + \Delta_2}{2} \end{pmatrix}, \quad (4.7)$$

where $\Delta_{1,2} = \delta g \mu_B B m_{1,2}$ are the differential Zeeman shifts. The two eigenstates $|eg^u; m_1, m_2\rangle$ and $|eg^d; m_1, m_2\rangle$ have eigenenergies given by,

$$E_{\{u,d\}}(m_1, m_2) = V + \frac{\Delta_1 + \Delta_2}{2} \pm \sqrt{V_{\text{ex}}^2 + \left(\frac{\Delta_1 - \Delta_2}{2}\right)^2}, \quad (4.8)$$

where $V = (U_{eg}^+ + U_{eg}^-)/2$ and $V_{\text{ex}} = (U_{eg}^+ - U_{eg}^-)/2$ are the direct and exchange interaction energies, respectively. The detunings of the $|gg; m_1, m_2\rangle \rightarrow |eg^{\{u,d\}}; m'_1, m'_2\rangle$ transitions relative to the $B = 0$ single-atom clock transition are,

$$\Delta E_{\{u,d\}}(m_1, m_2; m'_1, m'_2) = E_{\{u,d\}}(m'_1, m'_2) - U_{gg} + g_I \mu_B B (m'_1 + m'_2 - m_1 - m_2), \quad (4.9)$$

when the two-particle Rabi couplings $\Omega^{\{u,d\}}(m_1, m_2; m'_1, m'_2; q)$ with $\pi(q = 0)$ or $\sigma^\pm(q = \mp 1)$ -polarized clock light are non-zero, as discussed below.

The atom-light Hamiltonian for a single particle driven by $\pi(\sigma^\pm)$ -polarized clock light is given by,

$$\hat{H}_q^{(1)} = \frac{\hbar}{2} \sum_{m_F} (\Omega_{m_F, q} |e; m_F - q\rangle \langle g; m_F| + \text{h.c.}), \quad (4.10)$$

Here, the single-particle coupling $\Omega_{m_F, q}$ is expressed using the Wigner-Eckart theorem as,

$$\Omega_{m_F, q} = -\langle F_g, m_F; 1, q | F_e, m_F - q \rangle \langle F_g || d || F_e \rangle \cdot \frac{\mathcal{E}_q}{\hbar}, \quad (4.11)$$

where $\langle F_g || d || F_e \rangle$ is the reduced matrix element and \mathcal{E}_q is the electric field amplitude. Then, the two-particle atom-light Hamiltonian is written as,

$$\hat{H}_q^{(2)} = \left(\hat{H}_q^{(1)} \right)_1 \otimes (\mathbb{1})_2 + (\mathbb{1})_1 \otimes \left(\hat{H}_q^{(1)} \right)_2. \quad (4.12)$$

We find the two-particle couplings $\Omega^\pm(m_1, m_2; m'_1, m'_2; q)$ between the $|gg; m_1, m_2\rangle$ and $|eg^\pm; m'_1, m'_2\rangle$ transitions, driven by $\pi(q=0)$ - or $\sigma^\pm(q=\mp 1)$ -polarized clock beams to be,

$$\begin{aligned} \frac{\hbar}{2} \Omega^\pm(m_1, m_2; m'_1, m'_2; q) &= \langle eg^\pm; m'_1, m'_2 | \hat{H}_q^{(2)} | gg; m_1, m_2 \rangle \\ &= \frac{\hbar}{2\sqrt{2}} \left[\Omega_{m_1, q} \left(\delta_{m'_1, m_1 - q} \delta_{m'_2, m_2} \mp \delta_{m'_1, m_2} \delta_{m'_2, m_1 - q} \right) \right. \\ &\quad \left. + \Omega_{m_2, q} \left(\pm \delta_{m'_1, m_1} \delta_{m'_2, m_2 - q} - \delta_{m'_1, m_2 - q} \delta_{m'_2, m_1} \right) \right]. \quad (4.13) \end{aligned}$$

Thus, the two-particle couplings $\Omega^{\{u, d\}}(m_1, m_2; m'_1, m'_2; q)$ between the $|gg; m_1, m_2\rangle$ and $|eg^{\{u, d\}}; m'_1, m'_2\rangle$ states at a given B are obtained from linear combinations of Eq. 4.13. Fig. 4.7 shows all the detunings $\Delta E_{\{u, d\}}(m_1, m_2; m'_1, m'_2)$ from Eq. 4.9 for non-zero $\Omega^{\{u, d\}}(m_1, m_2; m'_1, m'_2; q)$ with π (black lines), σ^+ (red lines), and σ^- (blue lines) clock laser polarizations, as well as all single-atom transitions. In the case of an equal mixture of $m_F = \pm 9/2$ stretched states, the π -polarized clock light does not drive the $|gg; 9/2, -9/2\rangle \rightarrow |eg^+; 9/2, -9/2\rangle$ transition, since $\Omega_{m_1=9/2, q=0} = -\Omega_{m_2=-9/2, q=0}$ gives zero coupling strength as seen in Eq. 4.13. At our operating B , $|eg^u\rangle \approx |eg^+\rangle$, so π -polarized clock light only drives the $|gg; 9/2, -9/2\rangle \rightarrow |eg^d; 9/2, -9/2\rangle$ transition, as shown in Fig. 4.6 A.

Next, we investigate line pulling effects due to the additional lines shown in Fig. 4.7. Single-particle line pulling effects have already been discussed in [56]; here we focus on line pulling from transitions on doubly occupied sites. We approximate the lineshapes as Lorentzians with full width at half maximum Γ . For typical clock operation, the error signal ε for the digital PID that steers the clock laser center frequency f_0 to the atomic resonance is generated by measuring the normalized

excitation fraction N_{exc} at $f_0 + \Gamma/2$ and at $f_0 - \Gamma/2$ [23, 121]. The clock frequency is locked to the atomic reference such that $\varepsilon = N_{\text{exc}}(f_0 - \Gamma/2) - N_{\text{exc}}(f_0 + \Gamma/2) = 0$. In Fig. 4.8, we study how an additional line with a given amplitude relative to the clock transition modifies the center frequency f_0 for which $\varepsilon = 0$. Transitions from atoms on doubly occupied sites begin to overlap with the clock transitions when $B > (U_{gg} - U_{eg}^-)/[(9\delta g + g_I)\mu_B]$. At our chosen bias field of 500 mG [121, 23], the transitions on doubly occupied sites are separated from the main clock transitions by at least 500 Hz. Using a 1% upper bound on residual transition amplitudes and assuming 1 Hz transition linewidths, we estimate the fractional frequency shift due to line pulling effects from doubly occupied sites to be below 1×10^{-24} . If one were to operate their clock using Ramsey spectroscopy (instead of Rabi), we recommend first performing a narrow Rabi “clean-up” pulse to the excited state, removing all ground state atoms (including residual doublons), and then performing “top-down” Ramsey spectroscopy. Then the preceding discussion of systematic effects due to doublons is still valid.

4.2.2 Dipolar interactions

With shifts from on-site interactions now eliminated in 3D lattice clocks, we must now consider long-range electric dipole interactions, which can lead to many-body effects such as collective frequency shifts, superradiance, and subradiance [28]. At unity filling, clock shifts from dipolar interactions could reach the 10^{-18} level [32, 93], but there are strategies for accurately measuring and eliminating these shifts. Exploring different lattice configurations is a promising avenue for canceling dipolar frequency shifts. Also, since the dipolar shift scales with the filling fraction ρ as $\rho^{2/3}$, clocks can measure these systematic effects with Ramsey spectroscopy by modulating ρ [109]. Future studies of dipolar interactions in quantum degenerate lattice clocks will not only be necessary for clock accuracy but will also provide powerful connections to other physical systems based on polar molecules [167, 118], Rydberg gases [139], and magnetic atoms [4, 45, 81, 29].

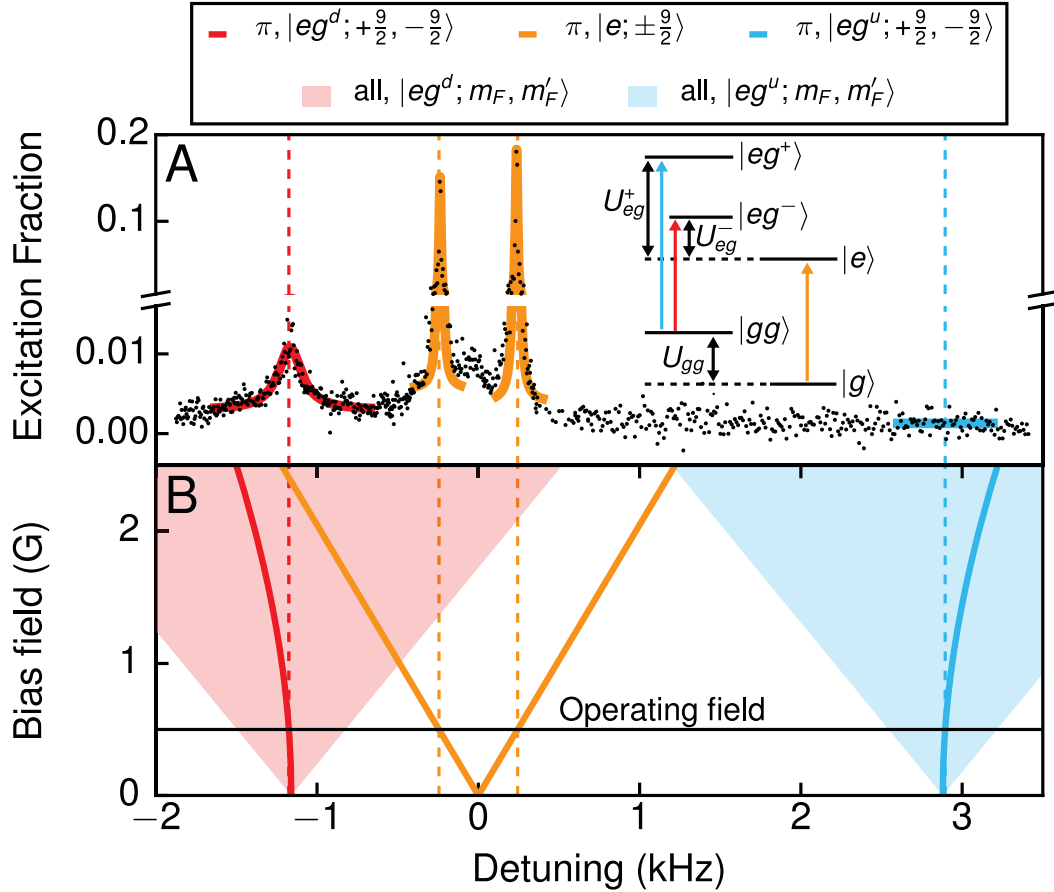


Figure 4.6: (A) Clock spectroscopy data of a two-spin Fermi gas in the $m_F = \pm 9/2$ stretched states for a 500 mG magnetic field, where a small fraction of the lattice sites contain both spin states. All transitions are saturated. The $|gg; -9/2, 9/2\rangle \rightarrow |eg^u; -9/2, 9/2\rangle$ transition is absent due to its vanishing dipole matrix element at small magnetic fields. Inset: Level diagram at zero magnetic field. (B) Calculated detunings for transitions on singly and doubly occupied sites. The solid lines correspond to transitions on singly occupied (orange) and doubly occupied (red, blue) sites with $m_F = \pm 9/2$. Transitions on doubly occupied sites for arbitrary m_F and clock laser polarization lie within the shaded regions. At our operating magnetic field of 500 mG, all resonances for doubly occupied sites are well-resolved from the clock transitions.

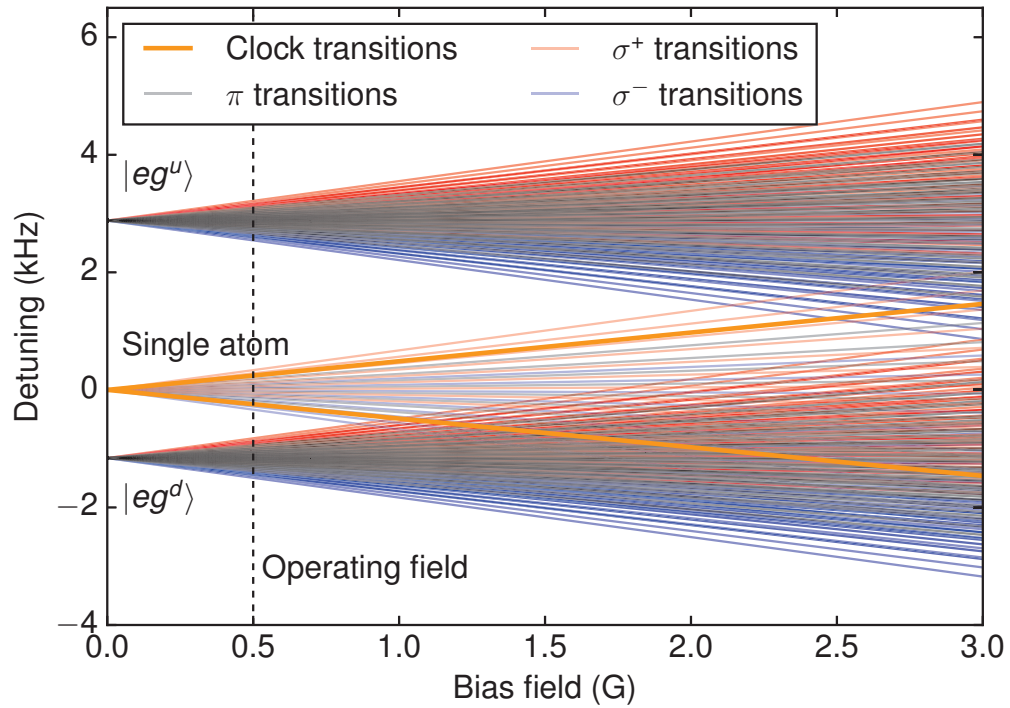


Figure 4.7: Detunings (relative to the unperturbed clock transition) for all transitions that can be driven on singly and doubly occupied lattice sites, shown for typical trap depths. Fig. 3B in the main text is a simplified version of this figure, with the shaded regions covering the range of all lines, and the solid lines showing the transition frequencies for only the states with $m_F = \pm 9/2$.

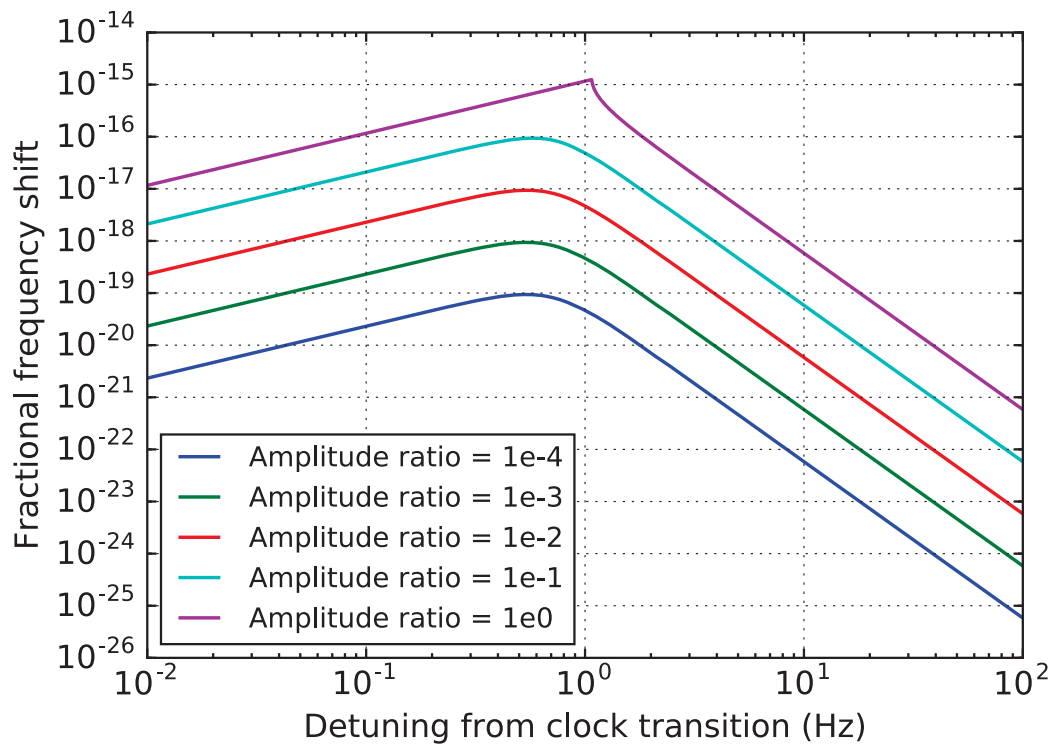


Figure 4.8: Systematic shifts due to line pulling from a residual line. Though the linewidth of the residual line will vary depending on what transition is being driven, we perform this calculation for 1 Hz linewidths to give a reasonable upper bound. The amplitude ratio indicates the amplitude of the residual line relative to that of the clock transition.

4.3 Narrow line spectroscopy

With atomic interactions and lattice ac Stark shifts controlled, we demonstrate a new record for narrow-line clock spectroscopy. Fig. 4.9 shows a progression of Ramsey fringes with free evolution times from 100 ms to 6 s, beyond what has been demonstrated in 1D lattice clocks [109, 121, 140]. Fig 4.10 shows 4 s Rabi spectroscopy at the Fourier limit, giving a linewidth of 190(20) mHz with full contrast. The \hat{x} lattice beam is operated at a depth sufficient ($>80E_{\text{rec}}$) to prevent atoms from tunneling along the clock laser axis during the 6 s free evolution period. Spectroscopy is performed on a spin-polarized sample, prepared by first exciting $|g; -9/2\rangle \rightarrow |e; -9/2\rangle$, then removing all ground state atoms via resonant $^1S_0 - ^1P_1$ light. Our longest observed coherence time approaches the limit of our clock laser based on its noise model [19] and the 12 s dead time between measurements. For the demonstration of Ramsey fringes at longer free-evolution times, maintaining atom-light phase coherence will require a significant reduction in fundamental thermal noise from the optical local oscillator. Additionally, the observation of narrower lines will require magnetic field control below the 100 μG level. The contrast of the observed Ramsey fringes is likely limited by lattice light causing both dephasing over the atomic sample and excited state population decay. Inhomogeneities are minimized for our smallest samples with an atom number of 1×10^4 and temperature of 15 nK.

Using Rabi spectroscopy with a 4 s pulse time, we measure a full-contrast Fourier-limited linewidth of 190(20) mHz, as shown in Fig. 4.10. This is different than spectroscopy in a 1D lattice, where clock scans at the longest probe times show substantially reduced contrast due to atomic contact interactions [109, 121].

4.4 Stability

The combination of large atom numbers with a long atom-light coherence time in this system opens the possibility for improving the quantum projection noise (QPN) limited clock stability by more than an order of magnitude over the current state-of-the-art [140]. The QPN limit for Ramsey

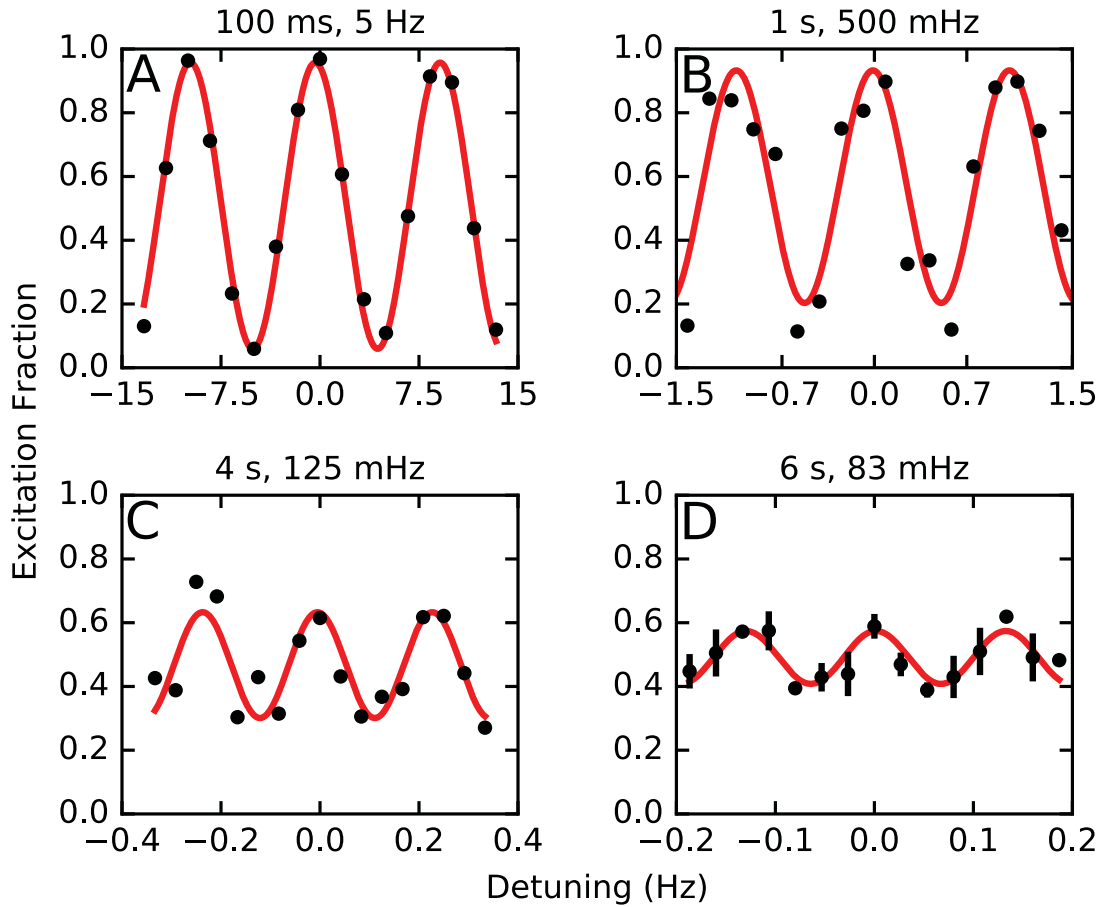


Figure 4.9: Ramsey spectroscopy data taken with 1×10^4 atoms at 15 nK for (A) 100 ms, (B) 1 s, (C) 4 s, and (D) 6 s free-evolution times, using 10 ms $\pi/2$ pulse times. With contact interactions and ac Stark shifts controlled in a 3D lattice, we are able to measure fringes at a record 6 s free-evolution time with a density of over 10^{13} atoms/cm³. The data shown in (D) is an average of two measurements, with 1σ error bars shown.

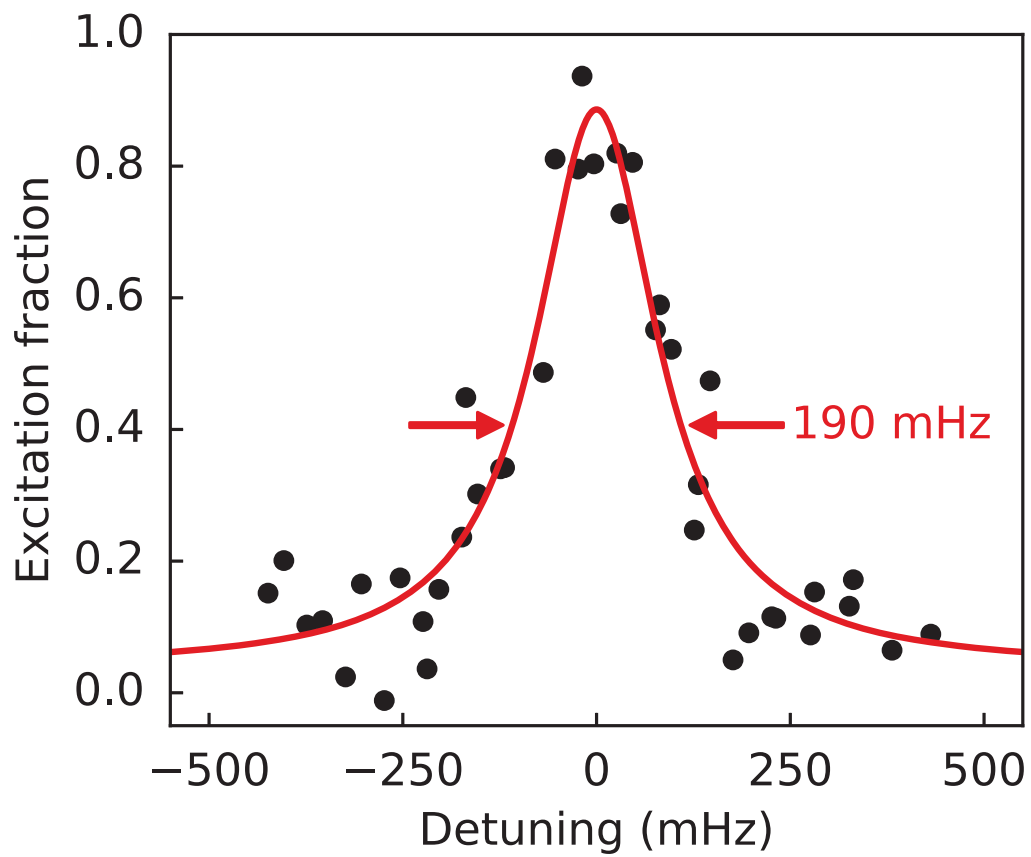


Figure 4.10: Rabi spectroscopy data for a 4 s π -pulse time, showing a 190(20) mHz Fourier-limited linewidth, taken with $m_F = 9/2$ and rescaled by the relative spin population.

spectroscopy can be given as,

$$\sigma_{\text{QPN}}(\tau) = \frac{1}{2\pi\nu T} \sqrt{\frac{T + T_d}{N\tau}}, \quad (4.14)$$

where ν is the clock frequency, T is the free-evolution time, T_d is the dead time, and τ is the total averaging time. Typically, OLCs operate at a stability above this limit due to the Dick effect [76]; however, operation at or near the QPN limit has been demonstrated in systems through synchronous interrogation of two clocks [122, 154] or interleaved interrogation of two clocks with zero dead time [140]. A synchronous comparison between two copies of our system would achieve a QPN-limited stability of $\sigma_{\text{QPN}}(\tau) \approx 3 \times 10^{-18}/\sqrt{\tau}$ for $T = 6$ s and $T_d = 12.7$ s, assuming perfect contrast. The current experimental contrast limits this stability to $1 \times 10^{-17}/\sqrt{\tau}$ (see Figure 4.9D). Our design can accommodate even greater atom numbers which, combined with improved preparation of degenerate gases and the next generation of ultra-stable lasers, should enable operation of a zero dead time clock below the $10^{-18}/\sqrt{\tau}$ level. Reaching such performance is extremely challenging for 1D OLCs as collisional effects force a compromise between interrogation time and the number of atoms that can be simultaneously interrogated [109, 121].

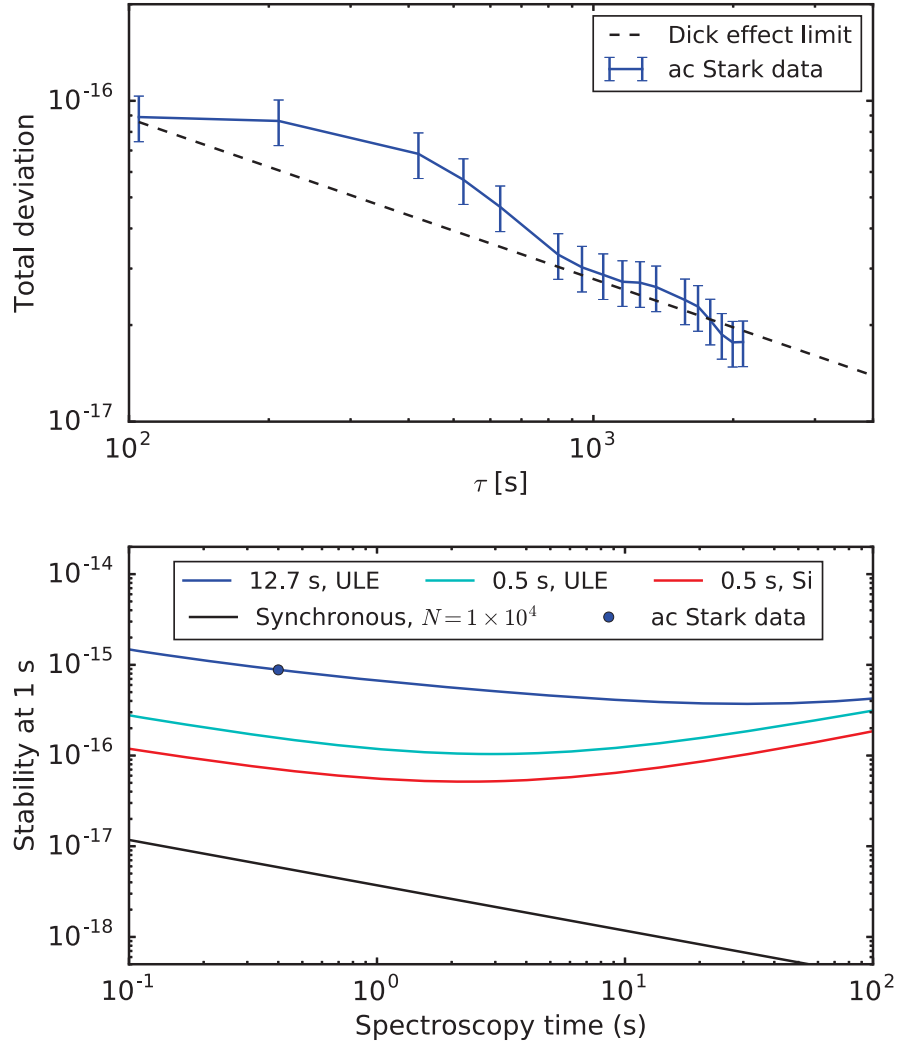


Figure 4.11: Measured and calculated stability for different clock configurations. Top: Total deviation of data (blue) from Fig. 3 divided by $\sqrt{2}$ to demonstrate single clock performance. The black dashed line represents the predicted Dick effect limit given the laser noise model [19] of our current cavity (ULE), a 12.7 s dead-time and a 0.4 s interrogation time, demonstrating that we understand the effects of laser noise on our clock stability. Bottom: Calculated stability at 1 second as a function of spectroscopy for various generations of clock lasers and dead times. Si represents our next generation ultra-stable laser [111]. The 12.7 second dead-time corresponds to that of our Fermi-degenerate 3D lattice clock while the 0.5 second dead-time corresponds to our previous generation 1D lattice clock [121]. The black line shows the QPN limit of our 3D lattice clock for 10^4 atoms.

Chapter 5

Future prospects and conclusion

Optical lattice clocks have now entered the quantum degenerate regime. With atoms that are frozen into a 3D cubic lattice, we have advanced the state-of-the-art in coherent atom-light interrogation times. Already, using synchronous comparisons, we have demonstrated an unprecedented stability of $3 \times 10^{-18}/\sqrt{7}$. Further improvements will be enabled by the next generations of ultra-stable optical reference cavities based on crystalline materials [86, 38]. The latest advances in the frequency references and local oscillators that together constitute atomic clocks will lead to a new era for clock performance, resulting in new measurement capabilities [92].

Quantum degenerate clocks also provide a promising platform for studying many-body physics. Future studies of dipolar interactions will not only be necessary for clock accuracy, but will also provide insight into long-range quantum spin systems in a regime distinct from those explored by polar molecules [167, 118], Rydberg gases [139, 95], and highly magnetic atoms [4, 45, 81, 29]. When clocks ultimately confront the natural linewidth of the atomic frequency reference, degenerate Fermi gases may be useful for engineering longer coherence times through Pauli blocking of spontaneous emission [136] or collective radiative effects [125, 93]. Ultracold quantum gases provide new capabilities for precision metrology.

5.0.1 Accuracy

Moving forward, we envision using high resolution imaging and spatially-pinned atoms in the 3D optical lattice to directly see systematic inhomogeneities. Whereas previously, we measured

systematic shifts via a self-comparison of alternating digital PID locks to alternating experimental conditions (e.g. high and low lattice intensities for measurement of the AC Stark effect), one can imagine combining high resolution imaging with long dark time Ramsey spectroscopy in order to perform a self-comparison within a single experimental cycle.

We could either trap each half of the cloud in a different experimental condition, or we could apply a linear gradient across the cloud. The systematic shift would then be determined from the relative phases inside atom cloud, and so the free evolution time could be much longer than the coherence time of the laser. This technique would remove laser noise entirely from the measurement of systematics, as well as increase the measurement Q factor far beyond that of the clock laser.

In this configuration, the statistical uncertainty for systematic measurements is only limited by the atoms' QPN which depends on the atom number N and atomic quality factor Q , thus providing further motivation for improving control and coherence time of the atomic reference component of the clock. This technique can improve clock accuracy whether or not laser noise from the Dick effect limits stability during normal operation. Here we discuss some outstanding systematics and how they might benefit from the capabilities of a quantum degenerate gas.

The most outstanding source of systematic uncertainty in OLCs is Stark shifts due to ambient blackbody radiation (BBR). Since the room-temperature BBR spectrum is largely in the infrared, while most of the transitions in Sr are optical, to first order, one can think of the BBR shift as a DC Stark shift which only depends on the total magnitude of the electric field. This is referred to as the “static BBR shift,” and it can be written as $\Delta\nu_{\text{static}}T^4$. Additionally, we apply a second-order correction known as the “dynamic BBR shift” ($\Delta\nu_{\text{dynamic}}T^6$) which depends on the frequency-dependent couplings of the various strontium transitions with the ambient BBR spectrum.

The strongest contributor to the dynamic BBR shift is the $2.6 \mu\text{m } ^3P_0$ to 3D_1 transition. To improve the uncertainty of the dynamic BBR strength in [121], we performed a better measurement of the 3D_1 lifetime to the 0.5% level in order to better constrain atomic structure calculations of $\Delta\nu_{\text{dynamic}}$, achieving a 1.4×10^{-18} fractional frequency uncertainty, limited by uncertainty in various experimentally-measured line strengths. The uncertainty can be further improved by a

better measurement of the 3D_1 lifetime, but only by a factor of 2 or so, before we would have to go and perform accurate measurements on *all* of the other coupling strengths.

A better strategy is to reduce the temperature T to reduce the contribution of uncertainty in $\Delta\nu_{\text{dynamic}}$. This can be accomplished using a cryogenic shield as in [157]. The difficulty with holding the atoms inside a shield with a different temperature, away from equilibrium with the outside world, is uncertainty introduced by both thermal gradients in the cryogenic shield and any open aperture used to shuttle the atoms inside. Ray-tracing models can be used to estimate these effects, but they are never as convincing as the direct clock measurements which are performed for nearly every other systematic. Cryogenic shielding will continue to be a challenging engineering problem for any group pursuing a 10^{-19} -level clock.

For example, one could imagine shuttling the 3D lattice into a cryogenic shield¹, performing a Ramsey sequence with a long dark time, and then imaging the spatial distribution of relative accumulated phases among the atomic references. Since an athermal BBR spectrum directly corresponds to a temperature gradient across the sample, this would allow us to directly measure the influence of, for example, room-temperature BBR leaking in through an aperture. These measurements would provide a direct check on the ray-tracing modeling, reducing uncertainty, and allowing me to sleep better at night.

The lattice AC Stark shift can also be measured via this method. We are already considering using digital micromirror arrays to engineer a 3D box potential for our lattice, it is not too much of a stretch to imagine using this technology to trap, for example, the left half of the cloud at a high lattice intensity, and the low half of the cloud at a low lattice intensity. As discussed earlier, the use of a Mott insulator will also allow us to run the clock at much lower lattice depths, and the uncertainty in our extrapolated shift would scale down accordingly.

A final example is that we could have half of our atoms be in the $m_F = -9/2$ state and the other half of the atoms in the $m_F = +9/2$ state. We could then apply a magnetic field gradient along a particular direction and for each magnetic field value, add the phases from the opposite

¹ Yes, this would be quite the engineering problem, but I would even say I could do it.

spin states. This would directly extract the quadratic Zeeman shift as a function of magnetic field.

5.1 Dark matter searches

“Those years, when the Lamb shift was the central theme of physics, were golden years for all the physicists of my generation. You were the first to see that this tiny shift, so elusive and hard to measure, would clarify our thinking about particles and fields.”

-Freeman Dyson, speaking to Willis Lamb on his 65th birthday[143]

Our innate desire to continue looking closer and closer is further fueled by the fact that we are far from figuring everything out. The Standard Model (SM) of particle physics explains only 5% of the mass-energy content of the universe. Another 27% of the universe is comprised of dark matter, which until recently was postulated to have a mass on the TeV/c^2 scale and only couple to the weak force. However, the Large Hadron Collider and direct detection experiments have so far failed to detect these weakly interacting massive particles, thus inspiring more searches in different parameter regimes. Furthermore, the increasing costs and technical challenges with each decade of particle accelerator energy motivate the need for new approaches to explore beyond SM physics. From astrophysical measurements, we know that DM in our Milky Way has an energy density ρ_{DM} of $0.3 \text{ GeV}/\text{cm}^3$ and a mean virial velocity V_{vir} of $10^{-3}c$ with a variance of similar order. Structure formation in the early universe puts a $1 \times 10^{-22} \text{ eV}/c^2$ lower bound on the DM rest mass m_{DM} [108]. Fermionic DM must have a rest mass greater than $1 \text{ keV}/c^2$, as Pauli exclusion prohibits lighter particles from reaching the required density. In contrast, bosonic DM allows for m_{DM} below $1 \text{ eV}/c^2$ at high phase space density. In this case, the DM is a Bose condensate with amplitude and frequency $m_{\text{DM}}c^2/h$, where h is the Planck constant [12]. The wave follows the scalar equation (in dimensionless units),

$$\phi(t, \vec{x}) = \phi_0 \cos \left(m_{\text{DM}}t - \vec{k}_\phi \times \vec{x} + \dots \right). \quad (5.1)$$

The spread in kinetic energy $\approx m_{\text{DM}}v_{\text{vir}}^2$ around the rest mass energy $m_{\text{DM}}c^2$ sets a quality factor Q for dark matter oscillations of 10^6 , corresponding to a coherence time τ_{coh} of $10^6 h/(m_{\text{DM}}c^2)$.

Improvements in precise atomic tests can search for ultralight dark matter oscillations at the 1 mHz, 1 Hz, or 1 kHz scale, corresponding to m_{DM} of $4 \times 10^{-18} \text{eV}/c^2$, $4 \times 10^{-15} \text{eV}/c^2$ and $4 \times 10^{-12} \text{eV}/c^2$, and coh of 30 years, 10 days, and 20 minutes, respectively. Candidates for ultralight DM particles include the axion [126], motivated by QCD, and the dilaton, as motivated by string theory. The dilaton is predicted by all versions of string theory as a scalar partner of the tensor Einstein graviton [42, 52]. Light scalar fields from extra dimensions offer a solution for the so-called hierarchy problem, wherein the SM offers no explanation for discrepancies in gauge coupling parameters for the fundamental forces, the most outstanding of which is the puzzle as to why the weak force is 10^{24} times stronger than gravity [11, 72]. The dilaton could be detected via possible scalar couplings d_i to the four fundamental forces of the SM, which cause oscillatory perturbations to the effective masses and gauge couplings of fundamental particles [43]. In particular, the electromagnetic coupling term d_e would lead the field ϕ to cause coherent oscillations in the fine structure constant α according to,

$$\frac{\partial \ln \alpha}{\partial(\kappa\phi)} = d_e, \quad (5.2)$$

where the field is normalized to the Planck mass M_{Pl} using $\kappa = M_{\text{Pl}}/\sqrt{4\pi}$. Additionally, the gluonic, quark mass, and electron mass coupling terms can also cause variations in the proton-to-electron mass ratio m_p/m_e . The frequencies f_A of atomic transitions scale with m_p/m_e and α as,

$$f_A \propto \left(\frac{m_e}{m_p}\right)^{\xi_A} \alpha^{\xi_A+2}, \quad (5.3)$$

where $\xi_A = 1$ for hyperfine transitions and $\xi_A = 0$ for optical transitions [12]. The variable ξ_A depends on the properties of the atom and is listed for common atomic frequency references in [98]. Until recently, equivalence principle (EP) tests such as lunar laser ranging [162, 163] and the Eöt-Wash experiment [141] placed the best constraints on various dilaton couplings, including $|d_e| \leq 3.6 \times 10^{-4}$ for all dilaton masses (or equivalently, oscillation frequencies). However, following the proposal in [12], spectroscopy data for two isotopes of dysprosium was analyzed in [158] to further explore parameter space, improving limits on $|d_e|$ to below the 1×10^{-7} level for masses in

the $1 \times 10^{-22} \text{eV}/c^2$ range. The work in [67] used 6 years of comparison data between the hyperfine clock transitions in Rb and Cs, which, in addition to putting improved limits on $|d_e|$ at low mass, was also sensitive to variations in quark mass and the quantum chromodynamic mass scale. There is great room for improvement on searches for ultralight DM taking advantage of state-of-the-art optical clocks and ultrastable reference cavities [148]. A direct frequency comparison of the JILA strontium optical lattice clock with a laser referenced to a cryogenic silicon cavity is linearly sensitive to variations in α and therefore is sensitive to perturbations from ultralight DM. This experiment will be sensitive to oscillations in the mHz to kHz frequency range ($10^{-19} \text{eV}/c^2$ to $10^{-12} \text{eV}/c^2$ mass scale), with the capability to measure Planck-scale coupling in one second and surpass limits from EP tests after one week of averaging. Experiments using next-generation cavities with crystalline spacers, substrates, and mirror coatings will be able to reach this limit within a few hours. Synchronous clock comparisons between the JILA strontium clock and NIST ytterbium clock can improve limits on $|d_e|$ over a wide mass range, including lower masses approaching $10^{-22} \text{eV}/c^2$.

The better we make our atomic clocks, the more sensitive they will be to measuring new particles. Furthermore, better stability not only allows for shorter averaging times or lower uncertainties, it also enables the detection of transients.

5.2 The future of quantum metrology

“The simplest prototype of emergent exactness, however, is the regularity of crystal lattices, the effect ultimately responsible for solid rigidity. The atomic order of crystals can be perfect on breathtakingly long scales in very good samples, as many as one hundred million atomic spacings.”

- Robert Laughlin, A Different Universe: Reinventing Physics From the Bottom Down

We discover new physical laws and make deeper connections by traveling to new places and parameter regimes. Measurement precision is a dimension of exploration unto itself. For the journey to continue, we must anticipate and overcome future limitations. The major impediments to measurement precision are shot noise, decoherence, and uncontrolled systematics.

Great strides have already been made to tackle the first two issues, as quantum correlations can both move errors outside of the measurement basis and enhance the maintenance of an out-of-equilibrium state. Spin squeezing via the collective interaction of an atomic ensemble with a mode of an electromagnetic field in a cavity has been used to redistribute the quantum noise between different degrees of freedom by entangling the atoms in the ensemble [117]. This has been used to overcome the Standard Quantum Limit, where measurement noise scales with the particle number N as $1/\sqrt{N}$, to make progress towards the Heisenberg limit where noise scales as $1/N$. However, to this day nobody has yet demonstrated spin squeezing at sufficiently long time scales to truly improve the state-of-the-art in frequency metrology. This is a great and fun challenge to tackle in the near future.

Many-body synchronization has been studied in the context of superradiance [50] and driven time crystals that prevent thermalization [170, 35]. Superradiant lasers in particular can overcome the noise from the optical cavity and may well be the future of ultrastable lasers [114, 24, 124, 123]. To protect against both decoherence and quantum noise, quantum error correction schemes store the information from one qubit among several highly-entangled qubits.

While improvements in short-term stability increase both overall sensitivity and bandwidth

for the detection of transients, uncontrolled systematic shifts present a separate, albeit related, challenge in precision measurement. When developing tools such as atomic clocks, accuracy and precision turn out to be two sides of the same coin. Nature provides fundamental constants that are either not changing or changing so slowly that we cannot tell, and so we use them to reference our measurement devices to minimize long-term drift, which is equivalent to low-frequency noise. Something that does not drift over time has no limit to how well it can be known. More data always improves the error bars. However, every real-world Allan deviation turns up at some point. Atomic transition frequencies are, in principle, constants of nature, but in practice they fluctuate within the bounds of our ability to mitigate and account for environmental perturbations. Even our “perfect” atomic reference is a source of noise which is not guaranteed to average down beyond its accuracy.

We demonstrate first successful use of a quantum many-body system (a Mott insulator) to essentially eliminate a systematic effect (collisional shifts) in an atomic clock. We anticipate that we will soon be able to make a band insulator and run at much lower trap depths which will also reduce the lattice AC Stark shift. This opens up a new approach to clock accuracy. Instead of measuring and stabilizing every systematic effect, we can engineer quantum many-body states that are immune to them.

This inspires us to take another look inside our quantum toolbox and see how far we can take the ideas of quantum entanglement, emergent behavior, and topological matter towards protecting our clock against systematic errors. The idea would be to engineer a synthetic atomic transition that is not susceptible to the usual systematics. One could think of entangling two ensembles of different atoms with different sensitivities to various environmental perturbations. Perhaps the synthetic atomic transition would need to be entangled with and provide feedback to the environment. One starting point could be systematics which couple to another observable, so we could extract an error signal by other means than direct measurement on the clock transition. Inspired by the decoherence-free subspaces employed in quantum error correction, I wonder if one can engineer a system which has an “error-free subspace” which is immune to errors in DC values of clock transition

frequencies. Another idea is that we can engineer large energy gaps for systematics (similar to what we have already shown for clock transitions for doublons), so that they are energetically forbidden from befouling the clock transition.

For example, differential lattice AC stark shifts coming from the differential polarizability between the ground and clock states cause the atoms position and motion to become entangled with its electronic state. Could a cavity QED system provide some mechanism for detection and amplification of this differential atomic motion? Can shifts be canceled via quantum feedback? A quantum many-body frequency reference that never decoheres and uses quantum feedback to eliminate all systematics may be a pipe dream, but then again, we do live in Boulder.

When logic and proportion

Have fallen sloppy dead

And the White Knight is talking backwards

And the Red Queen's off with her head

Remember what the dormouse said

Feed your head

Feed your head

- Jefferson Airplane, White Rabbit

Bibliography

- [1] Base unit definitions: Meter, <http://physics.nist.gov/cuu/Units/meter.html>.
- [2] Fraunhofer lines, https://upload.wikimedia.org/wikipedia/commons/2/2f/fraunhofer_lines.svg.
- [3] International System of Units (SI). International Bureau of Weights and Measures (BIPM), 8 edition, 2008.
- [4] K. Aikawa, S. Baier, A. Frisch, M. Mark, C. Ravensbergen, and F. Ferlaino. Observation of Fermi surface deformation in a dipolar quantum gas. Science, 345(6203), 2014.
- [5] Tomoya Akatsuka, Masao Takamoto, and Hidetoshi Katori. Three-dimensional optical lattice clock with bosonic Sr88 atoms. Physical Review A - Atomic, Molecular, and Optical Physics, 81(2), 2010.
- [6] Fangzhao Alex An, Eric J. Meier, and Bryce Gadway. Direct observation of chiral currents and magnetic reflection in atomic flux lattices. 9 2016.
- [7] M. H. Anderson, J. R. Ensher, M. R. Matthews, C. E. Wieman, and E. A. Cornell. Observation of Bose-Einstein Condensation in a Dilute Atomic Vapor. Science, 269(5221):198–201, 7 1995.
- [8] Rene Andrae. Error estimation in astronomy: A guide. <http://arxiv.org/abs/1009.2755>. 2010.
- [9] Andrew D. Ludlow. The Strontium Optical Lattice Clock: Optical Spectroscopy with Sub-Hertz Accuracy. PhD thesis, University of Colorado, 2008.
- [10] Ariel T. Sommer. Strongly Interacting Fermi Gases: Non-Equilibrium Dynamics and Dimensional Crossover. PhD thesis, MIT, 2013.
- [11] Nima Arkani-Hamed, Lawrence Hall, David Smith, and Neal Weiner. Solving the hierarchy problem with exponentially large dimensions. Physical Review D, 62(10):105002, 10 2000.
- [12] Asimina Arvanitaki, Junwu Huang, and Ken Van Tilburg. Searching for dilaton dark matter with atomic clocks. Physical Review D, 91(1):015015, 1 2015.
- [13] W. David Kelton Averill M. Law. Simulation Modelling and Analysis. McGraw Hill Higher Education, 3 edition, 2000.
- [14] Aviv Keshet. A Next-Generation Apparatus for Lithium Optical Lattice Experiments. PhD thesis, MIT, 2012.

- [15] D. Banerjee, M. Bögli, M. Dalmonte, E. Rico, P. Stebler, U.-J. Wiese, and P. Zoller. Atomic Quantum Simulation of $U(N)$ and $SU(N)$ Non-Abelian Lattice Gauge Theories. Physical Review Letters, 110(12):125303, 3 2013.
- [16] M. Bartenstein, A. Altmeyer, S. Riedl, R. Geursen, S. Jochim, C. Chin, J. Hecker Denschlag, R. Grimm, A. Simoni, E. Tiesinga, C. J. Williams, and P. S. Julienne. Precise Determination of Li 6 Cold Collision Parameters by Radio-Frequency Spectroscopy on Weakly Bound Molecules. Physical Review Letters, 94(10):103201, 3 2005.
- [17] K. Beloy, N. Hinkley, N.B. Phillips, J.A. Sherman, M. Schioppo, J. Lehman, A. Feldman, L.M. Hanssen, C.W. Oates, and A.D. Ludlow. Atomic Clock with $1 \cdot 10^{-18}$ Room-Temperature Blackbody Stark Uncertainty. Physical Review Letters, 113(26):260801, 12 2014.
- [18] M. Bishof, M. J. Martin, M. D. Swallows, C. Benko, Y. Lin, G. Quéméner, A. M. Rey, and J. Ye. Inelastic collisions and density-dependent excitation suppression in a 87 Sr optical lattice clock. Physical Review A, 84(5):052716, 11 2011.
- [19] M. Bishof, X. Zhang, M. J. Martin, and Jun Ye. Optical Spectrum Analyzer with Quantum-Limited Noise Floor. Physical Review Letters, 111(9):093604, 8 2013.
- [20] S. Blatt, J. W. Thomsen, G. K. Campbell, A. D. Ludlow, M. D. Swallows, M. J. Martin, M. M. Boyd, and J. Ye. Rabi spectroscopy and excitation inhomogeneity in a one-dimensional optical lattice clock. Physical Review A, 80(5):052703, 11 2009.
- [21] Immanuel Bloch. Ultracold quantum gases in optical lattices. Nature Physics, 1(1):23–30, 10 2005.
- [22] Immanuel Bloch, Jean Dalibard, and Wilhelm Zwerger. Many-body physics with ultracold gases. Reviews of Modern Physics, 80(3):885–964, 7 2008.
- [23] B J Bloom, T L Nicholson, J R Williams, S L Campbell, M Bishof, X Zhang, W Zhang, S L Bromley, and J Ye. An optical lattice clock with accuracy and stability at the 10^{-18} level. Nature, 506(7486):71–75, 2014.
- [24] Justin G. Bohnet, Zilong Chen, Joshua M. Weiner, Dominic Meiser, Murray J. Holland, and James K. Thompson. A steady-state superradiant laser with less than one intracavity photon. Nature, 484(7392):78–81, 4 2012.
- [25] Martin M. Boyd, Tanya Zelevinsky, Andrew D. Ludlow, Sebastian Blatt, Thomas Zanon-Willette, Seth M. Foreman, and Jun Ye. Nuclear spin effects in optical lattice clocks. Physical Review A, 76(2):022510, 8 2007.
- [26] Martin M. Boyd, Tanya Zelevinsky, Andrew D. Ludlow, Seth M. Foreman, Sebastian Blatt, Tetsuya Ido, and Jun Ye. Optical Atomic Coherence at the 1-Second Time Scale. Science, 314(5804), 2006.
- [27] John C. D. Brand. Lines of Light: The Sources of Dispersive Spectroscopy, 1800 - 1930. Gordon and Breach Publishers, 1995.
- [28] S. L. Bromley, B. Zhu, M. Bishof, X. Zhang, T. Bothwell, J. Schachenmayer, T. L. Nicholson, R. Kaiser, S. F. Yelin, M. D. Lukin, A. M. Rey, and J. Ye. Collective atomic scattering and motional effects in a dense coherent medium. Nature Communications, 7:11039, 3 2016.

- [29] Nathaniel Q. Burdick, Yijun Tang, and Benjamin L. Lev. Long-Lived Spin-Orbit-Coupled Degenerate Dipolar Fermi Gas. Physical Review X, 6(3):031022, 8 2016.
- [30] G. K. Campbell, M. M. Boyd, J. W. Thomsen, M. J. Martin, S. Blatt, M. D. Swallows, T. L. Nicholson, T. Fortier, C. W. Oates, S. A. Diddams, N. D. Lemke, P. Naidon, P. Julienne, Jun Ye, and A. D. Ludlow. Probing Interactions Between Ultracold Fermions. Science, 324(5925), 2009.
- [31] G. Cappellini, M. Mancini, G. Pagano, P. Lombardi, L. Livi, M. Siciliani de Cumis, P. Cancio, M. Pizzocaro, D. Calonico, F. Levi, C. Sias, J. Catani, M. Inguscio, and L. Fallani. Direct Observation of Coherent Interorbital Spin-Exchange Dynamics. Physical Review Letters, 113(12):120402, 9 2014.
- [32] D. E. Chang, Jun Ye, and M. D. Lukin. Controlling dipole-dipole frequency shifts in a lattice-based optical atomic clock. Physical Review A, 69(2):023810, 2004.
- [33] Cheng-Hsun Wu. Strongly Interacting Quantum Mixtures of Ultracold Atoms. PhD thesis, MIT, 2013.
- [34] Cheng Chin, Rudolf Grimm, Paul Julienne, and Eite Tiesinga. Feshbach resonances in ultracold gases. Reviews of Modern Physics, 82(2):1225–1286, 4 2010.
- [35] Soonwon Choi, Joonhee Choi, Renate Landig, Georg Kucsko, Hengyun Zhou, Junichi Isoya, Fedor Jelezko, Shinobu Onoda, Hitoshi Sumiya, Vedika Khemani, Curt von Keyserlingk, Norman Y. Yao, Eugene Demler, and Mikhail D. Lukin. Observation of discrete time-crystalline order in a disordered dipolar many-body system. Nature, 543(7644):221–225, 3 2017.
- [36] Claude Cohen-Tannoudji. Manipulating Atoms with Photons. In Nobel Lectures, Physics 1996-2000. World Scientific Publishing Co., Singapore, 2002.
- [37] Eugenio Cocchi, Luke A. Miller, Jan H. Drewes, Marco Koschorreck, Daniel Pertot, Ferdinand Brennecke, and Michael Köhl. Equation of State of the Two-Dimensional Hubbard Model. Physical Review Letters, 116(17):175301, 4 2016.
- [38] G D Cole, W Zhang, M J Martin, J Ye, and M Aspelmeyer. Tenfold reduction of Brownian noise in high-reflectivity optical coatings. Nature Photonics, 7(8):644–650, 2013.
- [39] N. R. Cooper. Optical Flux Lattices for Ultracold Atomic Gases. Physical Review Letters, 106(17):175301, 4 2011.
- [40] E. A. Cornell and C. E. Wieman. Nobel Lecture: Bose-Einstein condensation in a dilute gas, the first 70 years and some recent experiments. Reviews of Modern Physics, 74(3):875–893, 8 2002.
- [41] CVI Melles Griot. Fundamental Optics. CVI Melles Griot 2009 Technical Guide, 2(1).
- [42] T. Damour and A.M. Polyakov. The string dilation and a least coupling principle. Nuclear Physics B, 423(2):532–558, 1994.
- [43] Thibault Damour and John F. Donoghue. Equivalence principle violations and couplings of a light dilaton. Physical Review D, 82(8):084033, 10 2010.

- [44] K. B. Davis, M. O. Mewes, M. R. Andrews, N. J. van Druten, D. S. Durfee, D. M. Kurn, and W. Ketterle. Bose-Einstein Condensation in a Gas of Sodium Atoms. Physical Review Letters, 75(22):3969–3973, 11 1995.
- [45] A. de Paz, P. Pedri, A. Sharma, M. Efremov, B. Naylor, O. Gorceix, E. Maréchal, L. Vernac, and B. Laburthe-Tolra. Probing spin dynamics from the Mott insulating to the superfluid regime in a dipolar lattice gas. Physical Review A, 93(2):021603, 2 2016.
- [46] B DeMarco. Onset of Fermi Degeneracy in a Trapped Atomic Gas. Science, 285(5434):1703–1706, 1999.
- [47] A. Derevianko and M. Pospelov. Hunting for topological dark matter with atomicclocks. Nature Physics, 10(12):933–936, 11 2014.
- [48] B. J. DeSalvo, M. Yan, P. G. Mickelson, Y. N. Martinez de Escobar, and T. C. Killian. Degenerate Fermi Gas of Sr 87. Physical Review Letters, 105(3):030402, 7 2010.
- [49] Jean-Daniel Deschênes, Laura C. Sinclair, Fabrizio R. Giorgetta, William C. Swann, Esther Baumann, Hugo Bergeron, Michael Cermak, Ian Coddington, and Nathan R. Newbury. Synchronization of Distant Optical Clocks at the Femtosecond Level. Physical Review X, 6(2):021016, 5 2016.
- [50] R. H. Dicke. Coherence in Spontaneous Radiation Processes. Physical Review, 93(1):99–110, 1 1954.
- [51] Scott A. Diddams, David J. Jones, Jun Ye, Steven T. Cundiff, John L. Hall, Jinendra K. Ranka, Robert S. Windeler, Ronald Holzwarth, Thomas Udem, and T. W. Hänsch. Direct Link between Microwave and Optical Frequencies with a 300 THz Femtosecond Laser Comb. Physical Review Letters, 84(22):5102–5105, 5 2000.
- [52] S. Dimopoulos and G.F. Giudice. Macroscopic forces from supersymmetry. Physics Letters B, 379(1-4):105–114, 6 1996.
- [53] W. B. Dress, P. D. Miller, J. M. Pendlebury, Paul Perrin, and Norman F. Ramsey. Search for an electric dipole moment of the neutron. Physical Review D, 15(1):9–21, 1 1977.
- [54] Albert Einstein. Concerning an Heuristic Point of View Toward the Emission and Transformation of Light. Annalen der Physik, 17:132–148, 1905.
- [55] Albert Einstein and Albert. Zur Quantentheorie der Strahlung. Physikalische Zeitschrift, Band 18, Seite 121-128., 18, 1917.
- [56] Stephan Falke, Nathan Lemke, Christian Grebing, Burghard Lipphardt, Stefan Weyers, Vladislav Gerginov, Nils Huntemann, Christian Hagemann, Ali Al-Masoudi, Sebastian Höfner, Stefan Vogt, Uwe Sterr, and Christian Lisdat. A strontium lattice clock with 3×10^{-17} inaccuracy and its frequency. New Journal of Physics, 16, 2014.
- [57] Richard P. Feynman. Simulating physics with computers. International Journal of Theoretical Physics, 21(6-7):467–488, 6 1982.
- [58] Michael Foss-Feig, Michael Hermele, and Ana Maria Rey. Probing the Kondo lattice model with alkaline-earth-metal atoms. Physical Review A, 81(5):051603, 5 2010.

- [59] Michael H. Freedman, Alexei Kitaev, Michael J. Larsen, and Zhenghan Wang. Topological quantum computation. Bulletin of the American Mathematical Society, 40(01):31–39, 10 2002.
- [60] J. P. Gordon, H. J. Zeiger, and C. H. Townes. The Maser: New Type of Microwave Amplifier, Frequency Standard, and Spectrometer. Physical Review, 99(4):1264–1274, 8 1955.
- [61] A. V. Gorshkov, M. Hermele, V. Gurarie, C. Xu, P. S. Julienne, J. Ye, P. Zoller, E. Demler, M. D. Lukin, and A. M. Rey. Two-orbital SU(N) magnetism with ultracold alkaline-earth atoms. Nature Physics, 6(4):289–295, 4 2010.
- [62] Christian Grebing, Ali Al-Masoudi, Sren Dörscher, Sebastian Häfner, Vladislav Gerginov, Stefan Weyers, Burghard Lipphardt, Fritz Riehle, Uwe Sterr, and Christian Lisdat. Realization of a timescale with an accurate optical lattice clock. Optica, 3(6):563, 6 2016.
- [63] Markus Greiner, Olaf Mandel, Tilman Esslinger, Theodor W. Hänsch, and Immanuel Bloch. Quantum phase transition from a superfluid to a Mott insulator in a gas of ultracold atoms. Nature, 415(6867):39–44, 1 2002.
- [64] T. W. Lynn, H. Mabuchi, D. W. Vernooy, J. Ye, H. J. Kimble, C. J. Hood. Title. In D. R. Blatt, J. Eschner and F. Schmidt-Kaler Leibfried, editors, Proceedings of the XIV International Conference on Laser Spectroscopy, Innsbruck, 2009. World Scientific.
- [65] J.L. Hall. Optical frequency measurement: 40 years of technology revolutions. IEEE Journal of Selected Topics in Quantum Electronics, 6(6):1136–1144, 11 2000.
- [66] Serge Haroche. Nobel Lecture: Controlling photons in a box and exploring the quantum to classical boundary. Reviews of Modern Physics, 85(3):1083–1102, 7 2013.
- [67] A. Hees, J. Guéna, M. Abgrall, S. Bize, and P. Wolf. Searching for an Oscillating Massive Scalar Field as a Dark Matter Candidate Using Atomic Hyperfine Frequency Comparisons. Physical Review Letters, 117(6):061301, 8 2016.
- [68] Michael Hermele, Victor Gurarie, and Ana Maria Rey. Mott Insulators of Ultracold Fermionic Alkaline Earth Atoms: Underconstrained Magnetism and Chiral Spin Liquid. Physical Review Letters, 103(13):135301, 9 2009.
- [69] H. Hertz. Ueber einen Einfluss des ultravioletten Lichtes auf die electrische Entladung. Annalen der Physik und Chemie, 267(8):983–1000, 1887.
- [70] N. Hinkley, J. A. Sherman, N. B. Phillips, M. Schioppo, N. D. Lemke, K. Beloy, M. Pizzocaro, C. W. Oates, and A. D. Ludlow. An Atomic Clock with 10^{18} Instability. Science, 341(6151):1215–1218, 2013.
- [71] M. Höfer, L. Riegger, F. Scazza, C. Hofrichter, D. R. Fernandes, M. M. Parish, J. Levinsen, I. Bloch, and S. Fölling. Observation of an Orbital Interaction-Induced Feshbach Resonance in Yb 173. Physical Review Letters, 115(26), 2015.
- [72] Lam Hui, Jeremiah P. Ostriker, Scott Tremaine, and Edward Witten. Ultralight scalars as cosmological dark matter. Physical Review D, 95(4):043541, 2 2017.

- [73] N. Huntemann, C. Sanner, B. Lipphardt, Chr. Tamm, and E. Peik. Single-Ion Atomic Clock with 3×10^{-18} Systematic Uncertainty. Physical Review Letters, 116(6):063001, 2 2016.
- [74] S. Inouye, M. R. Andrews, J. Stenger, H.-J. Miesner, D. M. Stamper-Kurn, and W. Ketterle. Observation of Feshbach resonances in a Bose-Einstein condensate. Nature, 392(6672):151–154, 3 1998.
- [75] S. Inouye, J. Goldwin, M. L. Olsen, C. Ticknor, J. L. Bohn, and D. S. Jin. Observation of Heteronuclear Feshbach Resonances in a Mixture of Bosons and Fermions. Physical Review Letters, 93(18):183201, 10 2004.
- [76] J. G. Dick. Local oscillator induced instabilities in trapped ion frequency standards. In Proc 19th Precise Time Time Interval Meet., pages 133–147, 1987.
- [77] S. R. Jefferts, J. Shirley, T. E. Parker, T. P. Heavner, D. M. Meekhof, C. Nelson, F. Levi, G. Costanzo, A. De Marchi, R. Drullinger, L. Hollberg, W. D. Lee, and F. L. Walls. Accuracy evaluation of NIST-F1. Metrologia, 39(4):321–336, 2003.
- [78] J.J. Thomson. Cathode Rays. The Electrician, 39(104), 1987.
- [79] Johann Jacob Balmer. Note on the Spectral Lines of Hydrogen. Annalen der Physik und Chemie, 25(80-5), 1995.
- [80] R Jordens, N Strohmaier, K Gunter, H Moritz, and Tilman Esslinger. A Mott insulator of fermionic atoms in an optical lattice. Nature, 455(7210):204–207, 2008.
- [81] Holger Kadau, Matthias Schmitt, Matthias Wenzel, Clarissa Wink, Thomas Maier, Igor Ferrier-Barbut, and Tilman Pfau. Observing the Rosensweig instability of a quantum ferrofluid. Nature, 530(7589):194–197, 2 2016.
- [82] P. L. Kapitza and P. A. M. Dirac. The reflection of electrons from standing light waves. Mathematical Proceedings of the Cambridge Philosophical Society, 29(02):297, 5 1933.
- [83] Hidetoshi Katori, Tetsuya Ido, and Makoto Kuwata-Gonokami. Optimal Design of Dipole Potentials for Efficient Loading of Sr Atoms. Journal of the Physical Society of Japan, 68(8):2479–2482, 8 1999.
- [84] Hidetoshi Katori, Masao Takamoto, Tomoya Akatsuka, and Hidekazu Hachisu. Optical lattice clocks with non-interacting bosons and fermions. In 2008 IEEE International Frequency Control Symposium, FCS, pages 58–64, 2008.
- [85] T. Kessler, C. Hagemann, C. Grebing, T. Legero, U. Sterr, F. Riehle, M. J. Martin, L. Chen, and J. Ye. A sub-40-mHz-linewidth laser based on a silicon single-crystal optical cavity. Nature Photonics, 6(10):687–692, 9 2012.
- [86] Thomas Kessler, Christian Hagemann, C. Grebing, T. Legero, Uwe Sterr, Fritz Riehle, M. J. Martin, L. Chen, and Jun Ye. A sub-40-mHz-linewidth laser based on a silicon single-crystal optical cavity. Nature Photonics, 6(10):687–692, 2012.
- [87] Wolfgang Ketterle. Nobel lecture: When atoms behave as waves: Bose-Einstein condensation and the atom laser. Reviews of Modern Physics, 74(4):1131–1151, 11 2002.

- [88] G. Kirchhoff and R. Bunsen. Chemische Analyse durch Spectralbeobachtungen. Annalen der Physik und Chemie, 186(6):161–189, 1860.
- [89] A.Yu. Kitaev. Fault-tolerant quantum computation by anyons. Annals of Physics, 303(1):2–30, 2003.
- [90] Michael Köhl. Thermometry of fermionic atoms in an optical lattice. Physical Review A, 73(3):031601, 3 2006.
- [91] S. Kolkowitz, S. L. Bromley, T. Bothwell, M. L. Wall, G. E. Marti, A. P. Koller, X. Zhang, A. M. Rey, and J. Ye. Spinorbit-coupled fermions in an optical lattice clock. Nature, 542(7639):66–70, 12 2016.
- [92] S. Kolkowitz, I. Pikovski, N. Langellier, M.D. Lukin, R.L. Walsworth, and J. Ye. Gravitational wave detection with optical lattice atomic clocks. Physical Review D, 94(12):124043, 12 2016.
- [93] Sebastian Krämer, Laurin Ostermann, and Helmut Ritsch. Optimized geometries for future generation optical lattice clocks. 1506.09079, (1):1–5, 2015.
- [94] M. J. H. Ku, A. T. Sommer, L. W. Cheuk, and M. W. Zwierlein. Revealing the Superfluid Lambda Transition in the Universal Thermodynamics of a Unitary Fermi Gas. Science, 335(6068):563–567, 2 2012.
- [95] Henning Labuhn, Daniel Barredo, Sylvain Ravets, Sylvain de Léséleuc, Tommaso Macrì, Thierry Lahaye, and Antoine Browaeys. Tunable two-dimensional arrays of single Rydberg atoms for realizing quantum Ising models. Nature, 534(7609):667–670, 6 2016.
- [96] Willis E. Lamb and Robert C. Retherford. Fine Structure of the Hydrogen Atom by a Microwave Method. Physical Review, 72(3):241–243, 8 1947.
- [97] Shau-Yu Lan, Pei-Chen Kuan, Brian Estey, Damon English, Justin M. Brown, Michael A. Hohensee, and Holger Müller. A Clock Directly Linking Time to a Particle’s Mass. Science, 339(6119), 2013.
- [98] S. N. Lea. Limits to time variation of fundamental constants from comparisons of atomic frequency standards. The European Physical Journal Special Topics, 163(1):37–53, 10 2008.
- [99] N. D. Lemke, J. vonStecker, J. A. Sherman, A. M. Rey, C. W. Oates, and A. D. Ludlow. p-Wave Cold Collisions in an Optical Lattice Clock. Physical Review Letters, 107(10):103902, 8 2011.
- [100] Pierre Lemonde and Peter Wolf. Optical lattice clock with atoms confined in a shallow trap. Physical Review A, 72(3):033409, 9 2005.
- [101] C. Lisdat, G. Grosche, N. Quintin, C. Shi, S.M.F. Raupach, C. Grebing, D. Nicolodi, F. Stefani, A. Al-Masoudi, S. Dörscher, S. Häfner, J.-L. Robyr, N. Chiodo, S. Bilicki, E. Bookjans, A. Koczwara, S. Koke, A. Kuhl, F. Wiotte, F. Meynadier, E. Camisard, M. Abgrall, M. Lours, T. Legero, H. Schnatz, U. Sterr, H. Denker, C. Chardonnet, Y. Le Coq, G. Santarelli, A. Amy-Klein, R. Le Targat, J. Lodewyck, O Lopez, and P.-E. Pottie. A clock network for geodesy and fundamental science. Nature Communications, 7:12443, 8 2016.

- [102] Jrme Lodewyck, Sawomir Bilicki, Eva Bookjans, Jean-Luc Robyr, Chunyan Shi, Grgoire Vallet, Rodolphe Le Targat, Daniele Nicolodi, Yann Le Coq, Jocelyne Guéna, Michel Abgrall, Peter Rosenbusch, and Sbastien Bize. Optical to microwave clock frequency ratios with a nearly continuous strontium optical lattice clock. Metrologia, 53(4):1123–1130, 8 2016.
- [103] E. Y. Loh, J. E. Gubernatis, R. T. Scalettar, S. R. White, D. J. Scalapino, and R. L. Sugar. Sign problem in the numerical simulation of many-electron systems. Physical Review B, 41(13):9301–9307, 5 1990.
- [104] M. Lohse, C. Schweizer, O. Zilberberg, M. Aidelsburger, and I. Bloch. A Thouless quantum pump with ultracold bosonic atoms in an optical superlattice. Nature Physics, 12(4):350–354, 12 2015.
- [105] Andrew D. Ludlow, Martin M. Boyd, Jun Ye, E. Peik, and P.O. Schmidt. Optical atomic clocks. Reviews of Modern Physics, 87(2):637–701, 6 2015.
- [106] M. Mancini, G. Pagano, G. Cappellini, L. Livi, M. Rider, J. Catani, C. Sias, P. Zoller, M. Inguscio, M. Dalmonte, and L. Fallani. Observation of chiral edge states with neutral fermions in synthetic Hall ribbons. Science, 349(6255), 2015.
- [107] Markus Greiner. Ultracold quantum gases in three-dimensional optical lattice potentials. PhD thesis, Ludwig-Maximilians-Universität München, 2003.
- [108] David J.E. Marsh. Axion cosmology. Physics Reports, 643:1–79, 2016.
- [109] M. J. Martin, M. Bishof, M. D. Swallows, X. Zhang, C. Benko, J. Von-Stecher, A. V. Gorshkov, A. M. Rey, and J. Ye. A quantum many-body spin system in an optical lattice clock. Science, 341(6146):632–6, 2013.
- [110] Martin M. Boyd. High Precision Spectroscopy of Strontium in an Optical Lattice: Towards a New Standard for Frequency and Time. PhD thesis, 2007.
- [111] D. G. Matei, T. Legero, S. Häfner, C. Grebing, R. Weyrich, W. Zhang, L. Sonderhouse, J. M. Robinson, J. Ye, F. Riehle, and U. Sterr. 1.5 μm lasers with sub 10 mhz linewidth. 2 2017.
- [112] Matthew Swallows. A search for the permanent electric dipole moment of mercury-199. PhD thesis, University of Washington, 2007.
- [113] Thomas McGreevy. The Basis of Measurement: Volume 1 Historical Aspects. T Pitcon Publishing, Chippenham, 1995.
- [114] D. Meiser, Jun Ye, D. R. Carlson, and M. J. Holland. Prospects for a Millihertz-Linewidth Laser. Physical Review Letters, 102(16):163601, 4 2009.
- [115] Michael J. Martin. Quantum Metrology and Many-Body Physics: Pushing the Frontier of the Optical Lattice Clock. PhD thesis, University of Colorado, 2013.
- [116] R. A. Millikan. On the Elementary Electrical Charge and the Avogadro Constant. Physical Review, 2(2):109–143, 8 1913.
- [117] Ian D. Leroux Monika Schleier-Smith and Vladan Vuleti. Spin Squeezing on an Atomic Clock Transition. In M. Rozman R. Côté, P.L Gould and W.W. Smith, editors, Proceedings of the XXI. International Conference on Atomic Physics. World Scientific, 2009.

- [118] Steven A. Moses, Jacob P. Covey, Matthew T. Miecnikowski, Bo Yan, Bryce Gadway, Jun Ye, and Deborah S. Jin. Creation of a low-entropy quantum gas of polar molecules in an optical lattice. Science, 350(6261), 2015.
- [119] Takashi Mukaiyama and Masahito Ueda. Universal Thermodynamics of a Unitary Fermi Gas. pages 361–377. Springer Berlin Heidelberg, 2013.
- [120] N. G. Basov and A. M. Prokhorov. Possible methods of obtaining active molecules for a molecular oscillator. Sov. Phys. JETP, 1:184–185, 1955.
- [121] T. L. Nicholson, S. L. Campbell, R. B. Hutson, G. E. Marti, B. J. Bloom, R. L. McNally, W. Zhang, M. D. Barrett, M. S. Safronova, G. F. Strouse, W. L. Tew, and J. Ye. Systematic evaluation of an atomic clock at 2×10^{-18} total uncertainty. Nature communications, 6:6896, 2015.
- [122] T. L. Nicholson, M. J. Martin, J. R. Williams, B. J. Bloom, M. Bishof, M. D. Swallows, S. L. Campbell, and J. Ye. Comparison of two independent sr optical clocks with 10^{-17} stability at 103s. Physical Review Letters, 109(23), 2012.
- [123] Matthew A. Norcia and James K. Thompson. Cold-Strontium Laser in the Superradiant Crossover Regime. Physical Review X, 6(1):011025, 3 2016.
- [124] Matthew A. Norcia, Matthew N. Winchester, Julia R. K. Cline, and James K. Thompson. Superradiance on the millihertz linewidth strontium clock transition. Science Advances, 2(10), 2016.
- [125] Laurin Ostermann, Helmut Ritsch, and Claudiu Genes. Protected State Enhanced Quantum Metrology with Interacting Two-Level Ensembles. Physical Review Letters, 111(12):123601, 9 2013.
- [126] R. D. Peccei and Helen R. Quinn. CP Conservation in the Presence of Pseudoparticles. Physical Review Letters, 38(25):1440–1443, 6 1977.
- [127] S. G. Porsev, Andrew D. Ludlow, Martin M. Boyd, and Jun Ye. Determination of Sr properties for a high-accuracy optical clock. Physical Review A, 78(3):032508, 9 2008.
- [128] T. J. Quinn. The new SI based on fundamental constants. Philosophical Transactions of the Royal Society A: Mathematical, Physical and Engineering Sciences, 369(1953):3905–3906, 10 2011.
- [129] R. Oerter. The Theory of Almost Everything: The Standard Model, the Unsung Triumph of Modern Physics. Penguin Group, 2006.
- [130] I Rabi, J. Zacharias, S. Millman, and P. Kusch. A New Method of Measuring Nuclear magnetic Moment. Physical Review, 53:318, 1938.
- [131] Norman F. Ramsey. A Molecular Beam Resonance Method with Separated Oscillating Fields. Physical Review, 78(6):695–699, 6 1950.
- [132] Mohit Randeria and Edward Taylor. Crossover from Bardeen-Cooper-Schrieffer to Bose-Einstein Condensation and the Unitary Fermi Gas. Annual Review of Condensed Matter Physics, 5(1):209–232, 3 2014.

- [133] Robert B. Laughlin. A Different Universe: Reinventing Physics from the Bottom Down. Basic Books, New York, 2006.
- [134] T. Rom, Th. Best, D. van Oosten, U. Schneider, S. Fölling, B. Paredes, and I. Bloch. Free fermion antibunching in a degenerate atomic Fermi gas released from an optical lattice. Nature, 444(7120):733–736, 12 2006.
- [135] T. Rosenband, D. B. Hume, P. O. Schmidt, C. W. Chou, A. Brusch, L. Lorini, W. H. Oskay, R. E. Drullinger, T. M. Fortier, J. E. Stalnaker, S. A. Diddams, W. C. Swann, N. R. Newbury, W. M. Itano, D. J. Wineland, and J. C. Bergquist. Frequency ratio of Al⁺ and Hg⁺ single-ion optical clocks; metrology at the 17th decimal place. Science, 319(5871):1808–12, 3 2008.
- [136] R. M. Sandner, M. Müller, A. J. Daley, and P. Zoller. Spatial Pauli blocking of spontaneous emission in optical lattices. Physical Review A, 84(4):043825, 10 2011.
- [137] T. A. Savard, K. M. OHara, and J. E. Thomas. Laser-noise-induced heating in far-off resonance optical traps. Physical Review A, 56(2):R1095–R1098, 8 1997.
- [138] F. Scazza, C. Hofrichter, M. Höfer, P. C. De Groot, I. Bloch, and S. Fölling. Observation of two-orbital spin-exchange interactions with ultracold SU(N)-symmetric fermions. Nature Physics, 10(10):779–784, 2014.
- [139] P. Schauß, J. Zeiher, T. Fukuhara, S. Hild, M. Cheneau, T. Macrì, T. Pohl, I. Bloch, and C. Gross. Crystallization in Ising quantum magnets. Science, 347(6229), 2015.
- [140] M. Schioppo, R. C. Brown, W. F. McGrew, N. Hinkley, R. J. Fasano, K. Beloy, T. H. Yoon, G. Milani, D. Nicolodi, J. A. Sherman, N. B. Phillips, C. W. Oates, and A. D. Ludlow. Ultrastable optical clock with two cold-atom ensembles. Nature Photonics, 11(1):48–52, 11 2016.
- [141] S. Schlamminger, K.-Y. Choi, T. A. Wagner, J. H. Gundlach, and E. G. Adelberger. Test of the Equivalence Principle Using a Rotating Torsion Balance. Physical Review Letters, 100(4):041101, 1 2008.
- [142] U. Schneider, L. Hackermüller, S. Will, Th. Best, I. Bloch, T. A. Costi, R. W. Helmes, D. Rasch, and A. Rosch. Metallic and Insulating Phases of Repulsively Interacting Fermions in a 3D Optical Lattice. Science, 322(5907), 2008.
- [143] National Academy of Sciences. Biographical Memoirs. National Academies Press, Washington, D.C., 11 2009.
- [144] C. Shi, J.-L. Robyr, U. Eismann, M. Zawada, L. Lorini, R. Le Targat, and J. Lodewyck. Polarizabilities of the ⁸⁷Sr clock transition. Physical Review A, 92(1):012516, 7 2015.
- [145] Silke Ospelkaus-Schwarzer. Quantum Degenerate Fermi-Bose Mixtures of ⁴⁰K and ⁸⁷Rb in 3D Optical Lattices. PhD thesis, Universität Hamburg, 2006.
- [146] Sir Isaac Newton. Opticks. CreateSpace Independent Publishing Platform, 1704.
- [147] Britney Spears. Britney Spears’ Guide to Semiconductor Physics - Lasers and Optoelectronics.

- [148] Y. V. Stadnik and V. V. Flambaum. Enhanced effects of variation of the fundamental constants in laser interferometers and application to dark-matter detection. Physical Review A, 93(6):063630, 6 2016.
- [149] Simon Stellmer, Rudolf Grimm, and Florian Schreck. Production of quantum-degenerate strontium gases. Physical Review A - Atomic, Molecular, and Optical Physics, 87(1), 2013.
- [150] Steven Chu. The Manipulation of Neutral Particles. In Nobel Lectures, Physics 1996-2000,. World Scientific Publishing Co., Singapore, 2002.
- [151] B. K. Stuhl, H.-I. Lu, L. M. Ayccock, D. Genkina, and I. B. Spielman. Visualizing edge states with an atomic Bose gas in the quantum Hall regime. Science, 349(6255), 2015.
- [152] Matthew D. Swallows, Michael Bishof, Yige Lin, Sebastian Blatt, Michael J. Martin, Ana Maria Rey, and Jun Ye. Suppression of Collisional Shifts in a Strongly Interacting Lattice Clock. Science, 331(6020), 2011.
- [153] Masao Takamoto, Feng-Lei Hong, Ryoichi Higashi, and Hidetoshi Katori. An optical lattice clock. Nature, 435(7040):321–324, 5 2005.
- [154] Masao Takamoto, Tetsushi Takano, and Hidetoshi Katori. Frequency comparison of optical lattice clocks beyond the Dick limit. Nature Photonics, 5(5):288–292, 5 2011.
- [155] Storm Thorgerson and George Hardie. Dark side of the moon album cover, https://upload.wikimedia.org/wikipedia/en/3/3b/dark_side_of_the_moon.png.
- [156] S. Trotzky, P. Cheinet, S. Fölling, M. Feld, U. Schnorrberger, A. M. Rey, A. Polkovnikov, E. A. Demler, M. D. Lukin, and I. Bloch. Time-Resolved Observation and Control of Superexchange Interactions with Ultracold Atoms in Optical Lattices. Science, 319(5861), 2008.
- [157] Ichiro Ushijima, Masao Takamoto, Manoj Das, Takuya Ohkubo, and Hidetoshi Katori. Cryogenic optical lattice clocks. Nature Photonics, 9:1–5, 2015.
- [158] Ken Van Tilburg, Nathan Leefer, Lykourgos Bougas, and Dmitry Budker. Search for Ultralight Scalar Dark Matter with Atomic Spectroscopy. Physical Review Letters, 115(1):011802, 6 2015.
- [159] ed. Vincent, Nicholas. Magna Carta. 1215.
- [160] P. G. Westergaard, J. Lodewyck, L. Lorini, A. Lecallier, E. A. Burt, M. Zawada, J. Millo, and P. Lemonde. Lattice-induced frequency shifts in sr optical lattice clocks at the 10^{-17} level. Physical Review Letters, 106(21), 2011.
- [161] William D. Phillips. Laser Cooling and Trapping of Neutral Atoms. In Nobel Lectures, Physics 1996-2000. World Scientific Publishing Co., Singapore, 2002.
- [162] James G. Williams, Slava G. Turyshev, and Dale H. Boggs. Progress in Lunar Laser Ranging Tests of Relativistic Gravity. Physical Review Letters, 93(26):261101, 12 2004.
- [163] James G Williams, Slava G Turyshev, and Dale H Boggs. Lunar laser ranging tests of the equivalence principle. Classical and Quantum Gravity, 29(18):184004, 9 2012.

- [164] David J. Wineland. Nobel Lecture: Superposition, entanglement, and raising Schrödinger's cat. Reviews of Modern Physics, 85(3):1103–1114, 7 2013.
- [165] R Wynands and S Weyers. Atomic fountain clocks. Metrologia, 42(3):S64–S79, 6 2005.
- [166] Xinye Xu, Thomas H. Loftus, John L. Hall, Alan Gallagher, and Jun Ye. Cooling and trapping of atomic strontium. Journal of the Optical Society of America B, 20(5):968, 5 2003.
- [167] Bo Yan, Steven A. Moses, Bryce Gadway, Jacob P. Covey, Kaden R. A. Hazzard, Ana Maria Rey, Deborah S. Jin, and Jun Ye. Observation of dipolar spin-exchange interactions with lattice-confined polar molecules. Nature, 501(7468):521–525, 9 2013.
- [168] Jun Ye, H. J. Kimble, and Hidetoshi Katori. Quantum State Engineering and Precision Metrology Using State-Insensitive Light Traps. Science, 320(5884), 2008.
- [169] M. H. You, J. R. Lewenstein, M. R. Cooper, C. E. Wieman, and E. A. Cornell. Quantum field theory of atoms interacting with photons. II. Scattering of short laser pulses from trapped bosonic atoms. Physical Review A, 51(6):4712–4727, 6 1995.
- [170] J. Zhang, P. W. Hess, A. Kyprianidis, P. Becker, A. Lee, J. Smith, G. Pagano, I.-D. Potirniche, A. C. Potter, A. Vishwanath, N. Y. Yao, and C. Monroe. Observation of a discrete time crystal. Nature, 543(7644):217–220, 3 2017.
- [171] X. Zhang, M. Bishof, S. L. Bromley, C. V. Kraus, M. S. Safronova, P. Zoller, Ana Maria Rey, and Jun Ye. Spectroscopic observation of $SU(N)$ -symmetric interactions in Sr orbital magnetism. Science, 1467(m):1–11, 2014.
- [172] Erez Zohar, J. Ignacio Cirac, and Benni Reznik. Quantum simulations of gauge theories with ultracold atoms: Local gauge invariance from angular-momentum conservation. Physical Review A, 88(2):023617, 8 2013.
- [173] Wojciech H. Zurek, Uwe Dorner, and Peter Zoller. Dynamics of a Quantum Phase Transition. Physical Review Letters, 95(10):105701, 9 2005.

Appendix A

Anti-reflection coating fused silica viewports: A cautionary tale

Here we highlight some things that can go wrong when you have a company that is accustomed to coating 7056 glass viewports try and coat your fancy fused-silica viewports. Fused silica viewports have a maximum bakeout temperature of 200°C , a maximum thermal gradient of $25^{\circ}\text{C}/\text{minute}^1$, and the glass-to-metal seal is done via solder. Compare this to 7056 glass viewports (common in many other AMO labs), which have a 400°C maximum bakeout temperature, a maximum thermal gradient of $10^{\circ}\text{C}/\text{minute}^1$, with a glass-to-metal seal comprised of a “matched expansion seal.” The 7056 glass is more brittle and sensitive to thermal fluctuations, and so the glass-to-metal seal is made from the iron-nickel-cobalt alloy Kovar which has low thermal expansion similar to the glass. In contrast, fused silica is more resistant to thermal shock and are brazed directly into the Conflat flange using PbAg solder or similar. However, with this improved resistance to thermal shock comes more compilability, and the bending of the glass as it is rapidly heated (perhaps at different rate than the metal flange if the coating company is not careful) can place too much mechanical strain on the coating itself, causing it to fracture or peel off as the viewport bends during the coating process as shown in A.2. One of our coatings even arrived intact, but, as shown in Figure A.3, one side peeled off after the slightest disturbance of a careful methanol rinse. (In case the reader is wondering: Delamination occurred as soon as we poured the methanol on the viewport. It did not happen because we thermally-shocked the viewport by via evaporative cooling from aggressively blasting it with gas to dry it.) This possibly can also affect the thickness of the thin film layers,

¹ Though, according to Kurt J. Lesker: “Opinions vary about maximum heating rate, but there is no penalty for being cautious and using the lowest quoted heating rate of $\approx 2^{\circ}\text{C}/\text{minute}$.”

which can then cause the final coating to miss the target wavelength as shown in Figure A.1.

We recently learned of yet another AR coating failure mode from another group who used one of the same companies that we did.² The company did not mask the knife edge of the viewports. It is my understanding that this is typically not an issue (our knife edges were coated as well, as I believe is common), but for some reason their coating was permeable, so they saw leaks on the RGA at the $\geq 1 \times 10^{-9}$ Torr level. They were able to fix some of the windows by attaching and reattaching them so that the copper gaskets would cause the coating to be somewhat scraped off, and scrubbing the knife edge with acetone and then methanol in between. They were not confident about the larger viewports, however. In any case, if for some strange reason the AR coating is permeable (I wonder if it was somehow defective in a new strange way), it is crucial to have the company mask the knife edge. They subsequently had success with viewports from MPF. We also think that the company FiveNine Optics sounds also promising (as REO always did a fantastic job with AR coating viewport).

In conclusion, we recommend that other groups wishing to coat fused silica viewports make sure that their company understands the difference between the glass-to-metal seals for fused silica and 7056 glass, and has had specific experience with successfully coating *fused silica* viewports. If their coating is not UHV-compatible, they need to mask the knife edge as well. Additionally, we advise checking that the company does *ion* beam sputtering, which is more robust than electron beam sputtering.

² Thank you to Paul Lauria of the Barreiro lab at UCSD for providing this information so that we may inform the community ASAP and prevent future headaches such as those that have occurred both of our labs.

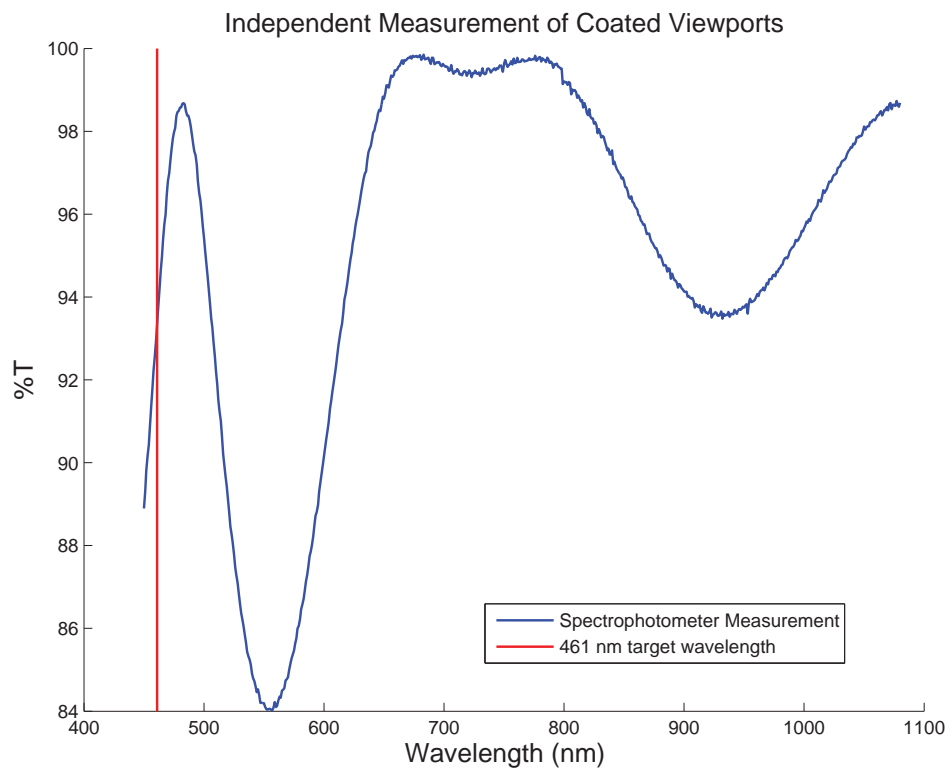


Figure A.1: Spectrophotometer measurement illustrating the decline of American manufacturing. APC/Blue Ridge Optics completely missed the 461 nm target wavelength.

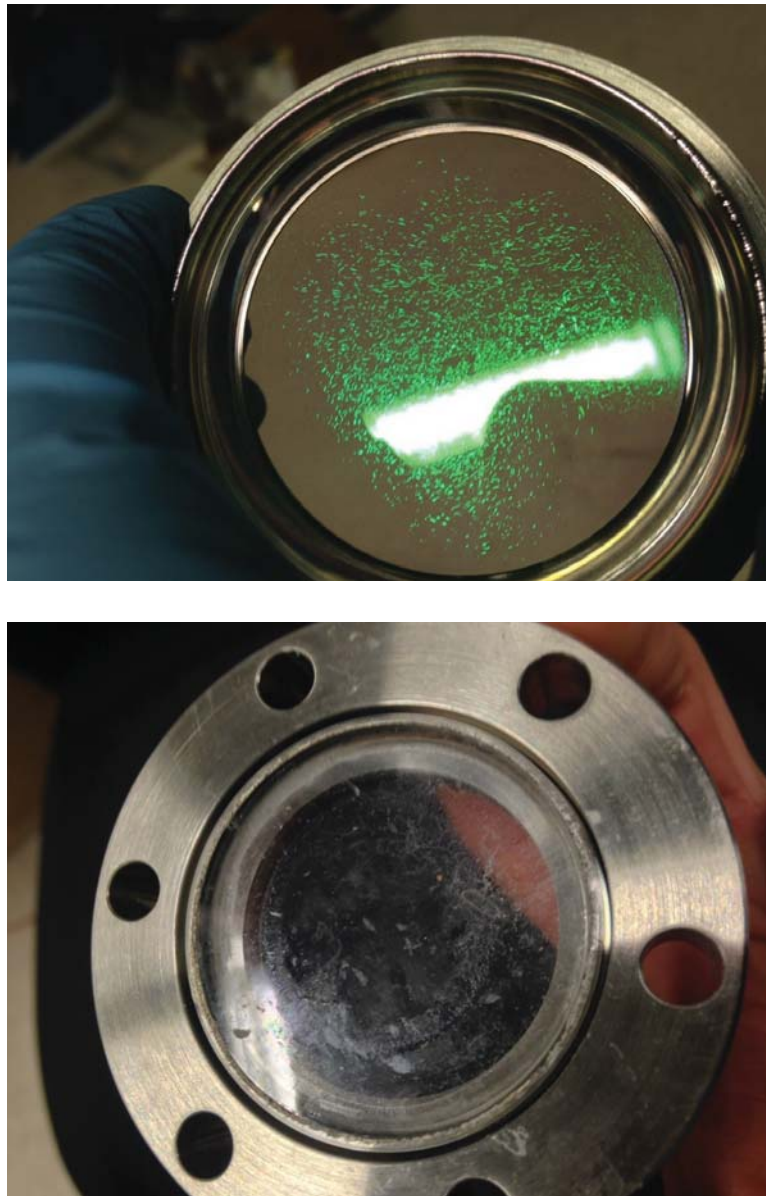


Figure A.2: Top: Shattered AR coating on the bucket window sub-assembly due to mechanical stress caused by improper temperature control during the sputtering process. Bottom: Viewport after Blue Ridge Optics etched away the faulty AR coating. We agreed that they would do one test viewport and let us know how it goes. Instead, they damaged \$10,000 of equipment, leaving deep scratches and pockmarks on every viewport that we shipped back to them. Surprisingly, they were willing to just ship everything back to us and pretend that there was no problem. One of the conclusions of this thesis is that one should never, ever have their coatings done by American Photonics or Blue Ridge Optics.

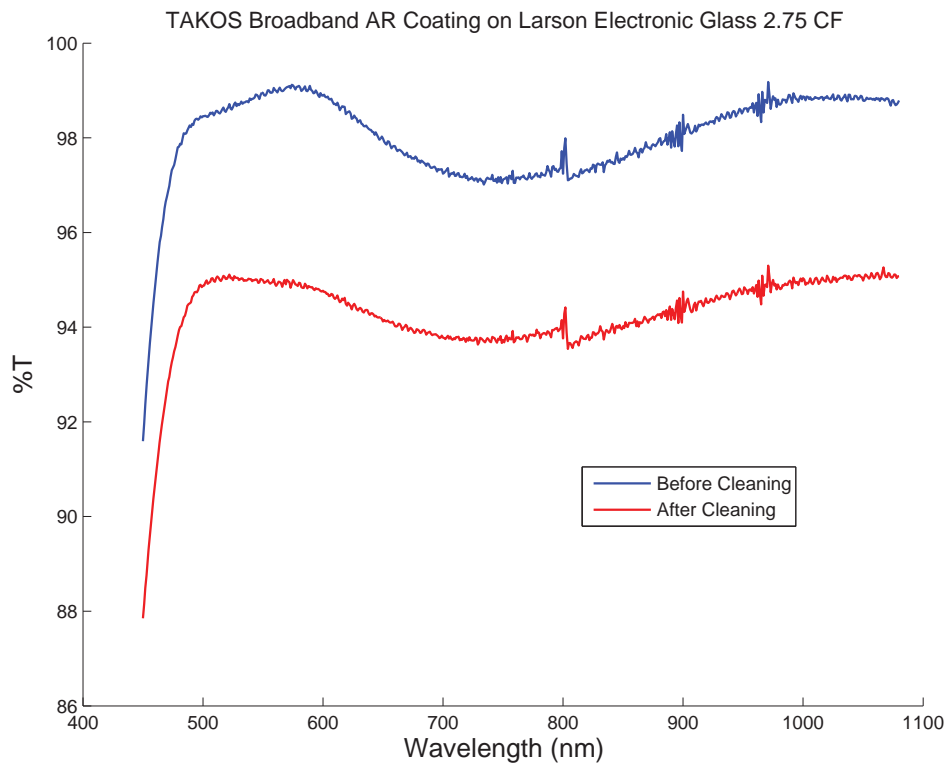


Figure A.3: A reminder that one should remind companies to use special care to temperature-control fused silica viewports during coating. Spectrophotometer measurements before and after one side of the viewport AR coating from TAKOS delaminated. Another set of viewports made with 7056 glass for the Thompson group in the same coating run had no problems.